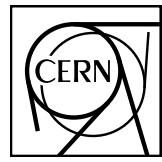


EUROPEAN ORGANIZATION FOR NUCLEAR RESEARCH



June 10, 2017

D-hadron correlations in p-Pb collisions at $\sqrt{s_{NN}} = 5.02 \text{ TeV}$

F. Colamaria, S. Kumar, M. Mazzilli

Abstract

In this note, we present the analysis of azimuthal correlations of D mesons and primary charged particles performed in the ALICE central barrel in p-Pb collisions at $\sqrt{s_{NN}} = 5.02 \text{ TeV}$, from 2016 data taking, in an extended p_T range and with additional observables with respect to p-Pb 2013 data analysis. After a description of the analysis strategy, corrections and systematic uncertainties, the results obtained for prompt D^0 , D^{*+} and D^+ mesons in different ranges of transverse momentum of the D meson and of the associated particles are presented and compared to Monte Carlo models and, for the common p_T ranges and observables, to 2013 p-Pb analysis.

1 **Contents**

2	1	Introduction and Motivation	3
3	2	Data/Monte Carlo samples and event selection	4
4	3	Analysis strategy	7
5	3.1	Mass plots and cut optimization	10
6	3.2	Code used for the analysis	14
7	3.3	Further details on corrections	14
8	3.3.1	Event Mixing	14
9	3.3.2	Tracking and D-meson trigger efficiency	18
10	3.3.3	Correction for bias on B to D decay topologies	22
11	3.3.4	Secondary track contamination	27
12	3.3.5	Beauty feed-down	31
13	4	Systematic uncertainties on $\Delta\phi$ correlation distributions	35
14	4.1	Uncertainty on S and B extraction	35
15	4.2	Uncertainty on background correlation shape	35
16	4.3	Uncertainty on D-meson cut stability	39
17	4.4	Uncertainty on tracking efficiency evaluation	39
18	4.5	Uncertainty on secondary particle contamination	43
19	4.6	Uncertainty on feed-down subtraction	44
20	4.7	Uncertainty on correction for the bias on B to D decay topologies	48
21	4.8	Summary table	49
22	5	Results	50
23	5.1	Comparing the three D meson correlation distributions	50
24	5.2	Average of D^0 , D^+ and D^{*+} results	63
25	5.3	Fit observable p_T trends and uncertainties	66
26	5.3.1	Results for near-side yield and width, away-side yield and width, and baseline .	67
27	5.4	Comparison of 2016 p-Pb and 2013 p-Pb results	83
28	5.5	Comparison of 2016 p-Pb and 2010 pp results	83
29	5.6	Comparison of 2016 p-Pb and model expectations	83
30	5.7	Planned results for SQM approvals	83

³¹	6	Bibliography	94
---------------	----------	---------------------	-----------

32 **1 Introduction and Motivation**

33 The study of the azimuthal correlations of heavy-flavour particles and charged particles at the LHC
 34 energies provides a way to characterize charm production and fragmentation processes in pp collisions
 35 as well as a way to probe our understanding of QCD in the perturbative regime, accessible in a large
 36 kinematic range given the large mass of heavy quarks. Flavour conservation in QCD implies that charm
 37 quarks are always produced as pairs of quarks and anti-quarks. The azimuthal correlations obtained
 38 using a meson carrying a heavy quark as trigger particle with the other charged particles in the same
 39 event give the possibility to study the underlying charm production mechanism in detail. In particular,
 40 prompt charm quark-antiquark pair production is back to back in azimuth at first order in leading-order
 41 perturbative-QCD (pQCD). Heavy quarks produced from the splitting of a massless gluon can be rather
 42 collimated and may generate sprays of hadrons at small $\Delta\phi$. Finally, for hard-scattering topologies
 43 classified as “flavour-excitation”, a charm quark undergoes a hard interaction from an initial splitting
 44 ($g \rightarrow c\bar{c}$), leading to a big separation in rapidity of the hadrons originating from the antiquark (quark)
 45 with respect to the trigger D meson and contribute to a rather flat term to the $\Delta\phi$ -correlation distribution.

46 Heavy-flavour correlation studies in more complex collision systems, like Pb-Pb, play a crucial role in
 47 studying the modification of the fragmentation of charmed jets due to in-medium (or cold nuclear matter,
 48 in case of p-Pb collisions) effects, in a similar way as it was done for di-hadron correlation studies in
 49 heavy-ion collisions (see for example). Furthermore, the recent observation of long range correlations in
 50 p-Pb for light flavour hadrons and for heavy-flavour decay electrons points to possible collective effects
 51 or effects originating from gluon saturation in the initial state. More information could be extracted by
 52 the eventual observation of the same effect with D mesons.

53

54 In the following, we describe the analysis strategy for the p-Pb 2016 data sample in all its steps, and we
 55 describe the list of corrections and the estimation of the systematic uncertainties we performed. We then
 56 present the results of $\Delta\phi$ correlations, and quantitative observable extracted to fits to those distributions,
 57 obtained for prompt D^0 , D^+ and D^{*+} in different ranges of transverse momentum for the D-meson
 58 (trigger particle) and the associated particles.

59 **2 Data/Monte Carlo samples and event selection**

60 The data samples used for the analyses were the FAST and CENT_woSDD samples from periods LHC16q
 61 and LHC16t (AOD samples). The reason for this choice is explained later on, in this section. It was ver-
 62 ified, by looking at D-meson and track η and φ distributions, and at the mixed-event correlation distri-
 63 butions for each subsamples, that no visible differences arose for the four periods, hence it was possible
 64 to perform the analysis directly on the merged samples without any bias.

65 The Monte Carlo productions adopted for this study were:

- 66 1. LHC17d2a_fast_new, a HIJING production with enrichment, for each event, of c or b quarks and
 67 their decay chains, performed by PYTHIA6 with Perugia2011 tune, and with forced hadronic
 68 decays of the charmed hadrons. This production was used for D-meson efficiency evaluation,
 69 purity estimation and Monte Carlo closure test.
- 70 2. LHC17f2b_cent_woSDD and LHC17f2b_fast, minimum-bias samples produced with DPMJET
 71 generator, used for the evaluation of the tracking efficiencies.

72 Table 1 shows the list of runs used for the analysis, for each of the data taking periods, and of the Monte
 73 Carlo productions used to evaluate the corrections:

74 The trigger mask request for the event selection is kINT7. Only events with a reconstructed primary
 75 vertex within 10 cm from the centre of the detector along the beam line are considered for both pp
 76 and p-Pb collisions. This choice maximises the detector coverage of the selected events, considering
 77 the longitudinal size of the interaction region, and the detector pseudorapidity acceptances. For p-Pb
 78 collisions, the center-of-mass reference frame of the nucleon-nucleon collision is shifted in rapidity by
 79 $y_{NN} = 0.465$ in the proton direction with respect to the laboratory frame, due to the different per-nucleon
 80 energies of the proton and the lead beams. Beam-gas events are removed by offline selections based
 81 on the timing information provided by the V0 and the Zero Degree Calorimeters, and the correlation
 82 between the number of hits and track segments in the SPD detector. This is automatically performed in
 83 the Physic Selection, a positive outcome of which is required during our event selection. The minimum-
 84 bias trigger efficiency is 100% for events with D mesons with $p_T > 1$ GeV/c. For the analyzed data
 85 samples, the probability of pile-up from collisions in the same bunch crossing is below 2% per triggered
 86 event (in most of the runs, well below 1%). Events in which more than one primary interaction vertex
 87 is reconstructed with the SPD detector (with minimum of 5 contributors, and a z distance greater than
 88 0.8 cm) are rejected, which effectively removes the impact of in-bunch pile-up events on the analysis.
 89 Out-of-bunch tracks are effectively rejected by the request of at least one point in the SPD, which has
 90 a very limited time acquisition window (300 ns). Indeed, though the default associated track selection
 91 requires a minimum of 2 points in the ITS, as it will be shown later on full compatibility of the corrected
 92 results with 2 and 3 minimum ITS clusters is obtained. For FAST and CENT_woSDD samples, the latter
 93 case indirectly forces the presence of a point in the SPD.

94 Since data collected during p-Pb 2016 data taking are distinguished into two categories - one including
 95 SDD detector (CENT_wSDD sample) and a second one without the SDD in the reconstruction, or in the
 96 acquisition (CENT_woSDD and FAST samples, respectively), a study of performance of the D-hadron
 97 correlation analysis with respect to the data samples employed has been carried out for D^{*+} and D^+
 98 mesons (more sensitive to the presence of the SDD w.r.t. the D^0 , due to their reconstruction from three
 99 decay tracks).

100 For this reason, the D-hadron correlation distribution has been compared on LHC16q_pass1_CENT_wSDD
 101 and LHC16q_pass1_CENT_woSDD and the relative statistical uncertainty has been estimated in order to
 102 understand if it was better to perform the analysis separately on the two data sample, applying in this
 103 case different corrections, or not. In particular, it was crucial for the correlation analysis involving the

Type	Production	Run list	nEvents
Monte-Carlo	LHC17d2a_fast_new (c/b enriched), LHC17f2b_fast (MB), LHC17f2b_cent_woSDD (MB)	267166, 267165, 267164, 267163, 265525, 265521, 265501, 265500, 265499, 265435, 265427, 265426, 265425, 265424, 265422, 265421, 265420, 265419, 265388, 265387, 265385, 265384, 265383, 265381, 265378, 265377, 265344, 265343, 265342, 265339, 265338, 265336, 265335, 265334, 265332, 265309 = [36 runs]	50M
Data	LHC16q, pass1_CENT_woSDD	265525, 265521, 265501, 265500, 265499, 265435, 265427, 265426, 265425, 265424, 265422, 265421, 265420, 265419, 265388, 265387, 265385, 265384, 265383, 265381, 265378, 265377, 265344, 265343, 265342, 265339, 265338, 265336, 265335, 265334, 265332, 265309 = [32 runs]	261M total
	LHC16q, pass1_FAST	265525, 265521, 265501, 265500, 265499, 265435, 265427, 265426, 265425, 265424, 265422, 265421, 265420, 265419, 265388, 265387, 265385, 265384, 265383, 265381, 265378, 265377, 265344, 265343, 265342, 265339, 265338, 265336, 265335, 265334, 265332, 265309 = [32 runs]	260M
	LHC16t, pass1_CENT_woSDD	267166, 267165, 267164, 267163 = [4 runs]	40M
	LHC16t, pass1_FAST	267166, 267165, 267164, 267163 = [4 runs]	41M

Table 1: Data Set and Run list

¹⁰⁴ D^{*+} meson because the track reconstruction efficiency of the soft pion is $\approx 10\%$ higher employing also
¹⁰⁵ the SDD information. Figure 1 shows the normalized azimuthal correlation distribution for low, mid
¹⁰⁶ and high p_T for D^{*+} meson. Blue points are referred to the woSDD sample while red points represents
¹⁰⁷ wSDD data. Figure 2 shows the relative statistical uncertainty extracted from the azimuthal correlation
¹⁰⁸ distributions for the D^{*+} in different kinematic ranges.

¹⁰⁹ It can be observed that the data sample that includes the SDD information is characterized by $\approx 10 - 15\%$
¹¹⁰ more statistics in each p_T ranges analyzed. This difference is related to the larger efficiency in track
¹¹¹ reconstruction with the wSDD sample - a larger number of tracks survives to the selection request of 3
¹¹² points in the ITS, which is part of the selection requests applied on the previous D-h analysis.

¹¹³ As a result, the wSDD sample is also affected by a slightly lower relative statistical uncertainty (about
¹¹⁴ 12-15%) due to several reasons: the larger tracking efficiency, the major number of signal entries in the
¹¹⁵ invariant mass distributions and a slight increase of S/B, which reflects in a slight decrease of uncertainty
¹¹⁶ from the sideband subtraction. It has also to be considered that, on the full sample including also the
¹¹⁷ FAST cluster, the increase in performance would be further reduced. The overall statistical uncertainty
¹¹⁸ difference resulting from the comparison is not enough to justify the implementation of two different
¹¹⁹ analysis and two subsequent different corrections either for D^{*+} and D⁺.

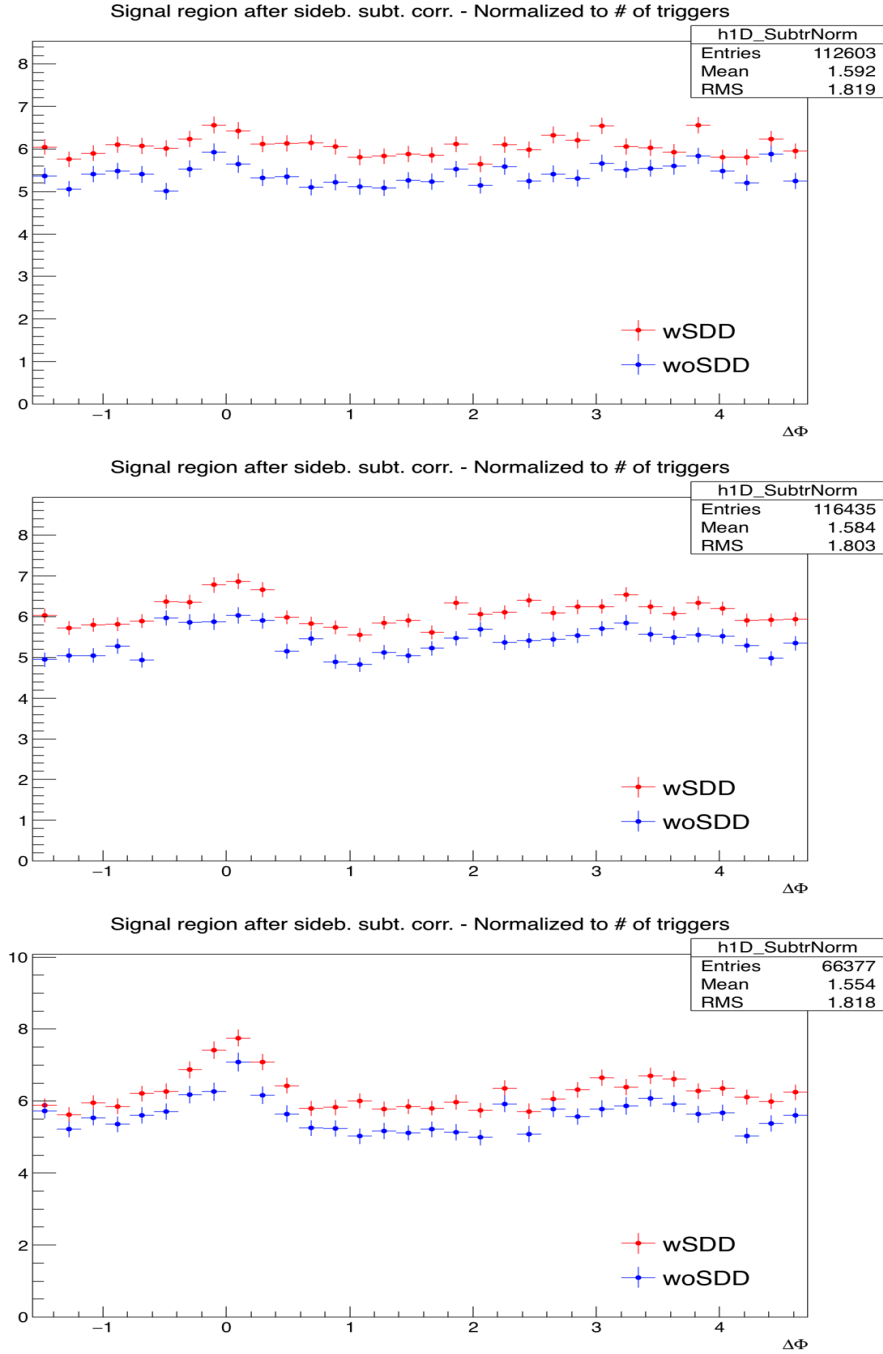


Figure 1: Normalized azimuthal correlation distribution of D^{*+} for low p_T ($3 < p_T(D^{*+}) < 5 \text{ GeV}/c$) on the top panel, mid p_T ($5 < p_T(D^{*+}) < 8 \text{ GeV}/c$) on the middle panel and high p_T ($8 < p_T(D^{*+}) < 16 \text{ GeV}/c$) on the bottom panel with a p_T threshold for associated tracks of $p_T(\text{assoc}) > 0.3 \text{ GeV}/c$. Blue points are referred to the woSDD sample while red points represent wSDD data.

120 Anyway, to cope with the lower tracking efficiency w.r.t. 2013 data sample, after this study it was decided
 121 to reduce the ITS request for the associated tracks from 3 (used on 2013 data) to 2 ITS clusters as default
 122 selection criterion.

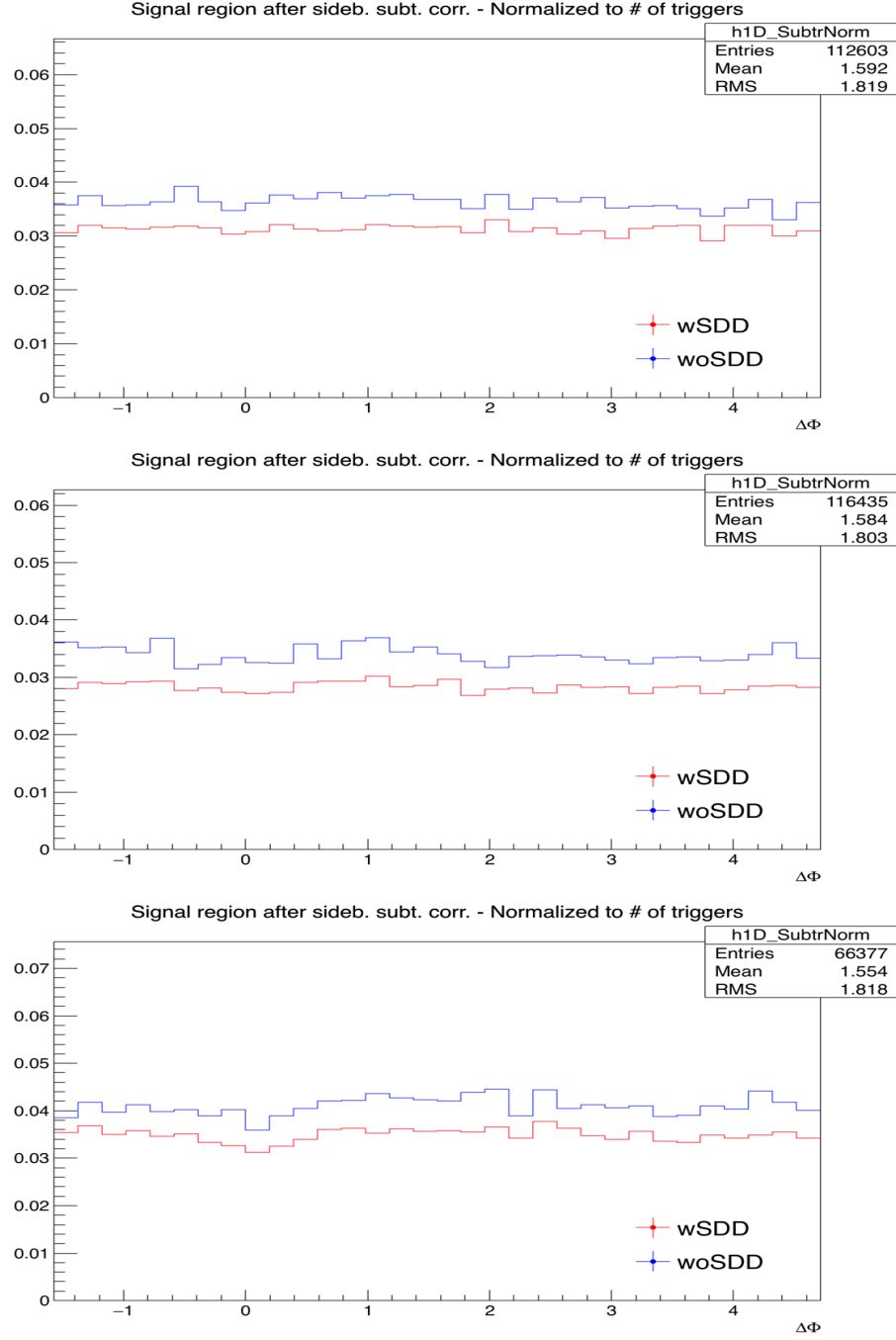


Figure 2: Statistical uncertainty extracted from the azimuthal correlation distribution of D^{*+} with associated charged particles. Top panel: $3 < p_T(D^{*+}) < 5 \text{ GeV}/c$. Mid panel: $5 < p_T(D^{*+}) < 8 \text{ GeV}/c$. Bottom panel: $8 < p_T(D^{*+}) < 16 \text{ GeV}/c$. Blue line is referred to the woSDD sample while the red line represents wSDD data.

123 3 Analysis strategy

124 The analysis strategy follows the one used from 2013 p-Pb data sample. Correlation pairs are formed by
 125 trigger particles (D mesons) reconstructed and selected in the following p_T^{trig} ranges: $3 < p_T^{\text{trig}} < 5 \text{ GeV}/c$,
 126 $5 < p_T^{\text{trig}} < 8 \text{ GeV}/c$, $8 < p_T^{\text{trig}} < 16 \text{ GeV}/c$, $16 < p_T^{\text{trig}} < 24 \text{ GeV}/c$, and associated particles (charged
 127 tracks) for the following p_T^{assoc} regions: $p_T^{\text{assoc}} > 0.3$, $0.3 < p_T^{\text{assoc}} < 1$, $1 < p_T^{\text{assoc}} < 2$, $2 < p_T^{\text{assoc}} < 3$,
 128 $p_T^{\text{assoc}} > 3 \text{ GeV}/c$ (with the addition of $p_T^{\text{assoc}} > 1 \text{ GeV}/c$ for comparison with p-Pb 2013 results). In
 129 D meson correlations, the particle identification defines the trigger particle rather than a momentum cut

and therefore the momentum range of the associated particles is not constrained by that of the trigger particle. Our definition of associated particle includes any charged particle coming from the primary vertex of interaction, including those coming from strong and electromagnetic decay of unstable particles, and particles deriving from the decay of hadrons with charm or beauty. We therefore include any charged particle except those coming from weak decays of strange particles and particles produced in the interaction with the detector material. This definition corresponds to that used in the method AliAODM-CParticle::IsPyphysicalPrimary(). All associated particles surviving the selection cuts and not matching the adopted criterion are considered as a contamination whose contribution has to be corrected for.

138

139 The analysis is performed through the following steps:

- 140 1. **D meson selection and signal extraction.** For each single event, “trigger” particles are defined
141 as the selected D meson candidates (D^0 , D^+ and D^{*+}) within a given p_T^{trig} range. The detection
142 strategy for D mesons at central rapidity is the same performed for the analyses of the D-meson
143 production at central rapidity [1], and also applied for the D-h analysis on 2010 pp and 2013 p-Pb
144 samples [2] and is based on the reconstruction of decay vertices displayed from the primary vertex
145 by a few hundred μm and on the identification of the decay-particle species. The identification of
146 the charged kaon and pion in the TPC and TOF detectors helps to further reduce the background at
147 low p_T . An invariant-mass analysis is then used to extract the raw signal yield, using the same fit
148 functions described in [2]. The D mesons are selected in the rapidity range varying from $|y| < 0.5$
149 at low p_T to $|y| < 0.8$ for $p_T > 5 \text{ GeV}/c$.
- 150 2. **Correlation of D candidates with associated tracks.** Particle pairs are formed by associating each
151 trigger particle with the charged primary particles passing the track selection (excluding those
152 coming from the decay of the D-meson candidate) in a specified p_T^{assoc} interval (which can overlap
153 with the p_T^{trig} range) and in the pseudo-rapidity range $|\eta| < 0.8$. For the D^0 meson, also the low-
154 momentum pion tracks from feed-down of D^{*+} mesons are removed via 3σ invariant mass cut on
155 the $M(K\pi\pi) - M(K\pi)$ difference. This because these soft pion are not related to the charm quark
156 fragmentation chain. For D meson candidates in the invariant mass signal region, defined by a \pm
157 2σ interval around the D meson mass, the azimuthal angle difference $\varphi^{\text{assoc}} - \varphi^{\text{trigg}} \equiv \Delta\varphi$ and the
158 pseudorapidity difference $\eta^{\text{assoc}} - \eta^{\text{trig}} \equiv \Delta\eta$ are evaluated and stored to build two-dimensional
159 correlation distribution.
- 160 3. **Correction for limited acceptance and detector inhomogeneities with Event Mixing** The angular
161 correlation distribution may be affected, even for uncorrelated pair of particles, by structures
162 not due to physical effects, but originating from the limited detector acceptance, as well as from
163 angular inhomogeneities in the trigger and track reconstruction efficiencies as a function of $\Delta\varphi$
164 and $\Delta\eta$. Effects of this kind are removed using the Event Mixing technique. In this technique, the
165 analysis is executed on the same data sample of the standard one (called “same event” analysis,
166 SE), but the trigger particles found in each event are correlated to charged particles reconstructed
167 in different events (“Mixed Events” analysis, ME) with similar characteristic, in particular con-
168 cerning the event multiplicity and z position of the primary vertex (see Section 3.3.1).

169

170 The differential yield of associated particles per trigger particle is obtained by

$$\frac{1}{N_{\text{trig}}} \frac{d^2N^{\text{pair}}}{d\Delta\eta d\Delta\varphi} = B_{\text{ME}}(0, 0) \times \frac{S(\Delta\eta, \Delta\varphi)}{B_{\text{ME}}(\Delta\eta, \Delta\varphi)}, \quad (1)$$

171 where N^{pair} is the total number of correlated D-hadron pairs. The functions $S(\Delta\eta, \Delta\varphi)$ and $B_{\text{ME}}(\Delta\eta, \Delta\varphi)$
172 are the signal and the mixed event background distributions, respectively. The latter is normalized

173 to its value in $(\Delta\eta, \Delta\phi) = (0, 0)$, i.e. $(B(0, 0))$. Further details on the mixed-event correction are
174 provided further on.

175 **4. Subtraction of background correlation from signal distribution.** The invariant mass signal re-
176 gion includes also background D-meson candidates. Their contribution to the raw correlation
177 distribution is subtracted as follows. For each p_T bin, the mean and the sigma of the invariant mass
178 spectrum are extracted. For D^0 and D^+ , a “background” region is defined in the sidebands of the
179 mass distribution as the interval $4\text{GeV}/c^2 < |m - m^{\text{pdg}}| < 8\text{GeV}/c^2$ (for the D^{*+} meson, only the
180 right sideband is used). The angular correlation distribution for background candidates in this re-
181 gion is extracted and normalized with respect to the background in the signal region estimated from
182 the mass fit. This normalized background correlation distribution is then subtracted from the raw
183 signal one to obtain the signal correlation distribution. The normalization factor is the ratio of the
184 number of background candidates under the signal peak (obtained by integrating the background
185 of the fit function within the signal region) over the number of background candidates in the side-
186 bands (obtained via bin-counting in the sideband region). This normalized background correlation
187 distribution is then subtracted from the raw signal one to obtain the signal correlation distribution.
188 An example of the signal region, sideband and sideband-subtracted 1D correlation distributions
189 (along $\Delta\phi$) is shown in figure 3, together with the comparison of the three distributions after the
190 normalization to the number of triggers.

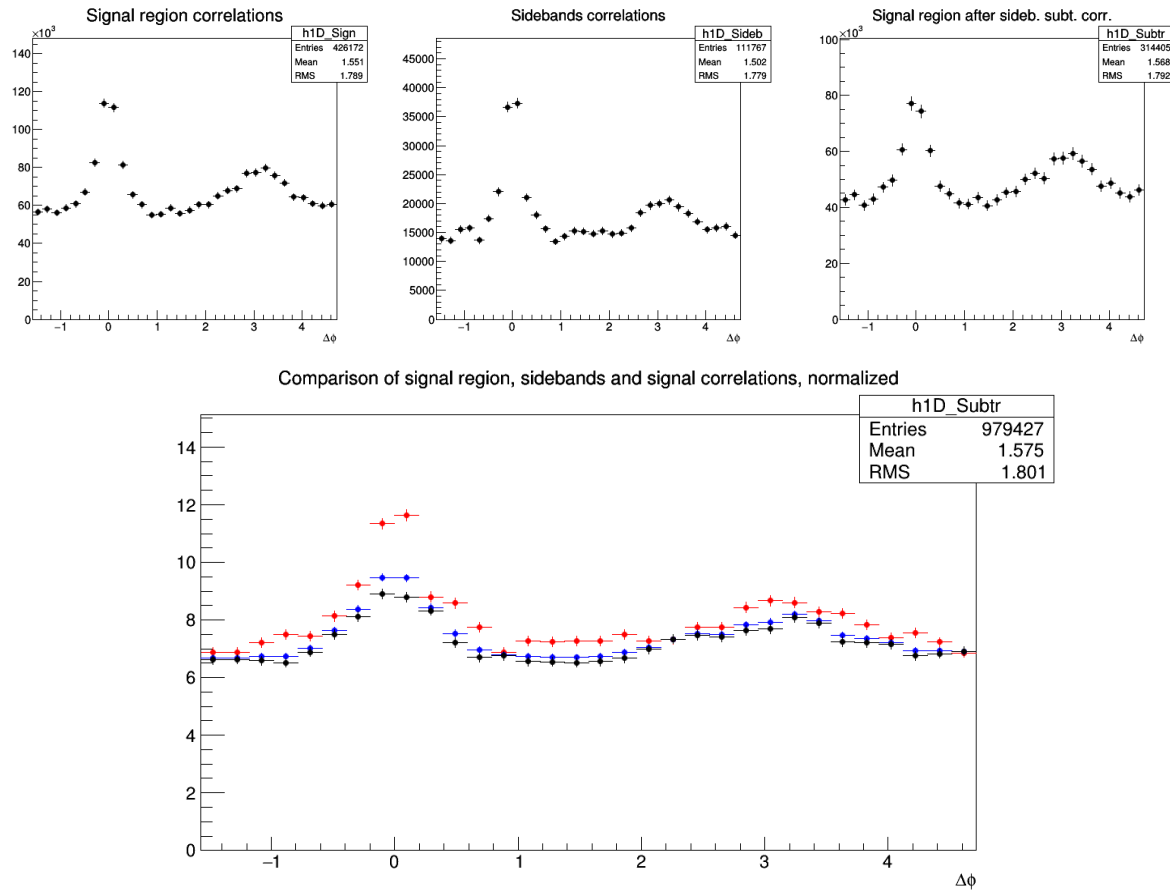


Figure 3: Top: Example of D^0 - h signal region (left), sideband (middle), and signal minus sideband (right) correlation distributions. Bottom: signal region per-trigger normalized correlation distribution (blue), sideband region per-trigger normalized correlation distribution (red), background-subtracted per-trigger normalized correlation distribution (black).

191 **5. Correction for D meson efficiency and associated track efficiency.** After filling the signal and

background correlation distributions, it is necessary to take into account also for the correlations with tracks not reconstructed, or not passing the quality selection due to poor reconstruction. In the same way, the loss of D-mesons which are not reconstructed, or do not pass the selection, impacts the correlation distribution shape. Hence, each pair is weighted by the inverse of the product of the associated track and D meson reconstruction efficiency, ε_{trk} and ε_{trig} . Further details are provided later on in this section.

6. **Projection in $\Delta\varphi$.** The limited statistics available does not allow to study the two dimensional $(\Delta\eta, \Delta\varphi)$ distribution, which is therefore projected to the $\Delta\varphi$ axis by integrating on $|\Delta\eta| < 1$. Despite, in principle, our maximum $\Delta\eta$ acceptance is of $|\Delta\eta| < 1.6$, removing the large $|\Delta\eta|$ regions allow us to reject angular regions with very low statistics, where fluctuations would be amplified by a large mixed-event correction, and avoid the so-called wings effect.

As the difference in the azimuthal angle is periodic ($\Delta\varphi = 0 = 2\pi$), the $\Delta\varphi$ -range is limited to the essential range of 2π . The $\Delta\varphi$ -limits are chosen to be $[-\pi/2, 3\pi/2]$ in order to provide a good visibility of the correlation pattern, which peaks around 0 and π .

7. **Correction for the contamination of secondary particles** The DCA to primary vertex cut, applied during the associated track selection, has the role of removing the secondary particles from the associated track sample. Secondary particles are indeed produced either from long-lived strange hadrons or from interaction of particles with the detector material. A residual contamination from secondary tracks is hence expected in the correlation distributions. This contamination is estimated from Monte Carlo simulation based on Pythia as described more in detail in the next section. The background-subtracted event-mixing corrected correlations are multiplied by a purity factor to remove this contribution.

8. **Correction for bias on B to D decay topologies** The presence of the topological cuts for the D-meson selection indirectly induce a bias on the topology of the B to D decay topologies, favouring cases with a small opening angle between the D-meson and the other tracks from the B decay. This affects the feed-down component of the data correlation distributions. This effect is corrected for with a procedure described in the subsection 3.3.3

9. **Correction for feed-down of D meson from b-hadron decay** The selection strategy employed for the D meson candidates selection enhances the fraction of reconstructed D mesons coming from the decay of a b-hadron. Typical values, with the cuts used for the D-meson selection, are of the order of 10% or less. The correlation distribution of these secondary D mesons will be sensitive to the properties of beauty jets and beauty hadron decay, which in general differ from those relative to charm jets and hadrons. The procedure used to subtract this contribution is described in the next paragraphs of this section.

10. **Study of correlation properties.** The properties of the azimuthal correlation distribution are quantified by fitting the distribution with a function composed of two Gaussian functions, modelling the near and the away side peaks, and a constant term describing the baseline. The mean of the Gaussian are fixed at $\Delta\varphi = 0$ and $\Delta\varphi = \pi$. To accomplish the 2π periodicity of the $\Delta\varphi$ variable, the Gaussian functions are “duplicated” with mean at $\Delta\varphi = 2\pi$ and $\Delta\varphi = -\pi$. The fitting procedure is described in details in Section 5.

3.1 Mass plots and cut optimization

The invariant mass distributions in the various p_T ranges studies are shown in Figure 4, 5 and 6 for D^0 , D^{*+} and D^+ respectively.

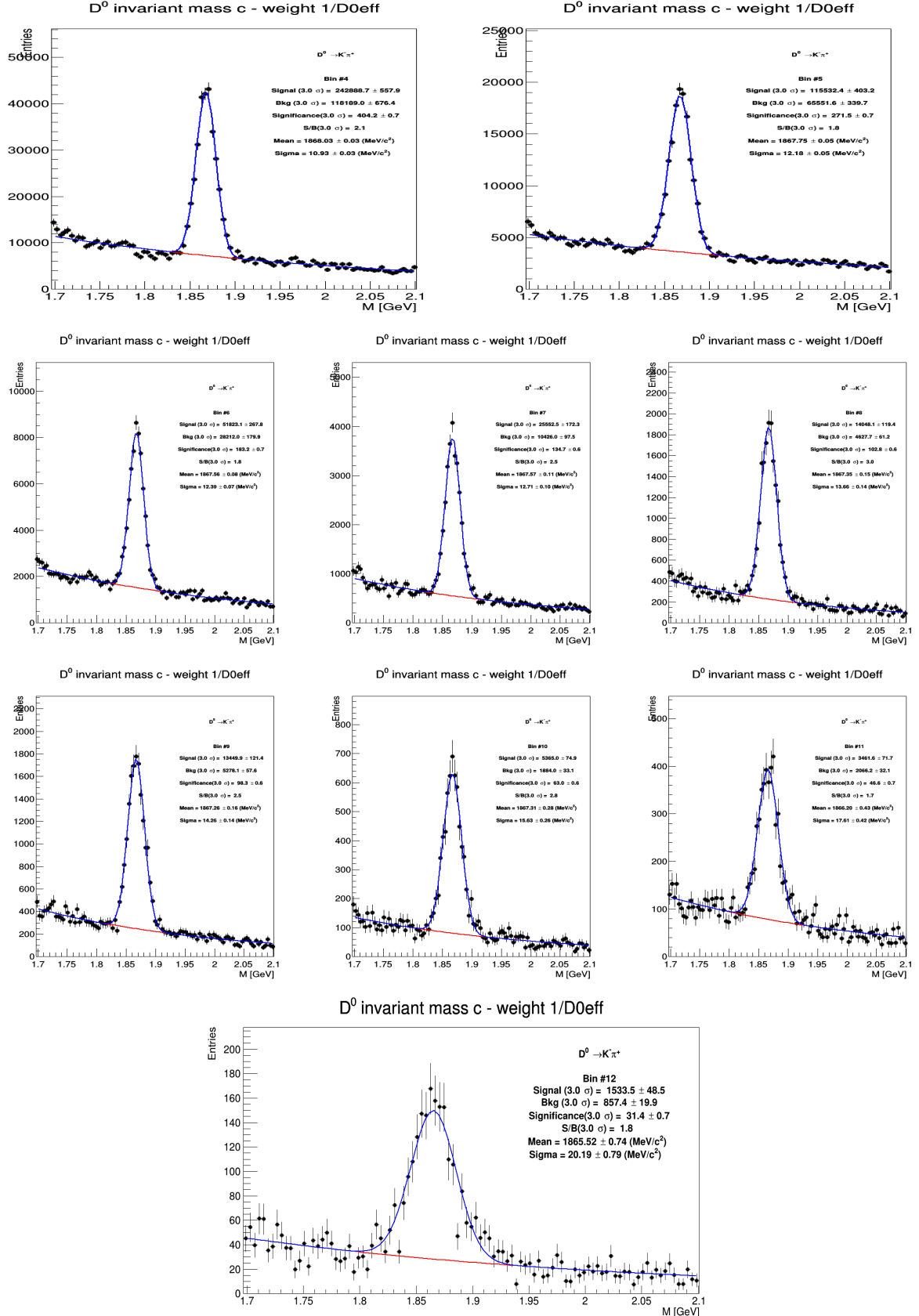


Figure 4: Invariant mass distributions of D⁰ in different p_T regions. Top: 3 < p_T^D < 4 GeV/c (left), 4 < p_T^D < 5 GeV/c (right), Mid 1: 5 < p_T^D < 6 GeV/c (left), 6 < p_T^D < 7 GeV/c (middle), 7 < p_T^D < 8 GeV/c (right); Mid2: 8 < p_T^D < 10 GeV/c, 10 < p_T^D < 12 GeV/c (middle), 12 < p_T^D < 16 GeV/c (right) and Bottom: 16 < p_T^D < 24 GeV/c.

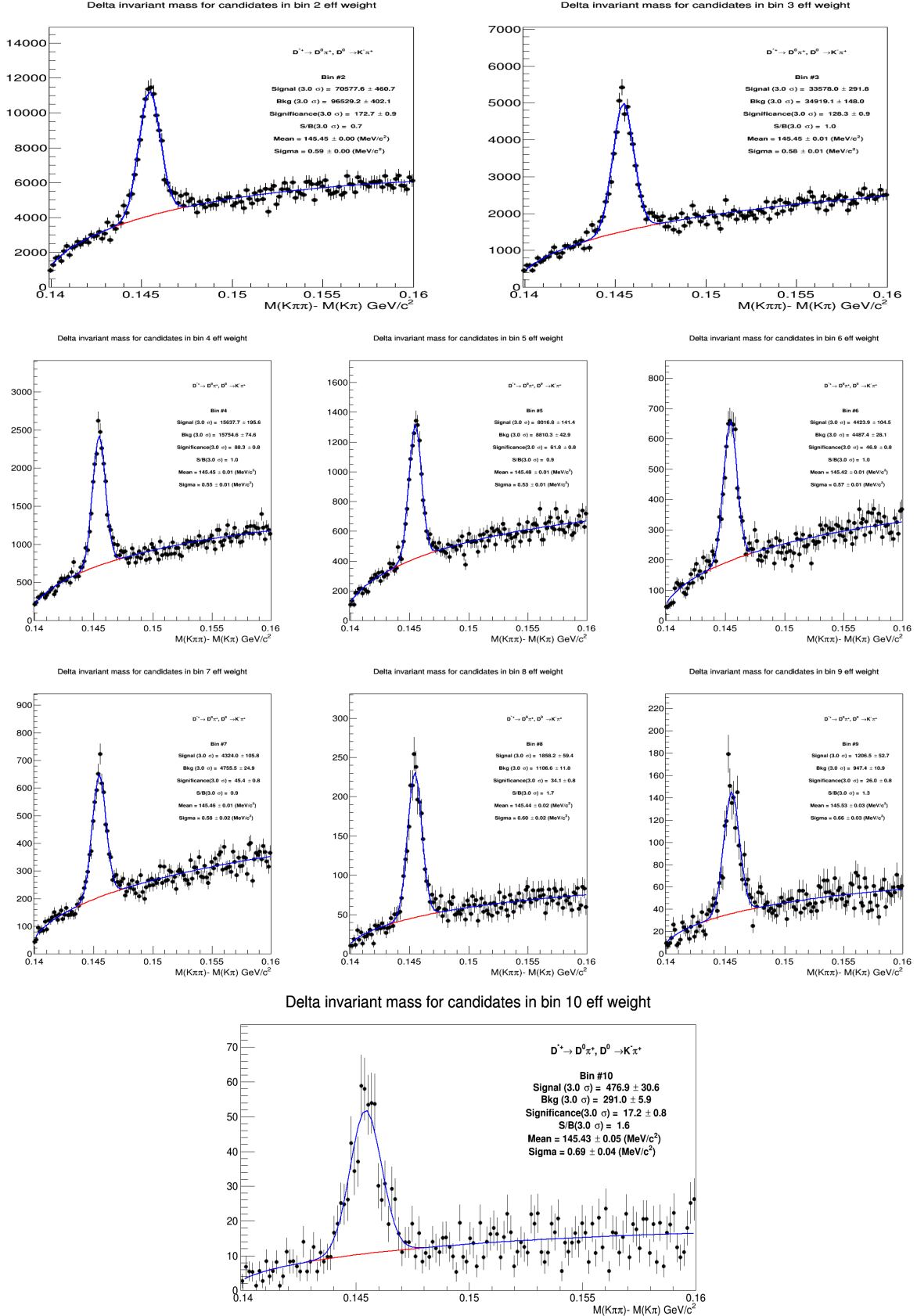


Figure 5: Invariant mass distributions of D^{*+} in different p_T^D regions. Top: $3 < p_T^D < 4$ GeV/c (left), $4 < p_T^D < 5$ GeV/c (right), Mid 1: $5 < p_T^D < 6$ GeV/c (left), $6 < p_T^D < 7$ GeV/c (middle), $7 < p_T^D < 8$ GeV/c (right); Mid2: $8 < p_T^D < 10$ GeV/c, $10 < p_T^D < 12$ GeV/c (middle), $12 < p_T^D < 16$ GeV/c (right) and Bottom: $16 < p_T^D < 24$ GeV/c .

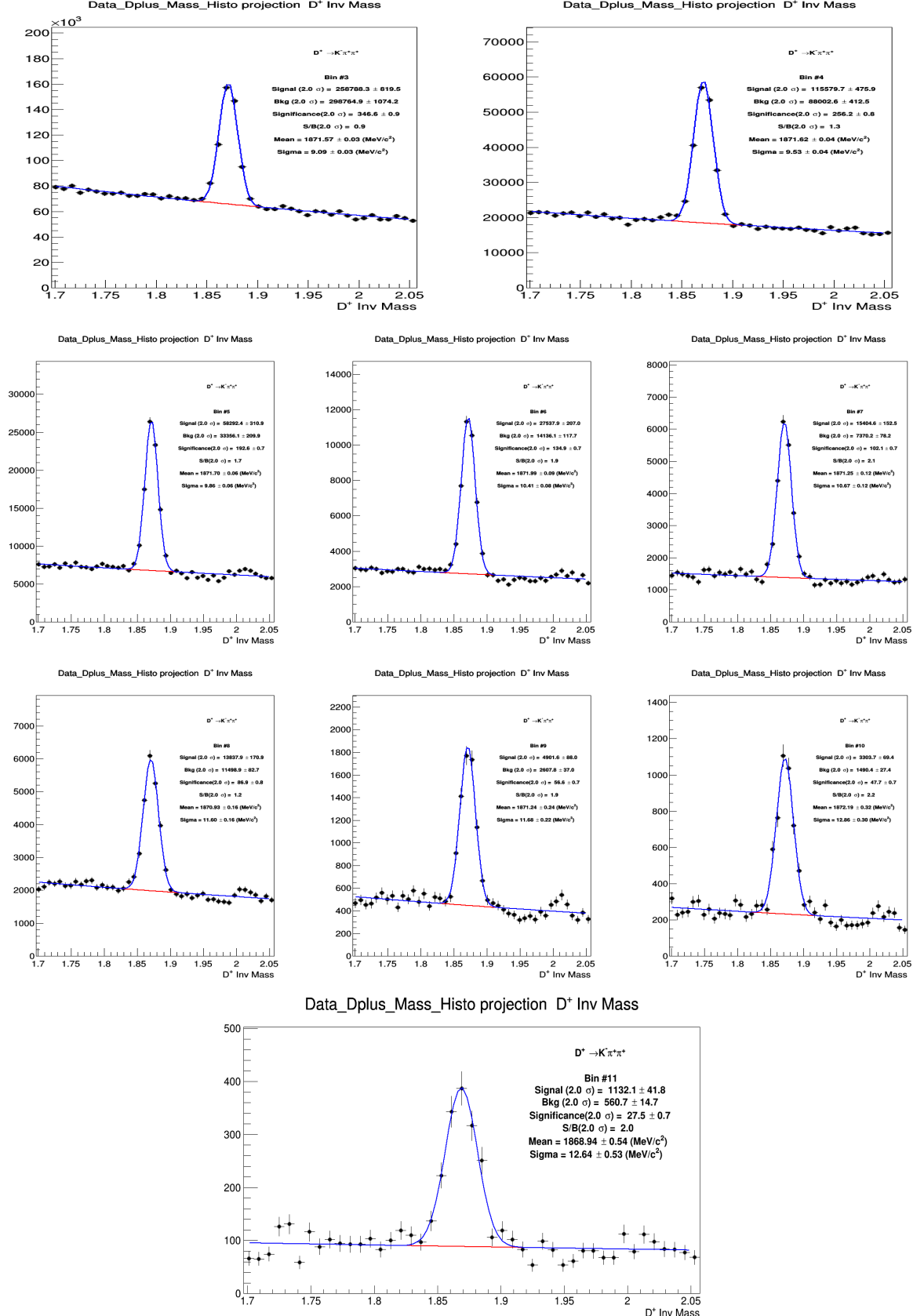


Figure 6: Invariant mass distribution of D⁺ in different p_T regions. Top: 3 < p_T^D < 4 GeV/c (left), 4 < p_T^D < 5 GeV/c (right), Mid 1: 5 < p_T^D < 6 GeV/c (left), 6 < p_T^D < 7 GeV/c (middle), 7 < p_T^D < 8 GeV/c (right); Mid2: 8 < p_T^D < 10 GeV/c, 10 < p_T^D < 12 GeV/c (middle), 12 < p_T^D < 16 GeV/c (right) and Bottom: 16 < p_T^D < 24 GeV/c .

For D^{*+} , the standard D2H p-Pb cuts (for the 2013 cross section analysis) were used. The same holds for the D^+ , but with the addition of cuts on the normalized decay length in xy plane and of the normalized difference between measured and expected daughter track impact parameters (topomatic cut). A particular cut optimization was instead performed for the D^0 meson. Twelve cut sets were tried, with the goal of increasing the S/B factor, in order to reduce fluctuations induced by the sideband subtraction (the limiting factor for the analysis performance). In Figure 7 the D^0 - h correlation distributions are shown for the different cut sets, in exemplary kinematic regions (left column), together with the bin-by-bin relative statistical uncertainty on the data points (right column). The best cut set (option G) was defined from the standard cuts used for the p-Pb 2013 cross section analysis, with a tightened selection on the cosine of the pointing angle, and with the addition of a cut on the normalized decay length in xy plane and of a selection on the normalized difference between measured and expected daughter track impact parameters (topomatic cut).

3.2 Code used for the analysis

The code used for D meson-hadron correlation analysis is fully committed in AliPhysics. The analysis classes can be found in `$ALICE_ROOT/PWGHF/correlationHF/`. The D meson specific classes where the aforementioned steps are carried out are `AliAnalysisTaskDStarCorrelations`, `AliAnalysisTaskSED0Correlations` and `AliAnalysisTaskDplusCorrelations`. The classes which are common to the D meson specific analysis which includes the associated particle cuts and the correlation observables are `AliHFAssociatedTrackCuts`, `AliHFCorrelator`, `AliHFOfflineCorrelator`, `AliReducedParticle` and `AliDhCorrelationExtraction`. Several additional classes and macros in the same folder deal with the correction steps.

3.3 Further details on corrections

3.3.1 Event Mixing

The event-mixing technique is used for correcting the raw correlation distribution for effects arising from the detector limited acceptance in rapidity and detector spatial inhomogeneities. The calculation of the Event Mixing correlation distribution is performed online. An event pool is created, where events preceding the one containing a D candidate are stored based on their properties (position of the vertex along the z axis and multiplicity). Each time a D meson candidate is found in an event, only the events contained in the same pool as the event under analysis is used to evaluate the correlations for the event mixing correction.

For D^0 and D^+ , an offline approach for the mixed-event correction has been developed. In this approach, D-meson triggers and associated tracks from every analyzed event are stored in dedicated TTree, together with the needed kinematic information to build correlation distributions, and with identifiers of the events to which they belong. In this way, it is possible to correlate each D meson with all the tracks belonging to the same pool over the full event sample, and not being limited to the same subjob as for the online analysis. This allows to increase the statistics of the mixed-event correlation distributions. It was verified that online and offline approaches are fully compatible within the statistical uncertainties.

The multiplicity and z vertex position bins for the pools used in the p-Pb analysis (for both approaches) are the following:

- Multiplicity bins: $(0, 40); (40, 65); (65, +\infty)$ (THESE ARE BEING SLIGHTLY CHANGED)
- Vertex z (cm) = $(-10, -2.5); (-2.5, 2.5); (2.5, 10)$ (THESE ARE BEING SLIGHTLY CHANGED)

In an ideal case, the mixed event distribution is expected to have a constant flat distribution as function of $\Delta\varphi$ and a triangular shaped distribution in $\Delta\eta$ deriving from the limited η acceptance of the detector.

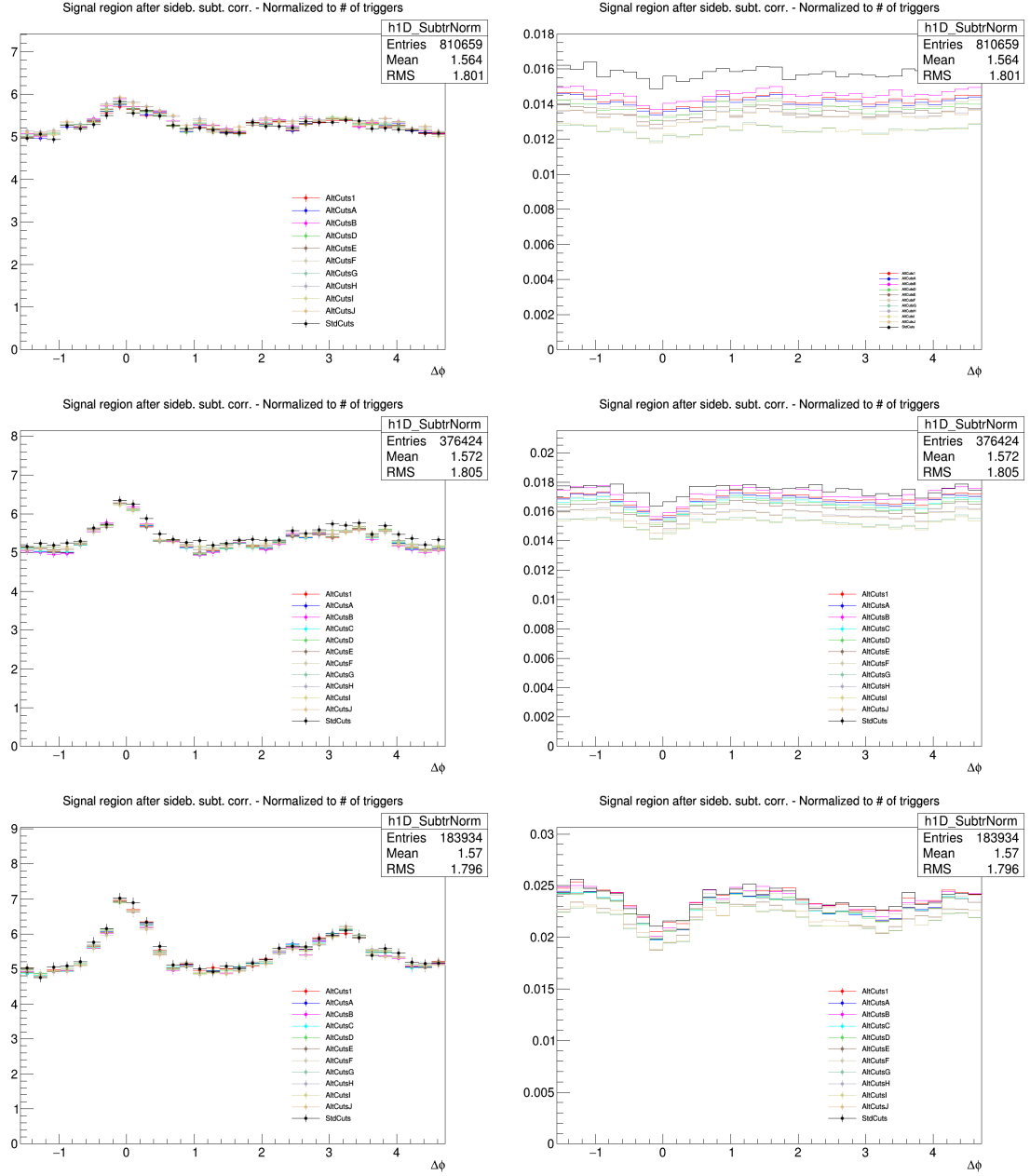


Figure 7: D^0 - h correlation distributions with different cut options (left) and point-by-point relative statistical uncertainty (right) for $3 < p_T^D < 5 \text{ GeV}/c$ (top), $5 < p_T^D < 8 \text{ GeV}/c$ (middle), $8 < p_T^D < 16 \text{ GeV}/c$ (bottom), in all cases with associated track $p_T > 0.3 \text{ GeV}/c$.

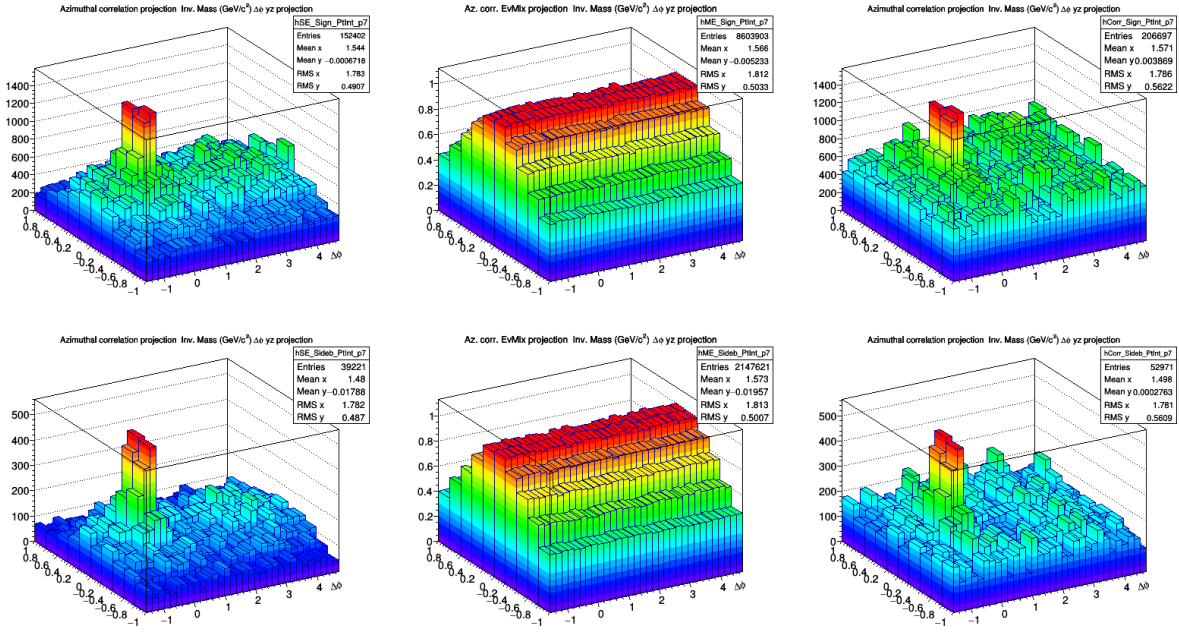


Figure 8: D^0 meson ($\Delta\varphi, \Delta\eta$) correlation for in the signal region (top row) and sidebands (bottom row) from Single Event (left) and Mixed Event analysis (center) for high p_T : $8 < p_T < 16$ GeV/c with associated $p_T > 0.3$ GeV/c. The right column shows the SE/ME corrected distributions.

278 In case, instead of detector inefficient regions, or holes, in the same angular position for D meson and
 279 associated tracks, these structures produce an excess of correlations at $\Delta\varphi = 0$ in the $\Delta\varphi$ distribution. The
 280 obtained distribution is used as a weight in each correlation bin, i.e, the corrected correlation distribution
 281 is calculated as follows:

$$\frac{dN^{corr}(\Delta\varphi, \Delta\eta)}{d\Delta\varphi d\Delta\eta} = \frac{\frac{dN^{SE}(\Delta\varphi, \Delta\eta)}{d\Delta\varphi d\Delta\eta}}{\frac{dN^{ME}(\Delta\varphi, \Delta\eta)}{d\Delta\varphi d\Delta\eta}} \frac{dN^{ME}(0, 0)}{d\Delta\varphi d\Delta\eta} \quad (2)$$

282 In the previous equation, the last term stands for the average of the bins in the region $-0.2 < \Delta\eta < 0.2$,
 283 $-0.2 < \Delta\varphi < 0.2$ (multiple bins are used to minimize the effect of statistical fluctuations on the normaliza-
 284 tion of the mixed-event plots). This kind of normalization, adopted in the analysis of hadron-hadron
 285 correlations, relies on the fact that at $(\Delta\eta, \Delta\varphi) = (0, 0)$ the trigger and associated particle experience
 286 the same detector effects. In the D meson case this is true only on average and not at very low p_T ,
 287 since D mesons are reconstructed from particles that can go in different detector region. However,
 288 $(\Delta\eta, \Delta\varphi) = (0, 0)$ is in any case the region with maximum efficiency for the pairs (both correlated and
 289 uncorrelated). Thus the same convention was adopted.

290 The mixed-event correlation distributions are built in both D meson signal and sideband regions. Both
 291 are corrected with the relative distributions. An example of the mixed-event distributions, and of the
 292 outcome of the mixed-event correction, is provided in Figures 8 and 9. The expected triangular shape
 293 in $\Delta\eta$, for the mixed-event distributions, addresses the effect of the limited detector pseudo-rapidity
 294 acceptance. Note that the mixed-event distribution is limited to the interval $|\Delta\eta| < 1$: the decision to
 295 limit the mixed-event correction, and thus the whole analysis, to this range was taken in order to avoid
 296 the so-called “wing effect”, i.e. the wing-like structures arising in the correlation distribution at large $\Delta\eta$
 297 due to the limited filling of the correlation bins in that region.

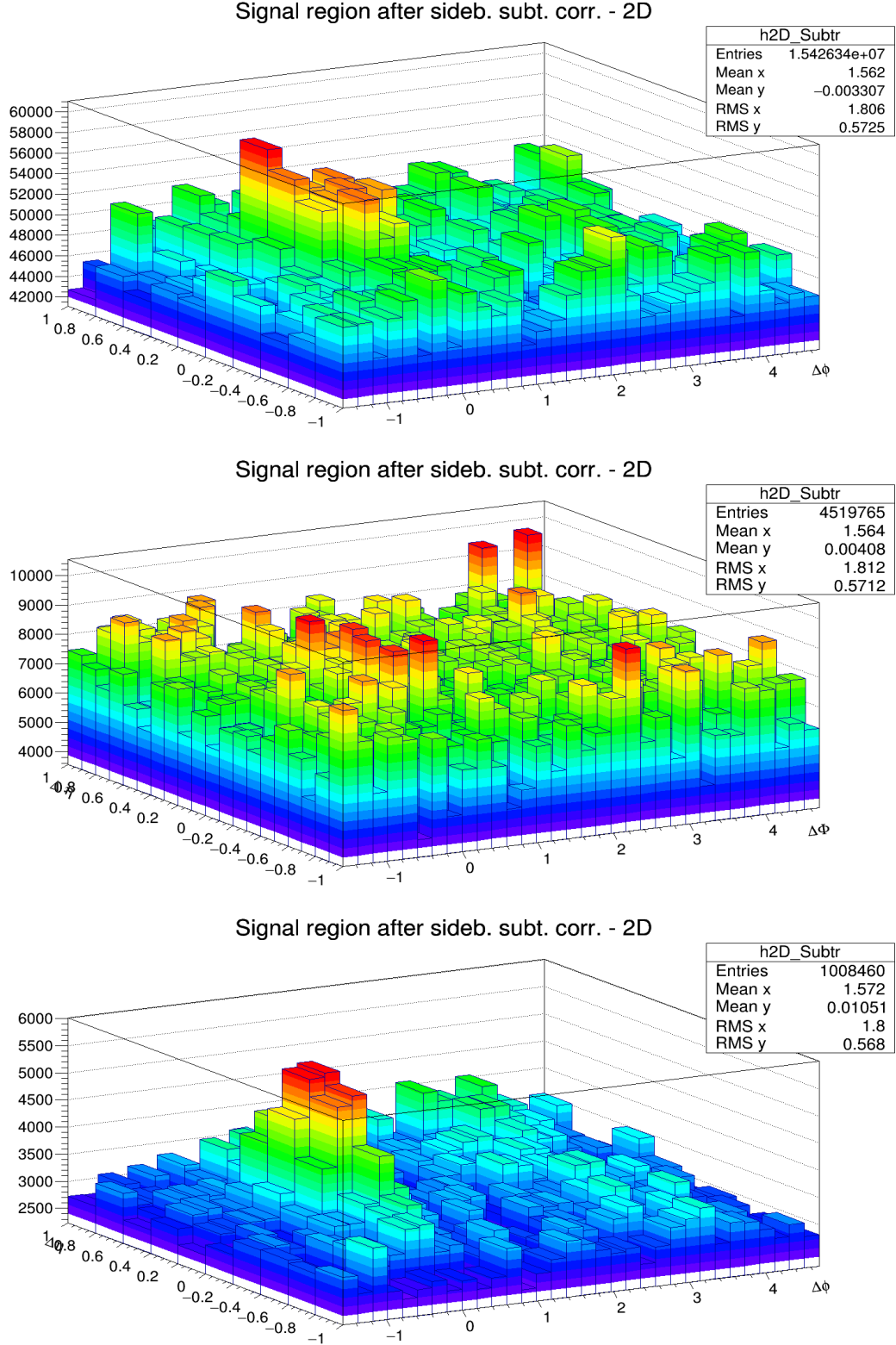


Figure 9: Top: $(\Delta\phi, \Delta\eta)$ correlation distribution of D^0 -h with $3 < p_T < 5$ GeV/c and associated track kinematic range: $0.3 < p_T < 1.0$ GeV/c Mid: $(\Delta\phi, \Delta\eta)$ correlation distribution of D^{*+} -h with $3 < p_T < 5$ GeV/c and associated track p_T Threshold: $p_T > 0.3$ GeV/c Bottom: $(\Delta\phi, \Delta\eta)$ correlation distribution of D^+ -h with $8 < p_T < 16$ GeV/c and associated track p_T threshold: $p_T > 0.3$ GeV/c. All the plots are shown after the mixed-event correction and the sideband subtraction.

298 **3.3.2 Tracking and D-meson trigger efficiency**

299 **(i) Tracking efficiency** - The tracking efficiency was calculated by obtaining the ratio between the yield
 300 at the reconstructed level and generated level, for a defined “type” of particles (in our case non-identified
 301 particles) and it is estimated differentially in p_T , η , and z_{vtx} of the event.

302
 303 Tracking efficiency maps were produced as TH3D histograms (p_T , η , z_{vtx}) obtained from MC analysis on
 304 the minimum-bias samples LHC17f2b_fast and LHC17f2b_cent_woSDD, and applying at reconstructed
 305 level the track selections (summarized in Table. 2). These efficiency maps were used in the analysis
 306 tasks to extract single track efficiencies; each correlation pairs found in the data analysis was inserted
 307 in correlation plots with a weight of **1/efficiency value**. Plots of the p_T dependence of the tracking
 308 efficiency for two different track selections are shown in Fig. 10.

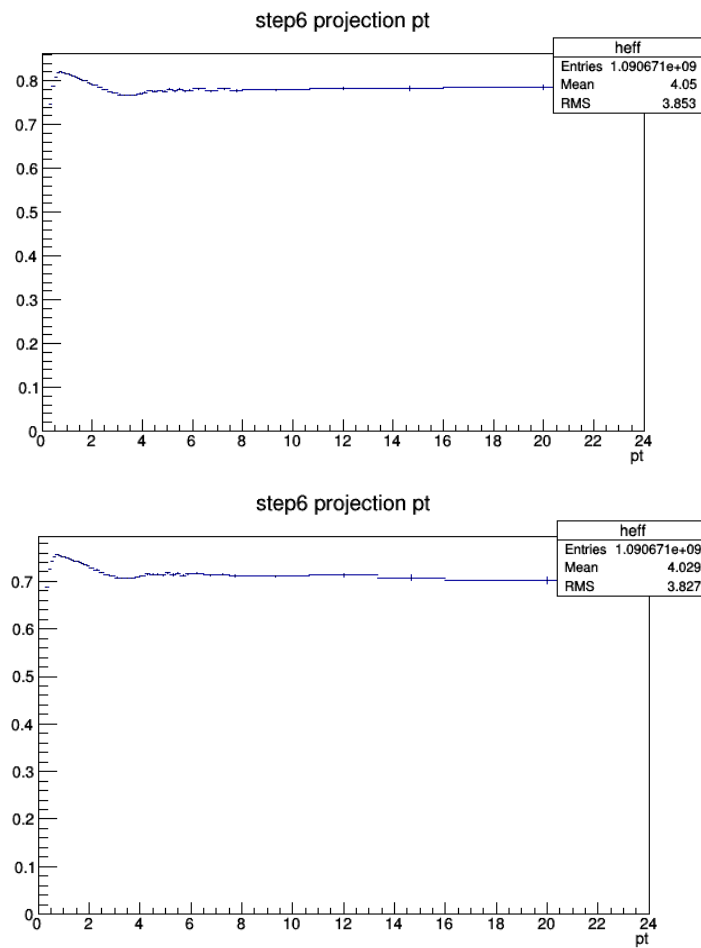


Figure 10: p_T efficiency map for standard track selection (2 ITS clusters) on top panel, and alternate track selection, used for systematics (3 ITS clusters, filterbit4, ITS refit) on bottom panel.

309 Details of cuts at event level and particle selection at different steps are listed in Table 2 .

MC Generated	
Stages	Cuts
1. MC Part with Generated Cuts	After Event Selection Charge PDG Code Physical Primary Kinematics Cuts $-0.8 < \eta < 0.8$ $pT > 0.3 \text{ (GeV}/c)$
2. MC Part with Kine Cuts	
MC Reconstructed	
4. Reco tracks	After Event Selection Physical Primary Kinematics Cuts $-0.8 < \eta < 0.8$ $pT > 0.3 \text{ (GeV}/c)$ Quality Cuts SetRequireSigmaToVertex(kFALSE) SetDCAToVertex2D(kFALSE) SetMinNCrossedRowsTPC(70) SetMinRatioCrossedRowsOverFindableClustersTPC(0.8) SetMinNClustersITS(2) SetMaxChi2PerClusterTPC(4) SetMaxDCAToVertexZ(1) SetMaxDCAToVertexXY(1) SetRequireTPCRefit(TRUE) SetRequireITSRefit(FALSE) Same as step 6
5. Reco tracks with Kine Cuts	
6. MC true with Quality Cuts	
7. Reco tracks with Quality Cuts	

Table 2: Single Track Efficiency cuts detail

310

311 **(ii) D Meson efficiency** - Due to limited statistics, the correlation analysis is performed in quite wide p_T
 312 bins and in each of them the reconstruction and selection efficiency of D mesons is not flat, in particular
 313 in the lower p_T region. We correct for the p_T dependence of the trigger efficiency within each p_T -bin.

314 This correction is applied online, by using a map of D meson efficiency as a function of p_T and event
 315 multiplicity (in terms of SPD tracklets in $|\eta| < 1$) extracted from the enriched Monte Carlo sample
 316 LHC17d2a_fast_new. The η dependence was neglected due to the statistics of the available Monte Carlo
 317 sample, which avoided the possibility of performing a 3D study.

318 To properly count the number of trigger particles used to normalize the correlation distributions, N_{trig} ,
 319 each D meson is weighted with the inverse of its efficiency in the invariant mass distribution. The main
 320 role of the correction for the D meson efficiency is to account for the p_T dependence of the correlation
 321 distribution within a given D meson p_T interval. Indeed, only the p_T shape of the D meson efficiency
 322 within the correlation p_T^{trig} ranges is relevant while the average value in the p_T range is simplified due to
 323 the normalization of the correlation distribution to the number of trigger particles.

It was observed that multiplicity dependence of the efficiency does not bias the extraction of the signal yield from the invariant mass distributions (which, as anticipated, are also weighted in the same manner). Efficiency plots for D^0 , D^+ and D^{*+} mesons are shown in Figs. 11 and 12.

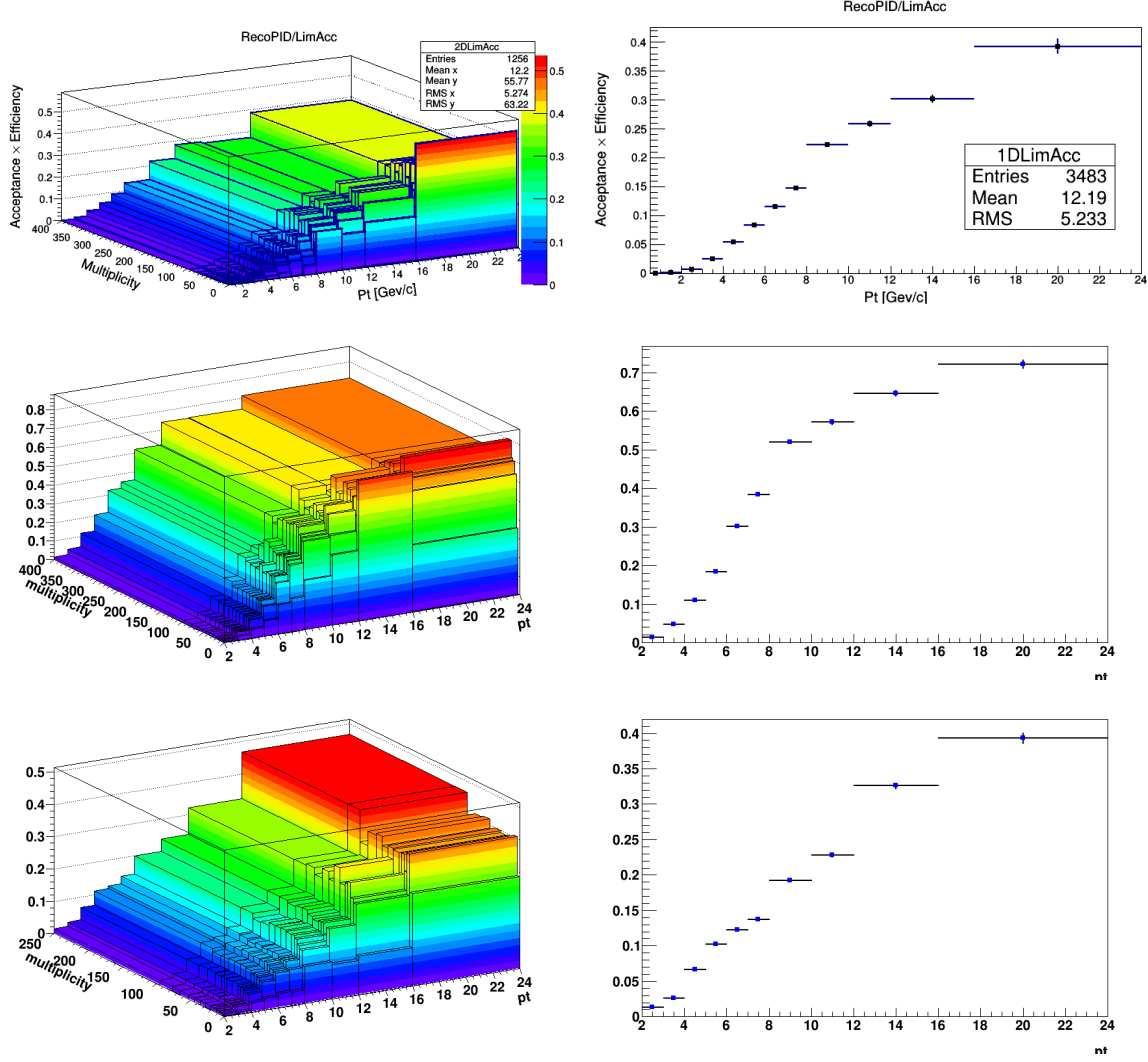


Figure 11: Top panel: (p_T , multiplicity) dependence (left) and p_T dependence (right) of prompt D^+ meson efficiency. Mid panel: (p_T , multiplicity) dependence (left) and p_T dependence (right) of prompt D^{*+} meson efficiency. Bottom panel: (p_T , multiplicity) dependence (left) and p_T dependence (right) of prompt D^0 meson efficiency.

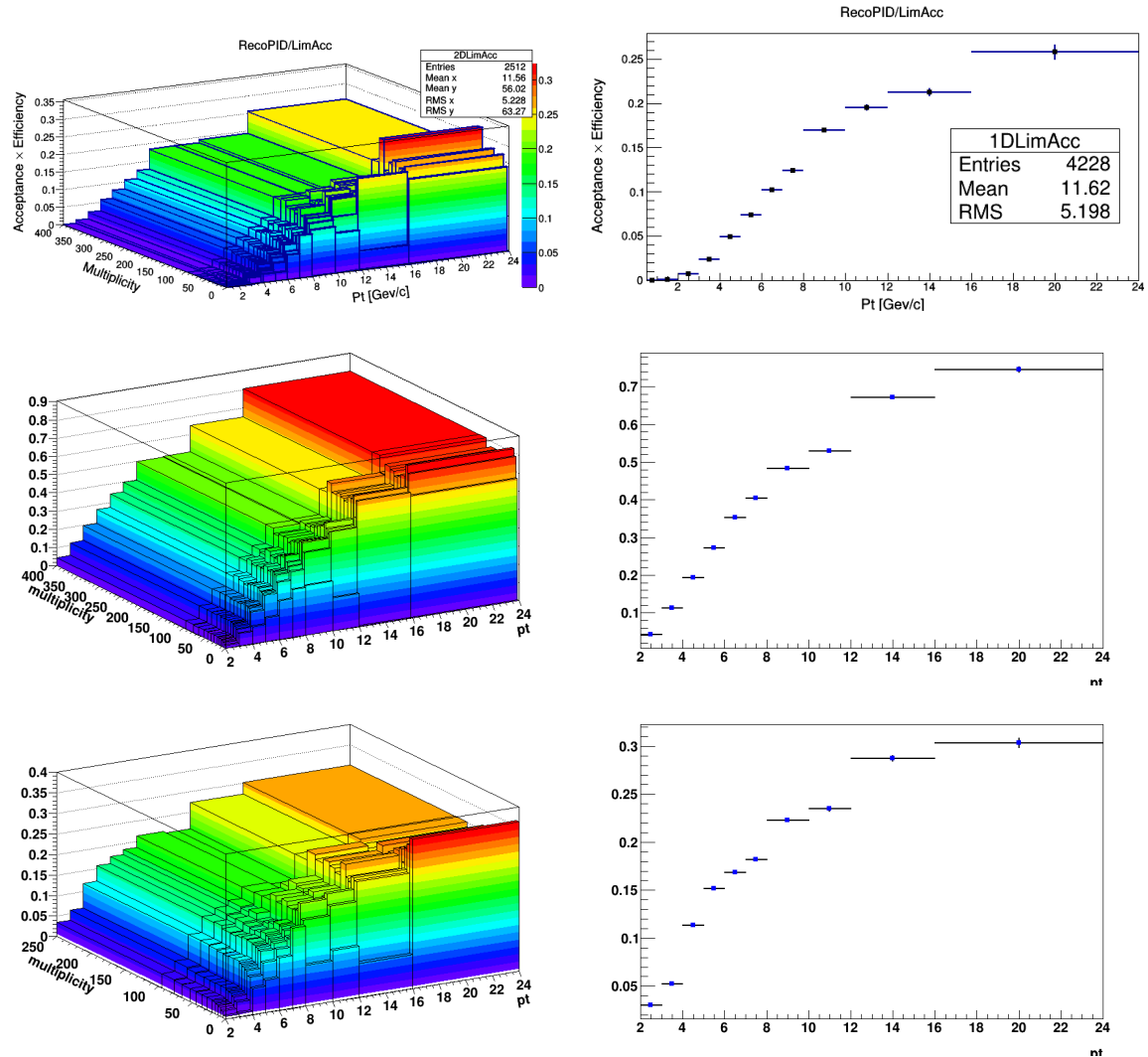


Figure 12: Top panel: (p_T , multiplicity) dependence (left) and p_T dependence (right) of feed-down D^+ meson efficiency. Mid panel: (p_T , multiplicity) dependence (left) and p_T dependence (right) of feed-down D^{*+} meson efficiency. Bottom panel: (p_T , multiplicity) dependence (left) and p_T dependence (right) of feed-down D^0 meson efficiency.

3.3.3 Correction for bias on B to D decay topologies

328 To verify the consistency of the analysis chain and of the corrections applied to the correlation distributions extracted from data, a Monte Carlo closure test was developed and tried on the D^0 - h analysis.

330 On the Monte Carlo enriched with charm and beauty quarks (LHC17d2a.fast_new), the correlation analysis was performed both at kinematic level and at reconstructed level. At kinematic level, only acceptance cuts were applied on the D mesons and the associated particles, using the Monte Carlo information for the identification of the D mesons and the hadrons in the event and rejecting the non-primary particles.

331 At reconstructed level, the analysis was performed as if it were executed on data, applying the event selection, the acceptance cuts for D mesons and the associated particles, selecting the D meson candidates with filtering cuts on their daughters, topological cuts and PID selection, and then keeping only the true D mesons by looking at the Monte Carlo truth; non-primary particles were rejected by means of the DCA selection. Event mixing correction was applied both at reconstructed and at kinematic level, where it takes into account just the effects of the acceptance cuts. In addition, at reconstructed level also tracking efficiency and trigger efficiency correction were applied.

341 Examples of correlation plots at both steps are shown in Figure 13 and 14, separating the contribution of associated tracks and D mesons from different origins to the correlation distribution, as described in the legend of the plots.

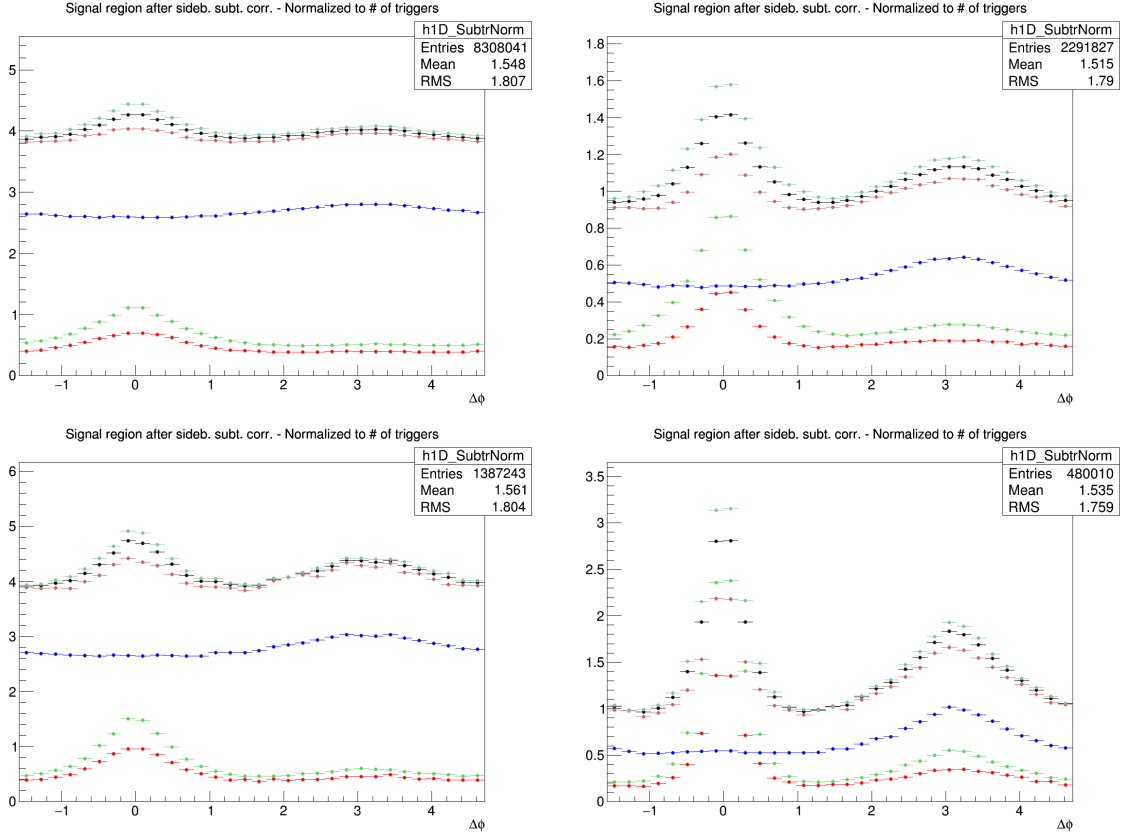


Figure 13: D^0 -hadrons azimuthal correlation distribution obtained from Monte Carlo, at kinematic step. Black points: All D^0 -all hadrons, normalized by all D^0 triggers; light red points: D^0 from c-hadrons from c, normalized by c- D^0 triggers; dark red points: D^0 from c-all hadrons, normalized by c- D^0 triggers; light green points: D^0 from b-hadrons from b, normalized by b- D^0 triggers; dark green points: D^0 from b-all hadrons, normalized by b- D^0 triggers; blue points: All D^0 -hadrons from light quarks, normalized by all D^0 triggers. The panels show the ranges: $3 < p_T(D) < 5 \text{ GeV}/c$, $0.3 < p_T(\text{assoc}) < 1 \text{ GeV}/c$ (top-left); $3 < p_T(D) < 5 \text{ GeV}/c$, $p_T(\text{assoc}) > 1 \text{ GeV}/c$ (top-right); $8 < p_T(D) < 16 \text{ GeV}/c$, $0.3 < p_T(\text{assoc}) < 1 \text{ GeV}/c$ (bottom-left); $8 < p_T(D) < 16 \text{ GeV}/c$, $p_T(\text{assoc}) > 1 \text{ GeV}/c$ (bottom-right).

344 The consistency check we performed was to verify whether, after having applied all the corrections to the
 345 azimuthal correlation plots at reconstructed level, the results were compatible with the ones at kinematic
 346 level. Hence, the ratios of fully corrected reconstructed plots over kinematic plots were evaluated in all
 347 the D^0 p_T bins and for the various p_T thresholds for the associated tracks, separating the contributions for
 348 the different origins of particles and triggers. The ratios, shown in Figure 15, denote a good compatibility
 349 with 1, within the uncertainties, with the only exception being due to some structures in the near side
 350 region for the beauty origin case. These structures were already found in the pp 2010 and p-Pb 2013
 351 analysis, and it was verified that they are induced our topological selection for the D mesons. Indeed, in
 352 cases in which the D meson triggers come from B hadrons, applying the topological cuts (especially the
 353 cosine of the pointing angle) tends to favour cases with a small angular opening between the products of
 354 the B hadron decay (i.e. the D meson trigger itself and other particles), with respect to cases where the
 355 B decay particles are less collinear.

356 In the Monte Carlo closure test, this situation is reflected in the correlation distributions at reconstructed
 357 level, where the topological selection is applied, while it does not occur at kinematic level. Hence, in
 358 the reconstructed/kinematic ratio, the distribution would show an excess for $\Delta\phi = 0$ (due to the favoured
 359 decays with small opening angle), which is then compensated by a depletion for larger values of $\Delta\phi = 0$

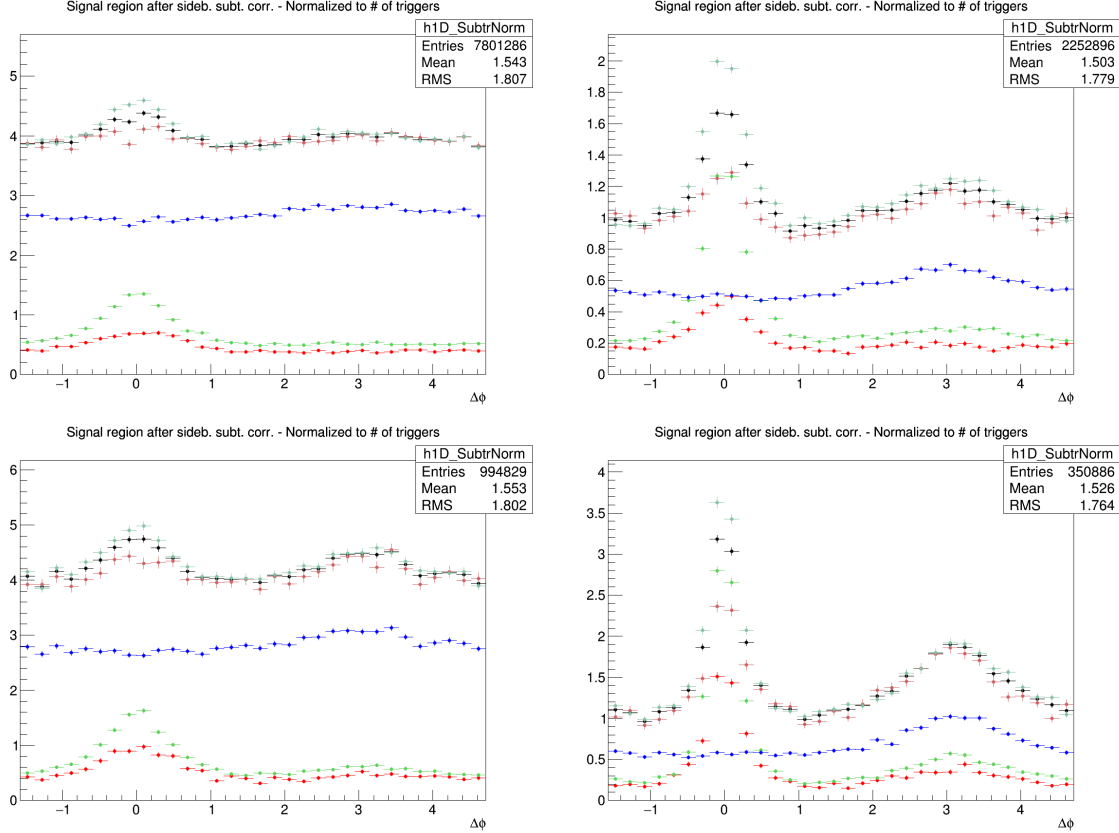


Figure 14: D^0 -hadrons azimuthal correlation distribution obtained from Monte Carlo, at reconstructed step. Black points: All D^0 -all hadrons, normalized by all D^0 triggers; light red points: D^0 from c-hadrons from c, normalized by c- D^0 triggers; dark red points: D^0 from c-all hadrons, normalized by c- D^0 triggers; light green points: D^0 from b-hadrons from b, normalized by b- D^0 triggers; dark green points: D^0 from b-all hadrons, normalized by b- D^0 triggers; blue points: All D^0 -hadrons from light quarks, normalized by all D^0 triggers. The panels show the ranges: $3 < p_T(D) < 5 \text{ GeV}/c$, $0.3 < p_T(\text{assoc}) < 1 \text{ GeV}/c$ (top-left); $3 < p_T(D) < 5 \text{ GeV}/c$, $p_T(\text{assoc}) > 1 \text{ GeV}/c$ (top-right); $8 < p_T(D) < 16 \text{ GeV}/c$, $0.3 < p_T(\text{assoc}) < 1 \text{ GeV}/c$ (bottom-left); $8 < p_T(D) < 16 \text{ GeV}/c$, $p_T(\text{assoc}) > 1 \text{ GeV}/c$ (bottom-right).

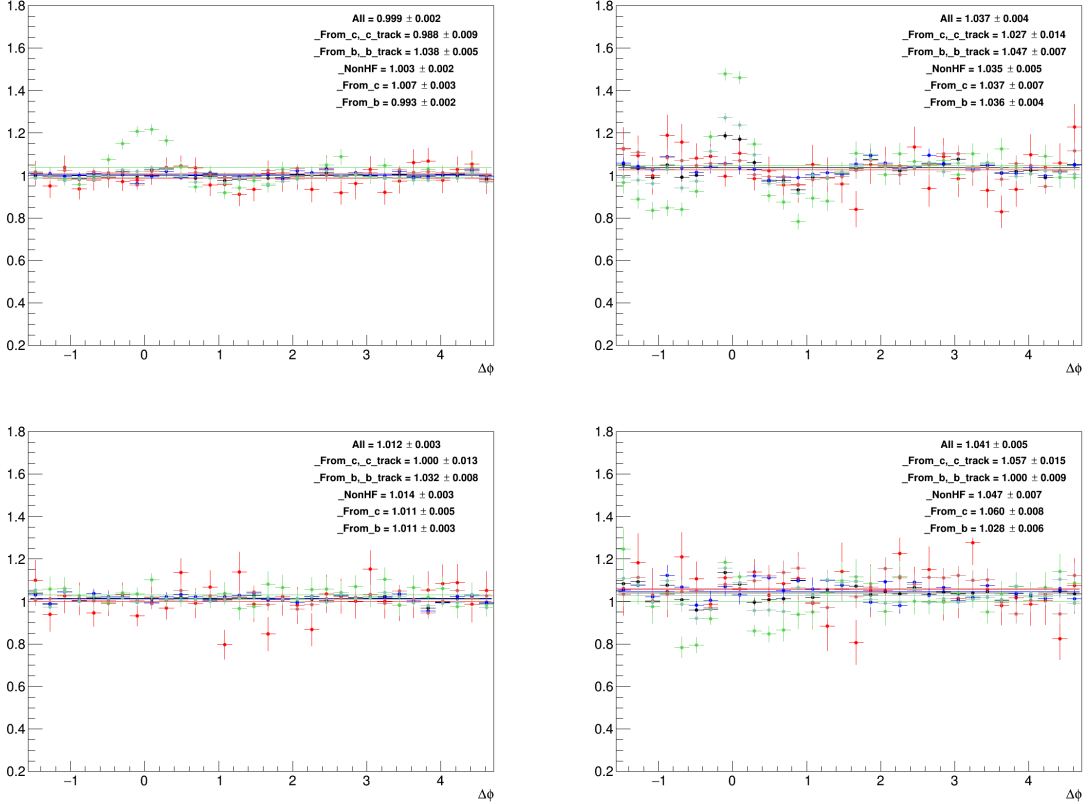


Figure 15: Ratios of fully corrected azimuthal correlation plots at reconstructed level over azimuthal correlation plots at kinematic level, in the two D^0 p_T bins, for the different associated p_T ranges. Black points: All D^0 -all hadrons, normalized by all D^0 triggers; light red points: D^0 from c-hadrons from c, normalized by c- D^0 triggers; dark red points: D^0 from c-all hadrons, normalized by c- D^0 triggers; light green points: D^0 from b-hadrons from b, normalized by b- D^0 triggers; dark green points: D^0 from b-all hadrons, normalized by b- D^0 triggers; blue points: All D^0 -hadrons from light quarks, normalized by all D^0 triggers. The panels show the ranges: $3 < p_T(D) < 5 \text{ GeV}/c$, $0.3 < p_T(\text{assoc}) < 1 \text{ GeV}/c$ (top-left); $3 < p_T(D) < 5 \text{ GeV}/c$, $p_T(\text{assoc}) > 1 \text{ GeV}/c$ (top-right); $8 < p_T(D) < 16 \text{ GeV}/c$, $0.3 < p_T(\text{assoc}) < 1 \text{ GeV}/c$ (bottom-left); $8 < p_T(D) < 16 \text{ GeV}/c$, $p_T(\text{assoc}) > 1 \text{ GeV}/c$ (bottom-right).

(corresponding to B decays with larger angles, which are disfavoured). These structures are prominent at low $D^0 p_T$, where the topological cuts are tighter, and tend to disappear at higher p_T , where the selections are released. They are also larger in the higher associated track p_T ranges, where the fraction of B-hadron decay tracks dominate the overall correlation distributions.

The data correlation distribution need to be corrected for this bias, and in particular for the enhancement of b-origin correlation pairs at the centre of the near side region, which would influence the near-side peak features. In order to do this, the amount of the b-origin excess is evaluated from the Reco/Kine ratio, by considering the b- D^0 -all tracks case (dark green points). The excess at Reco level (affecting data) is quantified as a $\Delta\varphi$ modulation **modul** for the five points an each side of the $\Delta\varphi = 0$ value (or, equivalently, on the first five points of the reflected distributions, which start from $\Delta\varphi = 0$). This is done separately in each p_T range. Then, the correction is done by applying this modulation to the data correlation distributions, but taking into account that only the correlation entries from B \rightarrow D are affected, while the c \rightarrow D correlations need to be left unaltered. In particular, it has to be considered that:

- On data, the B \rightarrow D correlation pairs are only a fraction ($1-f_{\text{prompt}}$) of the total.
- The amplitude of B \rightarrow D|_{amplit} correlation pattern is different (greater) than the amplitude of the c \rightarrow D|_{amplit} correlation pattern:

Thus, the following equation is applied to get the corrected $C(\Delta\varphi)_{\text{corr}}$ data points starting from the raw ones, $C(\Delta\varphi)_{\text{raw}}$:

$$C(\Delta\varphi)_{\text{corr}} = C(\Delta\varphi)_{\text{raw}} \cdot \left[\frac{c \rightarrow D|_{\text{amplit}}}{(B+c) \rightarrow D|_{\text{amplit}}} \cdot f_{\text{prompt}} + \frac{B \rightarrow D|_{\text{amplit}}}{(B+c) \rightarrow D|_{\text{amplit}}} \cdot (1 - f_{\text{prompt}}) \cdot \frac{1}{\mathbf{modul}} \right] \quad (3)$$

where $(B+c) \rightarrow D|_{\text{amplit}} = c \rightarrow D|_{\text{amplit}} \cdot f_{\text{prompt}} + B \rightarrow D|_{\text{amplit}} \cdot (1 - f_{\text{prompt}})$, and where the two amplitudes are evaluated from the Monte Carlo distributions of Figure 14 at reconstructed level (so, including the bias), and f_{prompt} with the procedure described in 3.3.5. Applying the **modul** factor to the beauty part of the data correlation distributions brings its value back to the generated level case, effectively removing the bias. The effect of the correction is a shift of the data points in the near-side region (in general, downward in the first and second points, the upward in the others). The maximum value of the shift is of about 5%, at the centre of the near-side peak, for the lowest D-meson p_T range ($5 < p_T < 8 \text{ GeV}/c$) and the highest associated track p_T range ($p_T > 3 \text{ GeV}/c$). The typical values are instead of a couple of percentage points. The correction is zero in the highest D-meson p_T range. To take into account for possible inaccuracies in the definition of the modulations, or in their rescaling, a systematic uncertainty is applied on the corrected data points, with value $|C(\Delta\varphi)_{\text{corr}} - C(\Delta\varphi)_{\text{raw}}|/\sqrt{12}$, on each side of the data points affected by the bias (symmetric uncertainty).

390 **3.3.4 Secondary track contamination**

391 The secondary tracks inside the associated track sample, due to interaction of primary track with the de-
 392 tector material or to decays of strange hadrons, are mostly removed by the DCA cuts applied during the
 393 cut selection phase ($\text{DCA}(xy) < 1 \text{ cm}$, $\text{DCA}(z) < 1 \text{ cm}$). Anyway, a small fraction of secondary tracks
 394 survives this cut, and the data correlation distributions have to be corrected for this residual contam-
 395 ination. The fraction of surviving secondary tracks is evaluated via a study on the LHC17d2a_fast_new
 396 sample, by counting the number of tracks accepted by the selection whose corresponding generated-
 397 level track doesn't satisfy the `IsPhysicalPrimary()` call, and dividing this number by the total nummer
 398 of accepted tracks. The outcome of the check is reported in Figure 16. As it's visible, no more than
 399 5% secondary tracks pass the selection. Moreover, the fraction of residual secondary tracks is flat along
 400 the $\Delta\phi$ axis, as shown, for exemplary p_T regions, in Figure 17, where the inhomogeneities are always
 401 below 1%. For this reason, it is possible to directly scale the data correlation distributions by their purity
 402 fraction (i.e. 1 - secondary contamination). This is done with an associated p_T dependence, due to the
 403 increase of the purity with the track p_T , while the purity fraction is taken flat versus the D-meson p_T .
 404 The purity values that were choosen are the following:

- 405 – $p_T(\text{assoc}) > 0.3 \text{ GeV}/c$: 0.958
- 406 – $p_T(\text{assoc}) > 1 \text{ GeV}/c$: 0.973
- 407 – $0.3 < p_T(\text{assoc}) < 1 \text{ GeV}/c$: 0.953
- 408 – $1 < p_T(\text{assoc}) < 2 \text{ GeV}/c$: 0.969
- 409 – $2 < p_T(\text{assoc}) < 3 \text{ GeV}/c$: 0.982
- 410 – $p_T(\text{assoc}) > 3 \text{ GeV}/c$: 0.990

411 It was also verified with the same Monte Carlo study that applying the DCA selection rejects less than
 412 0.2% primary tracks (tagged as false positives) from the associated track sample, again with a flat az-
 413 imuthal distribution, inducing hence a fully negligible bias on the data correlation distributions. This is
 414 shown in Figure 18. This was also verified for specific charm-origin and beauty-origin tracks, due to
 415 their larger DCA with respect to primary tracks from light quarks. In this case, the fraction of rejected
 416 charm and beauty tracks stays below 1% in all the kinematic ranges apart from the associated track p_T
 417 regions 0.3-1 and $> 0.3 \text{ GeV}/c$, where the rejection can be as high as 2%. In these kinematic ranges,
 418 though, the data correlation distributions are dominated by non-heavy-flavour tracks, as it was verified
 419 from the simulations, hence the overall bias is still contained below 1%, thus negligible.

420 These studies were performed on an enriched Monte Carlo sample, which could not fully reproduce
 421 the relative abundancies of the species. Anyway, for events with a reconstructed D-meson, this bias is
 422 expected to be minor, and only these events are used in the data analysis. In any case, the percentages
 423 obtained from the study were found to be consistent within 1% with the outcome of the studies for the
 424 p-Pb 2013 analysis, which reassures us on the full validity of these results.

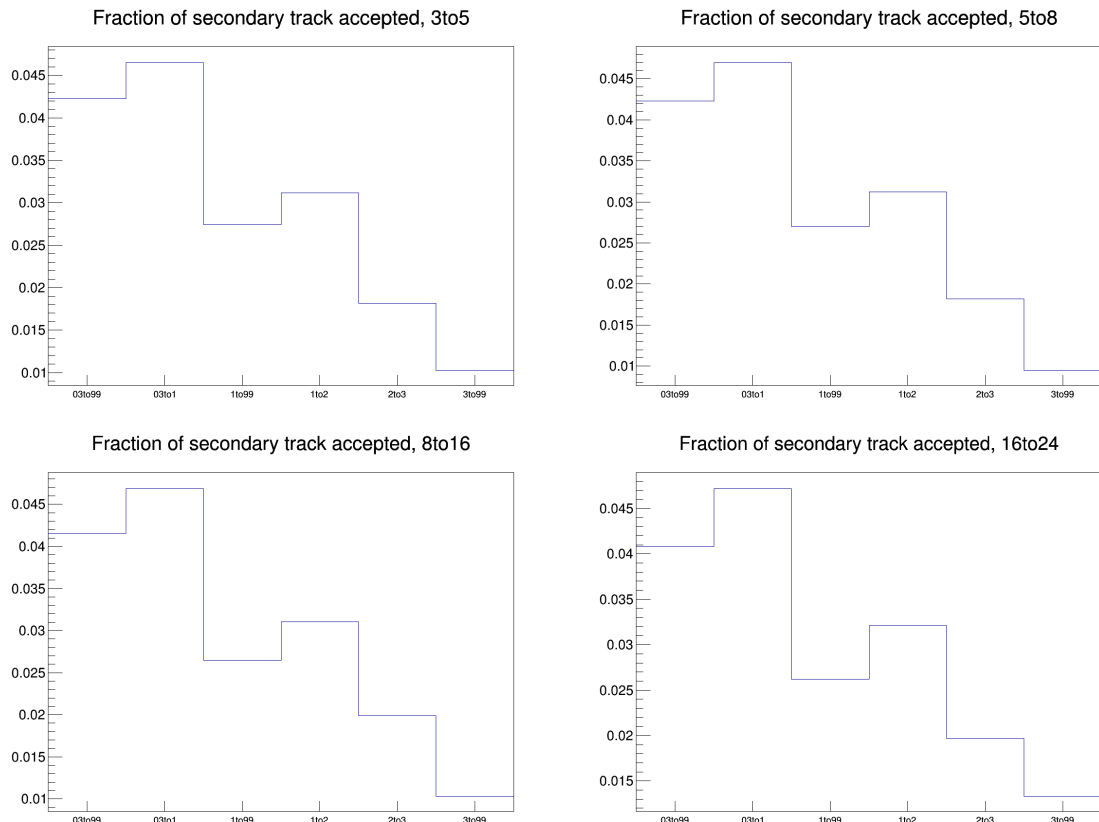


Figure 16: Fraction of secondary tracks over total amount of tracks which pass the DCA selection. The four panel show the fractions for the D-meson p_T ranges: 3-5, 5-8, 8-16, 16-24, respectively. Inside each panel, the associated track p_T ranges are shown on the x -axis.

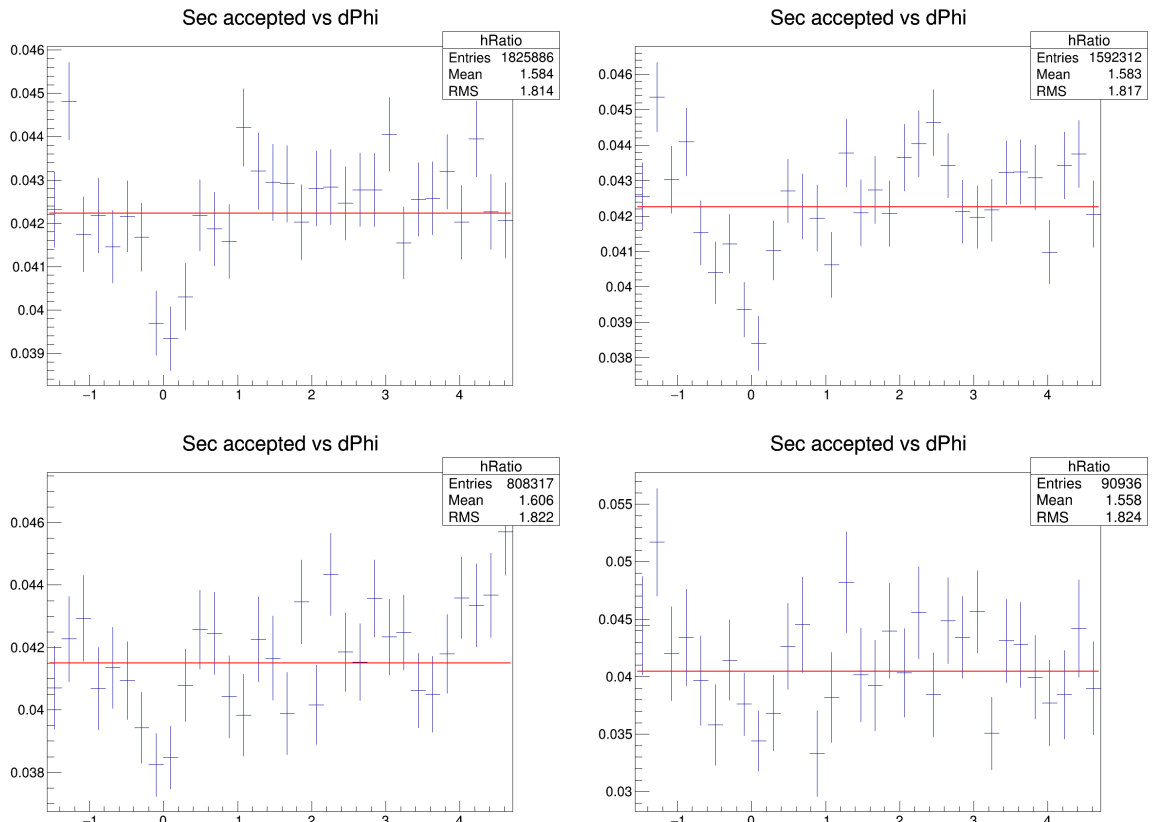


Figure 17: $\Delta\phi$ dependence of the fraction of secondary tracks in the D^0 - h correlation distributions. The four panels show the fractions for the D -meson p_T ranges: 3-5, 5-8, 8-16, 16-24, respectively. The associated track p_T ranges is the integrated one, i.e. $p_T > 0.3$ GeV/c.

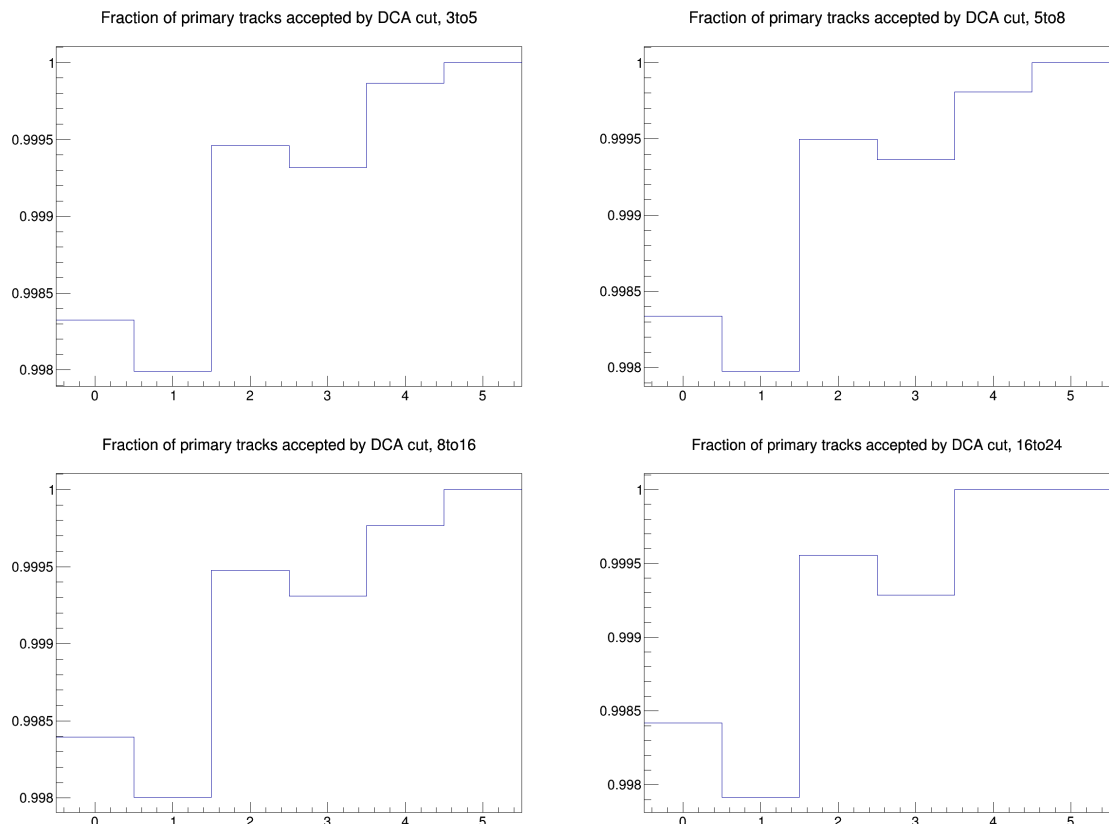


Figure 18: Fraction of primary tracks rejected by the DCA selection. The four panel show the fractions for the D-meson p_T ranges: 3-5, 5-8, 8-16, 16-24, respectively. Inside each panel, the associated track p_T ranges are shown on the x -axis.

425 **3.3.5 Beauty feed-down**

426 The contribution of correlations of D meson from b-hadron decay is subtracted from the data correlation
 427 distributions as:

$$\tilde{C}_{\text{prompt D}}(\Delta\varphi) = \frac{1}{f_{\text{prompt}}} \left(\tilde{C}_{\text{inclusive}}(\Delta\varphi) - (1 - f_{\text{prompt}}) \tilde{C}_{\text{feed-down}}^{\text{MC templ}}(\Delta\varphi) \right). \quad (4)$$

428 In the above equation, $\tilde{C}_{\text{inclusive}}(\Delta\varphi)$ and $\tilde{C}_{\text{prompt D}}(\Delta\varphi)$ are per-trigger azimuthal correlation distributions
 429 before and after feed-down contribution subtraction, f_{prompt} is the fraction of prompt D meson
 430 and $\tilde{C}_{\text{feed-down}}^{\text{MC templ}}$ is a template of the azimuthal correlation distribution for the feed-down component ob-
 431 tained from home-made Monte Carlo simulation at generated level, using PYTHIA6 with Perugia2011
 432 tune. In order to avoid biases related to the different event multiplicity in real and simulated events,
 433 the correlation distribution was shifted to have its minimum coinciding with the baseline of the data
 434 azimuthal-correlation distribution before feed-down subtraction.

435 The value of f_{prompt} (Figure 19), which depends on D-meson species and varies as a function of the p_T ,
 436 is estimated on the basis of FONLL predictions for the production of feed-down D mesons at central
 437 rapidity, in pp collisions at $\sqrt{s} = 5$ TeV, and using the reconstruction efficiency of prompt and feed-
 438 down D mesons, following the so-called N_b approach defined in [1]. Typical values ranges are about
 439 8-10% for the D^0 , about 4-7% for the D^+ and about 5-8% for the D^{*+} . The procedure adopted is the
 440 same as what done in pp: however, in p-Pb, in order to consider a possible non-zero v_2 -like modulation
 441 of the baseline, a range of $0 < v_2 < 0.2$ values for tracks and for secondary D mesons is considered for
 442 the systematic uncertainty evaluation (using an hypothesis of no modulation for both cases for central
 443 values).

444 Examples of the PYTHIA templates used for the feed-down contribution subtraction are shown in Figures
 445 20 (Figure 21 shows the same templates but for prompt D mesons).

446 The feed-down subtraction was performed after rescaling the data correlation distributions for the purity
 447 fraction, and correcting them by the near-side modulation induced by the bias on the B decay topology.

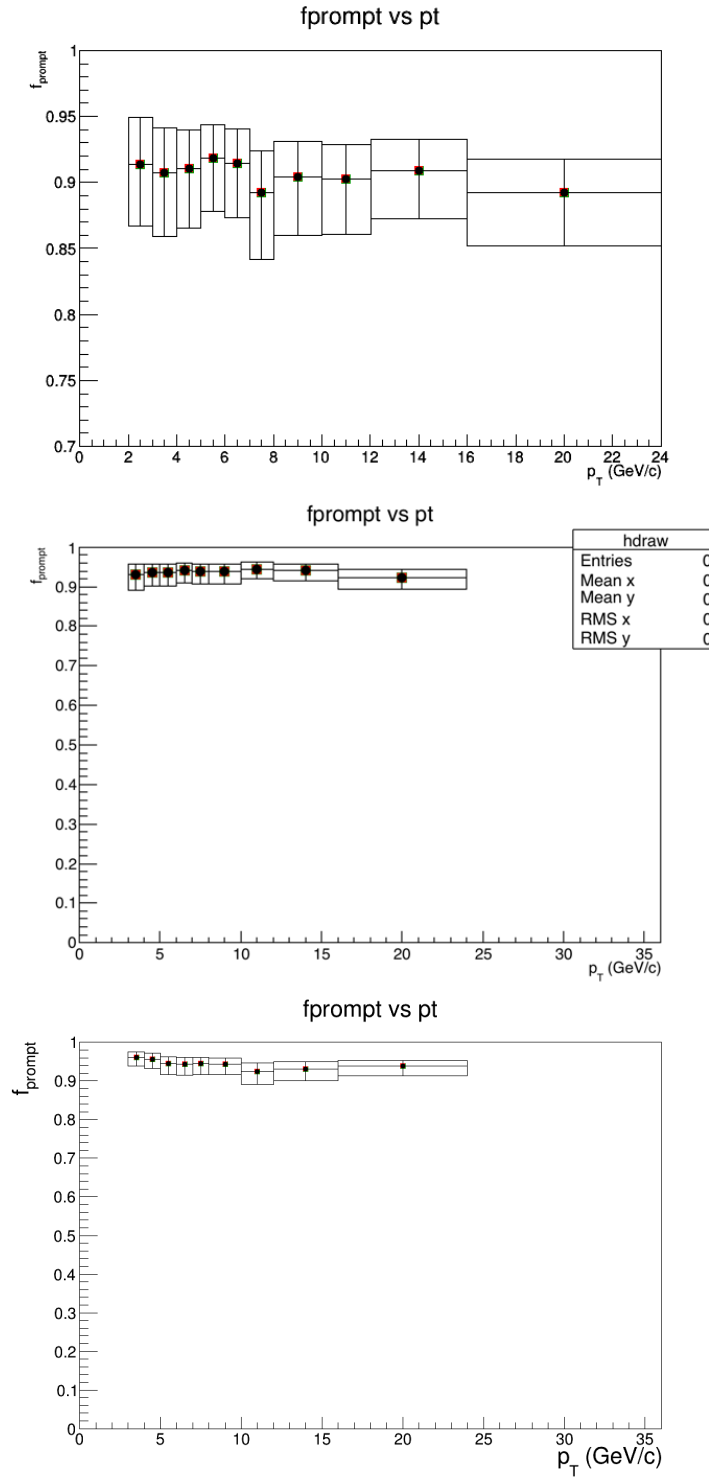


Figure 19: f_{prompt} as a function of the p_T for D^0 (top), D^{*+} (mid) and D^+ (bottom) estimated on the basis of FONLL predictions

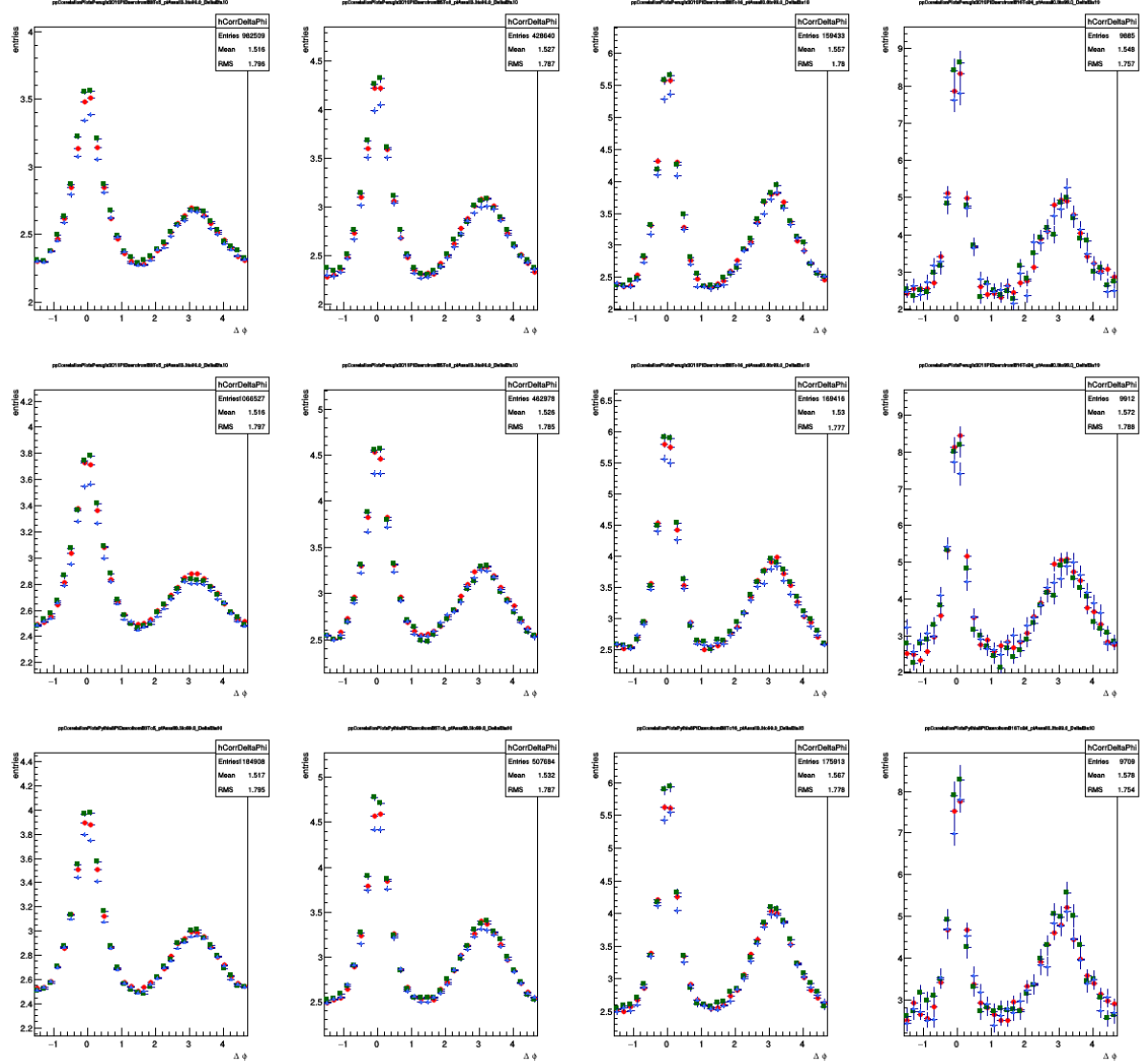


Figure 20: Azimuthal correlation distribution between D meson from b-hadron decay and charged particles obtained from Monte Carlo simulations based on Pythia-Perugia2010 tune (row1), Pythia-Perugia2011 tune (row2), Pythia8 tune (row3) for associated track $p_T > 0.3$ GeV/c and D-meson pT ranges: 3-5, 5-8, 8-16, 16-24 GeV/c. D^0 in blue, D^+ in green, D^{*+} in red.

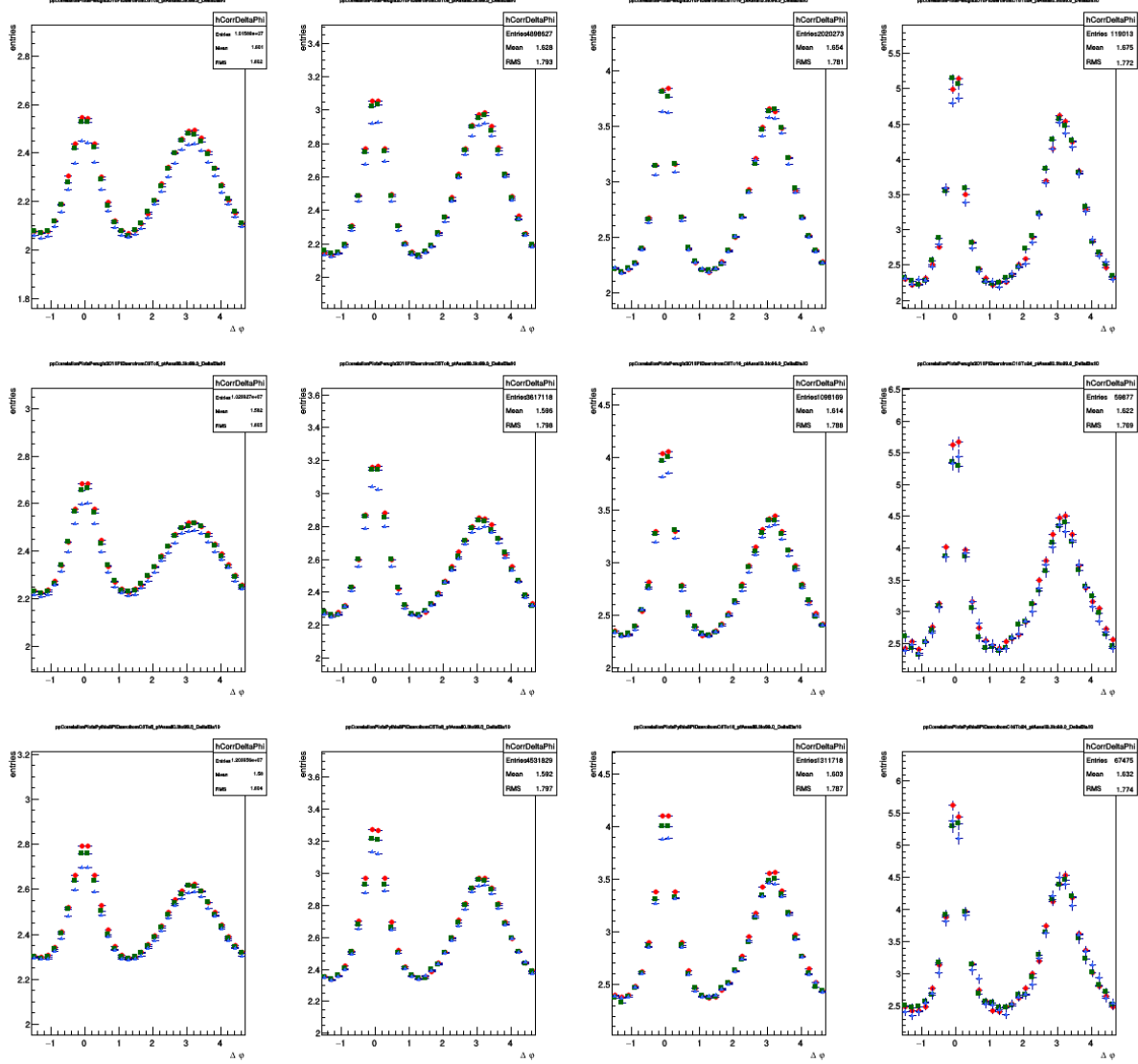


Figure 21: Azimuthal correlation distribution between prompt D meson and charged particles obtained from Monte Carlo simulations based on Pythia-Perugia2010 tune (row1), Pythia-Perugia2011 tune (row2), Pythia8 tune (row3) for associated track $p_T > 0.3$ GeV/c and D-meson pT ranges: 3-5, 5-8, 8-16, 16-24 GeV/c. D⁰ in blue, D⁺ in green, D^{*+} in red.

448 **4 Systematic uncertainties on $\Delta\phi$ correlation distributions**

449 **4.1 Uncertainty on S and B extraction**

450 The systematic uncertainty for the D meson yield extraction was determined separately for the three
 451 mesons. It was obtained by evaluating the value of the signal from the invariant mass spectra with the
 452 following differences with respect to the standard approach:

- 453 – Changing the background fit function, for D^0 and D^+ (tried with polynomials of 1st and 2nd order)
 454 and for D^{*+} (tried with polynomials of 2nd order and a power function);
- 455 – Changing the range in which the signal is extracted from the Gaussian fit;
- 456 – Reducing the range of invariant mass axis in which the signal region is defined (and S and B are
 457 extracted);
- 458 – Rebinning the invariant mass distributions before the fit for D^0 and D^+
- 459 – Extracting S and B via integral of the fit functions or B via bin counting and S via integral of the
 460 Gaussian function.

461 Both the value of the yield and the sidebands correlations normalization factor are affected by changing
 462 the yield extraction approach, while the rest of the procedure to extract the azimuthal correlation distribution
 463 is the same as in the standard analysis. The fully corrected azimuthal correlation plots were
 464 evaluated, for each of these approaches, in the various p_T bins and for each value of associated tracks
 465 p_T threshold. The ratios of the correlation distributions obtained with the standard yield extraction pro-
 466 cedure and by differentiating the approach were evaluated. From the average of these ratios, which
 467 are found to be flat versus $\Delta\phi$, a systematic uncertainty can be extracted, which was taken of 1% for
 468 $3 < p_T(D) < 16$ GeV/c and of 2% in $16 < p_T(D) < 24$ GeV/c (3% for D^0). No dependence versus the
 469 associated track p_T was assumed, since from a physics point of view we don't expect a modification of
 470 the signal and sideband values to have a dependence of this kind. Figures 22, show the ratios obtained
 471 by the above mentioned procedure for exemplary p_T ranges, which anyway span over the full kinematic
 472 ranges analyzed, for D^0 -h correlations. Figures 23 and 24 show the same ratios for D^{*+} -h, D^+ -h as well.

473 **4.2 Uncertainty on background correlation shape**

474 The systematic uncertainty for the subtraction of the background correlations includes the effects due to
 475 a potentially biased description of the background correlation shape, which is evaluated from of the side-
 476 bands correlations. In particular, the background correlation shape could present some hidden invariant
 477 mass dependence. To estimate this uncertainty, the invariant mass range of the sidebands definitions was
 478 varied with respect to the default values. For the D^0 meson, the usual range of the sidebands is 4 to 8σ
 479 from the centre of the peak of the Gaussian fit of the invariant mass spectra, and it was modified, for both
 480 sidebands to:

- 481 – inner half (4 to 6σ from the centre of the peak);
- 482 – outer half (6 to 8σ from the centre of the peak)
- 483 – extended to 4 to 10σ (in case this is possible without exceeding the fitting range of the mass plots)

484 Slightly different variations, but with the same reasoning, were assumed for the D^+ meson.

485 For the D^{*+} meson, the usual range of the sidebands is 5 to 10σ (only on the right side) from the centre
 486 of the peak of the Gaussian fit of the invariant mass spectra, and it was modified to:

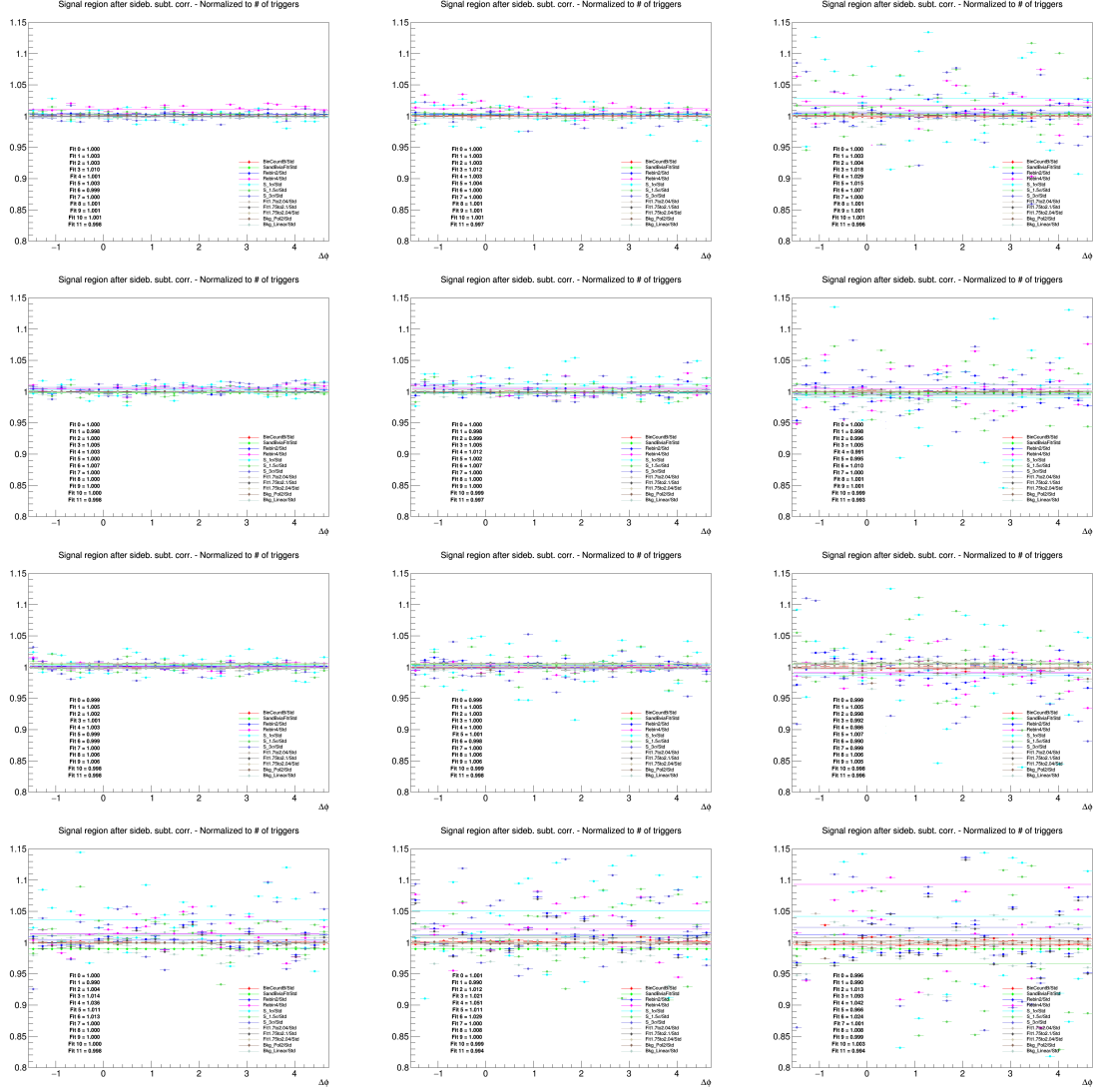


Figure 22: Ratios of D^0 - h correlation plots obtained changing S and B extraction procedure over those obtained with standard yield extraction procedure. Rows: $p_T(D^0)$ 3-5, 5-8, 8-16, 16-24 GeV/c. In each row, the panels show the associated track p_T ranges 0.3-1, 1-2, >3 GeV/c, respectively.

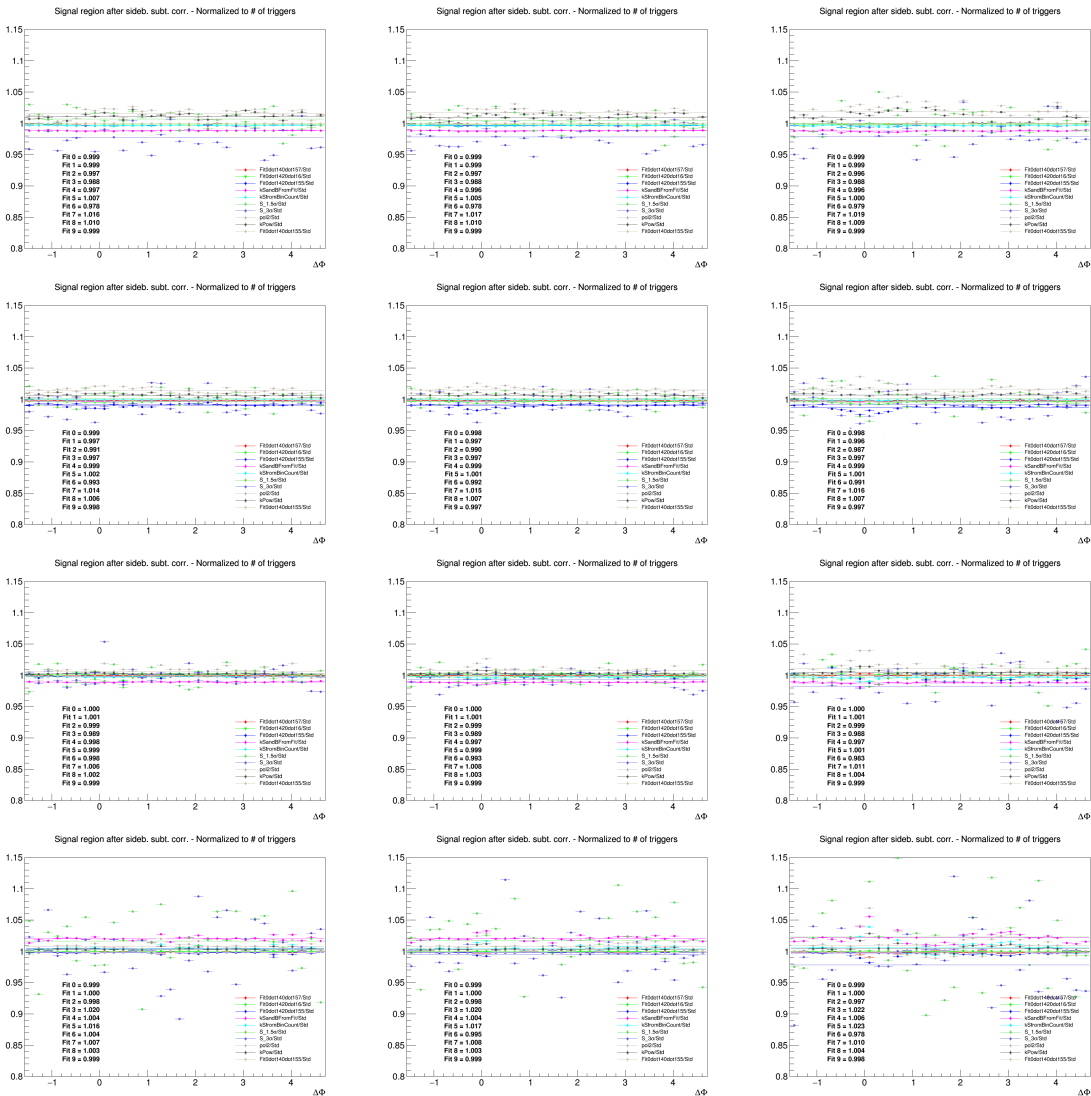


Figure 23: Ratios of D*⁺-h correlation plots obtained changing S and B extraction procedure over those obtained with standard yield extraction procedure. Rows: $p_T(D^*)$ 3-5, 5-8, 8-16, 16-24 GeV/c. In each row, the panels show the associated track p_T ranges >3 GeV/c, 0.3-1 GeV/c and >1 GeV/c, respectively.

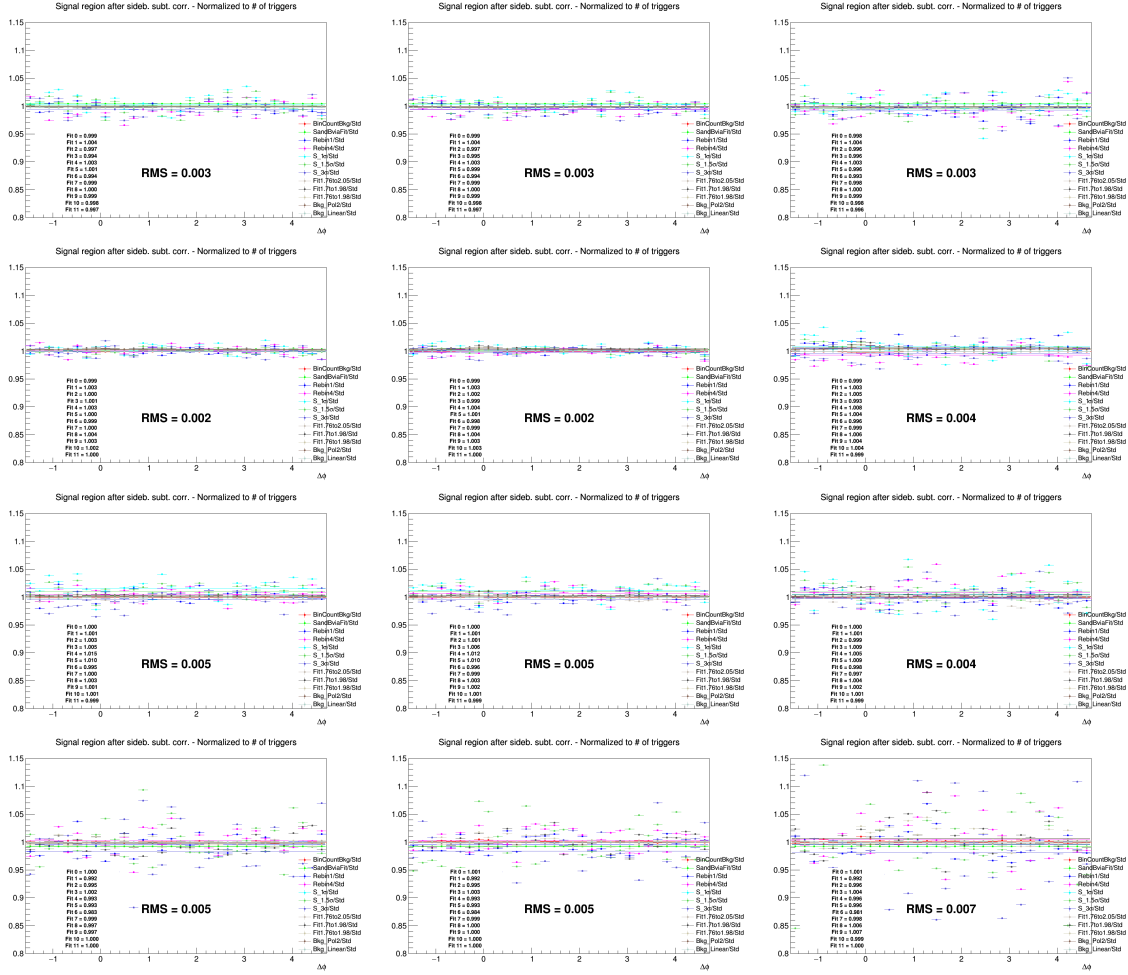


Figure 24: Ratios of D^+ - h correlation plots obtained changing S and B extraction procedure over those obtained with standard yield extraction procedure. Rows: $p_T(D^+)$ 3-5, 5-8, 8-16, 16-24 GeV/c. In each row, the panels show the associated track p_T ranges >3 GeV/c, 0.3-1 GeV/c and >1 GeV/c, respectively.

- 487 – inner half (5 to 8 σ from the centre of the peak);
- 488 – outer half (8 to 13 σ from the centre of the peak);
- 489 – extended to 5 to 13 σ from the centre of the peak;
- 490 – extended to 6 to 16 σ from the centre of the peak.

491 The rest of the procedure for the azimuthal correlations distribution was unchanged, and the ratios of
 492 the fully corrected azimuthal correlation plots obtained with the standard sidebands range and the corre-
 493 lation plots extracted with different sidebands definitions, were evaluated for each D-meson p_T bin and
 494 associated tracks p_T threshold. Results of this check are shown in Figures 25, 26 and 27 for D^0 , D^{*+} ,
 495 D^+ respectively, for exemplary p_T ranges, spanning over the full kinematic regions analysis. From the
 496 values of the ratios extracted from the checks, which do not show any azimuthal dependence a systematic
 497 uncertainty for the background subtraction can be evaluated. Also no dependence versus the associated
 498 track p_T was assumed also in this case. The uncertainty was hence taken of 1% for $3 < p_T(D) < 16$
 499 GeV/c and 3% for $16 < p_T(D) < 24$ GeV/c for the three D mesons.

500 4.3 Uncertainty on D-meson cut stability

501 To study the systematics due to the topological selections on the D meson, the cut variation approach was
 502 used. For each D-meson, alternate sets of released and tightened selection cuts were applied to extract
 503 the correlation distribution, varying in particular the cosine of the pointing angle, the maximum DCA
 504 among the daughter tracks and the product of the daughter track impact parameters. For each set of cuts
 505 a new efficiency map was computed. In Figures 28, 29, 30 (for D^0 , D^{*+} and D^+ , respectively) the ratio
 506 of the different 1D efficiencies with the alternate cuts with respect to the default cut selection is chosen,
 507 to highlight how the different selections effectively varied the efficiency values, especially at low p_T ,
 508 where cuts are more effective.

509 Figure 31, 32, 33 show the ratio of the correlation distributions with alternate cut sets over those with
 510 the standard approach, for exemplary p_T ranges covering the full kinematic region of interest for the
 511 analyses. The ratios are reasonably flat in $\Delta\phi$, hence a flat systematic was evaluated as systematic
 512 uncertainty from D-meson the cut variations. For the D^0 , the uncertainty was assumed of 2% for all
 513 the p_T ranges of trigger and tracks analyzed. For the D^{*+} , the uncertainty was assumed of 1.5% for
 514 $3 < p_T(D) < 8$ GeV/c and of 1% for $8 < p_T(D) < 24$ GeV/c. For the D^+ , the uncertainty was assumed
 515 of 1% for $3 < p_T(D) < 16$ GeV/c and of 3% for $16 < p_T(D) < 24$ GeV/c.

516 4.4 Uncertainty on tracking efficiency evaluation

517 The systematic uncertainty for the tracking efficiency includes the effects related to the set of filtering cuts
 518 defined for the associated tracks selection (mainly requests on the quality of reconstructed tracks for the
 519 TPC and ITS detectors). This uncertainty was determined by repeating the full analysis using different
 520 selections for the cuts on the associated tracks with respect to the usual selection (TPC only tracks with at
 521 least 2 points in the ITS). The alternative selections were: pure 'TPConly' selection, meaning TPC tracks
 522 with no requests on the number of hits in the ITS, and 'TPC+ITS' selection, which requires filterbit 4
 523 with, in addition, at least 3 points in the ITS, ITS refit and a hit in at least an SPD layer. The ratios
 524 of the azimuthal correlation distributions with different tracks selection over distributions with standard
 525 selection were evaluated, and are shown in Figures 34 and 35 for D^0 -h correlations. Their values were
 526 used to determine a systematic uncertainty, which as the previous ones could be assigned flat in $\Delta\phi$, and
 527 which was estimated of 3% in all the ranges of p_T analyzed.

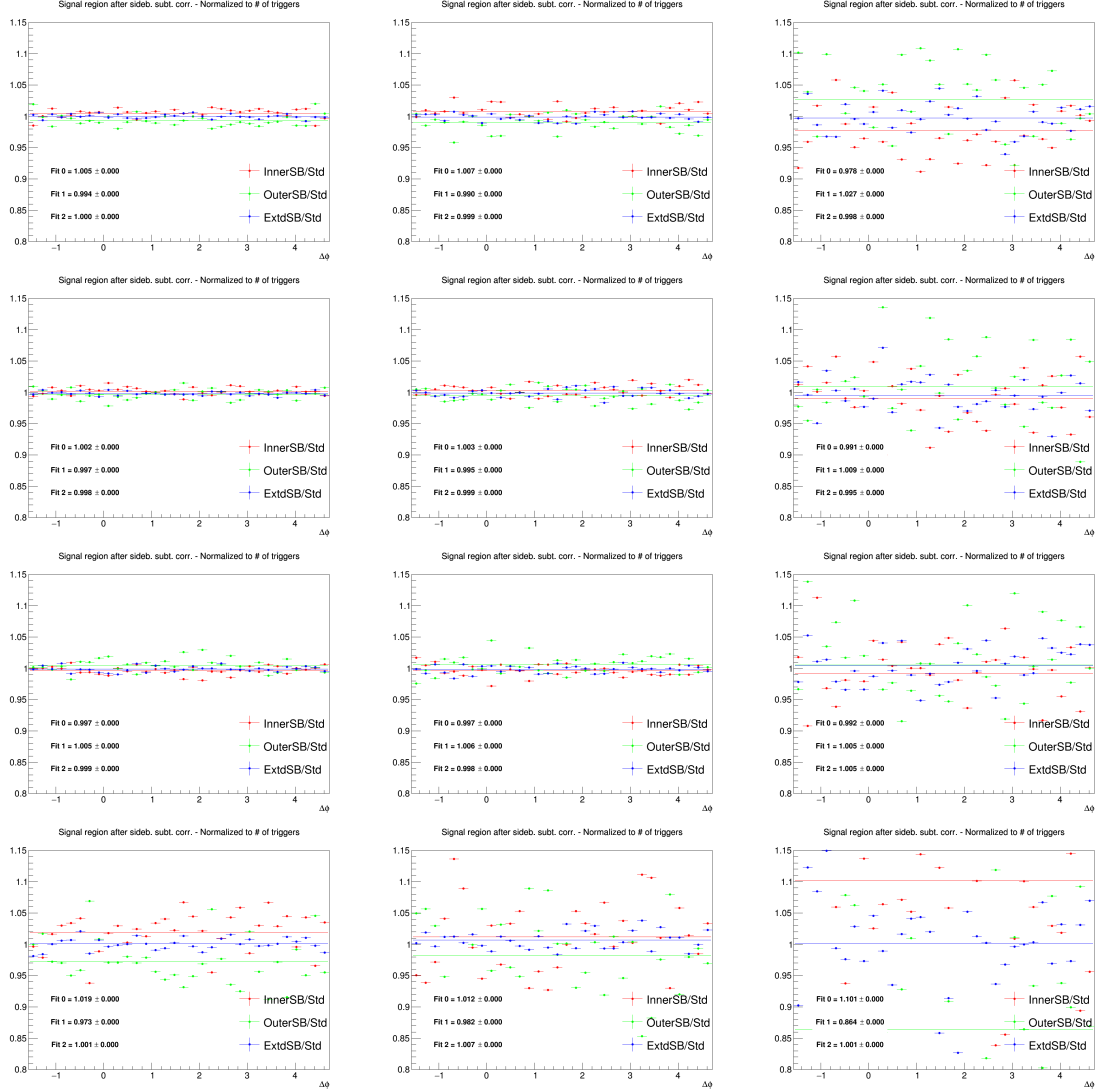


Figure 25: Ratios of D^0 - h correlation plots obtained changing the sideband ranges over those obtained with standard ranges. Rows: $p_T(D^0)$ 3-5, 5-8, 8-16, 16-24 GeV/c. In each row, the panels show the associated track p_T ranges 0.3-1, 1-2, >3 GeV/c, respectively.

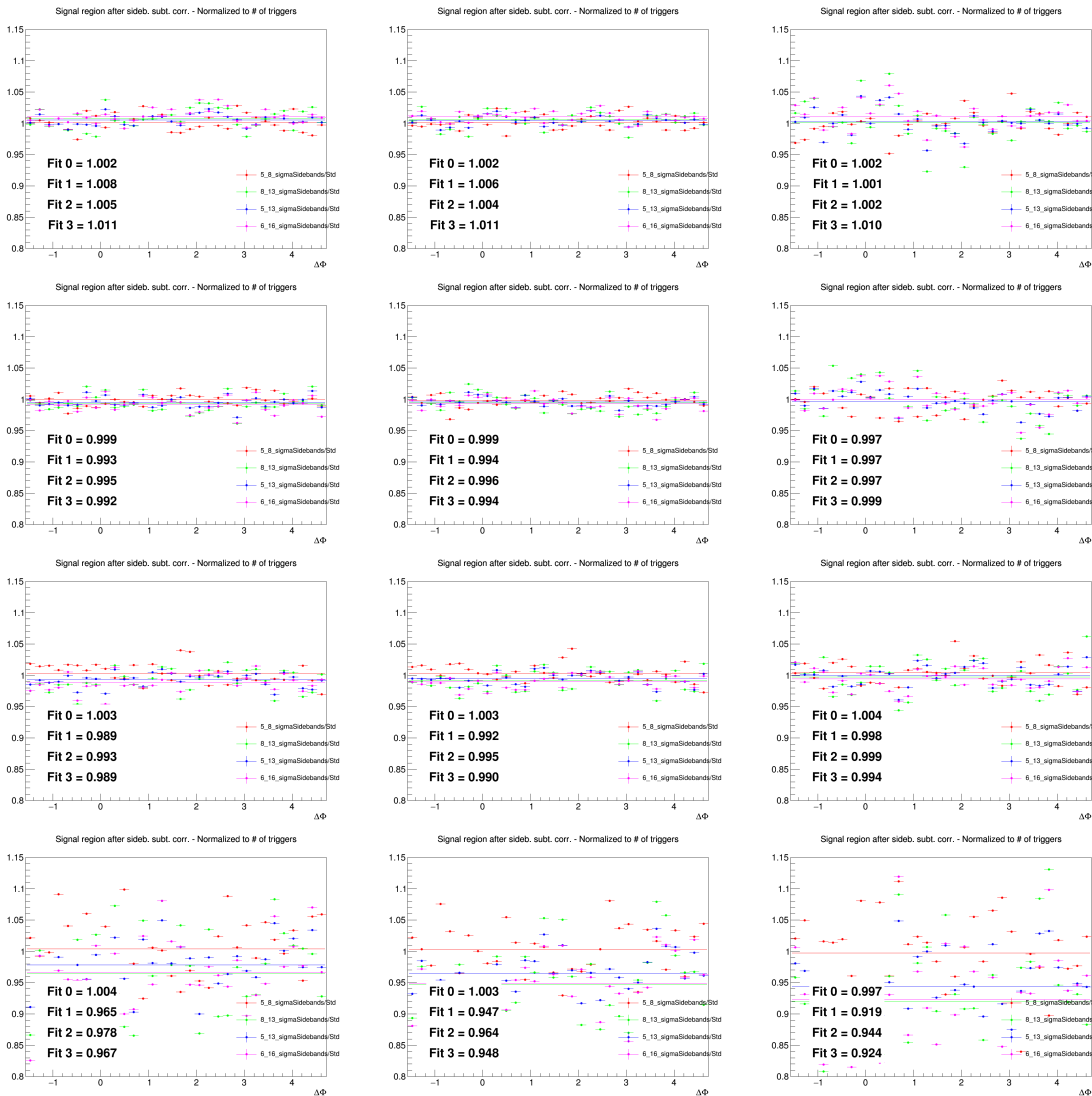


Figure 26: Ratios of $D^*+ - h$ correlation plots obtained changing the sideband ranges over those obtained with standard ranges. Rows: $p_T(D^*)$ 3-5, 5-8, 8-16, 16-24 GeV/c. In each row, the panels show the associated track p_T ranges 0.3-1, >3 GeV/c and >1 GeV/c, respectively.

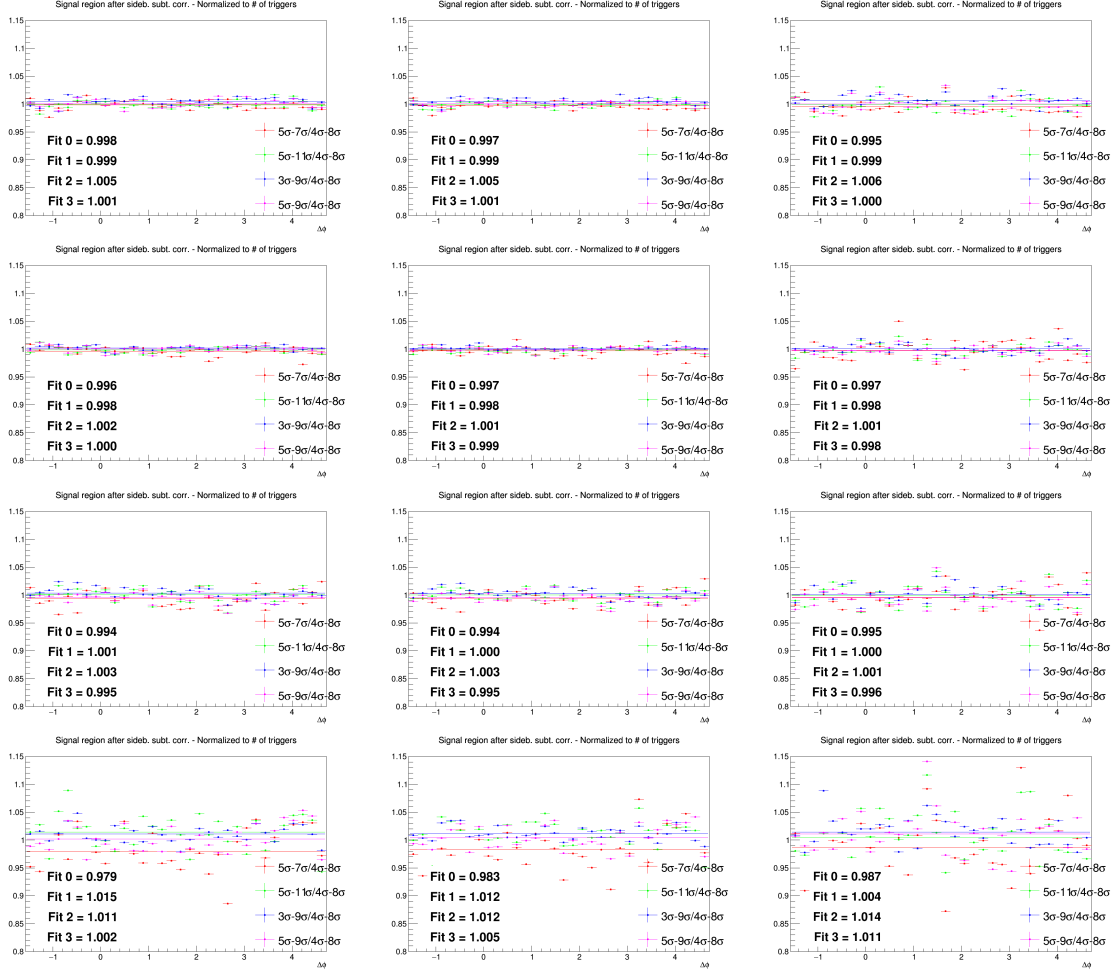


Figure 27: Ratios of D⁺ - h correlation plots obtained changing the sideband ranges over those obtained with standard ranges. Rows: p_T(D⁺) 3-5, 5-8, 8-16, 16-24 GeV/c. In each row, the panels show the associated track p_T ranges 0.3-1, >3 GeV/c and >1 GeV/c, respectively.

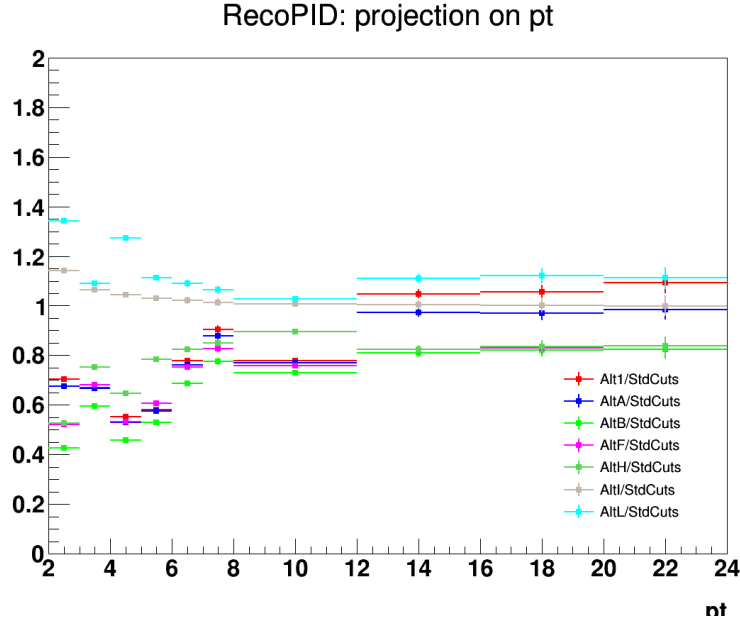


Figure 28: Ratio of D^0 efficiencies with alternate variations w.r.t. the standard cut used for the analysis.

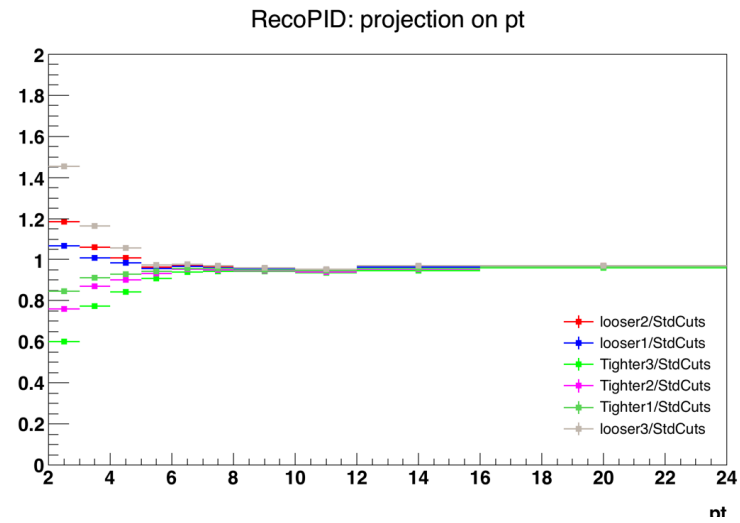


Figure 29: Ratio of D^{*+} efficiencies with alternate variations w.r.t. the standard cut used for the analysis.

528 4.5 Uncertainty on secondary particle contamination

529 Secondary particles, i.e. particles coming from strange hadrons decays or particles produced in inter-
 530 actions with the material, are expected to be tagged and removed by means of a distance of closest
 531 approach (DCA) from primary vertex cut. The uncertainty arising from the residual contamination of
 532 secondary tracks can be estimated from a Monte Carlo study, at reconstructed level. The number of
 533 primary/secondary tracks which are accepted/rejected from the DCA cut was determined for different
 534 values of the DCA selection, and the azimuthal distribution of the correlations for the various cases were
 535 evaluated. The variations were done in the xy direction, where the DCA resolution is better, and the
 536 following cases were tried (in addition to the default 1 cm cut): 0.1 cm, 0.25 cm, 0.5 cm, filtering DCA
 537 cut (i.e. 2.4 cm).

538 Figure 36 shows the amount of secondary tracks which are accepted by the DCA cut, over the total
 539 number of tracks (primary and secondary) accepted by the selection, for the various DCA selections that
 540 were tried. This is shown for the exemplary case of $5 < p_T < 8$ GeV/c (there's no $p_T(D)$ dependence)

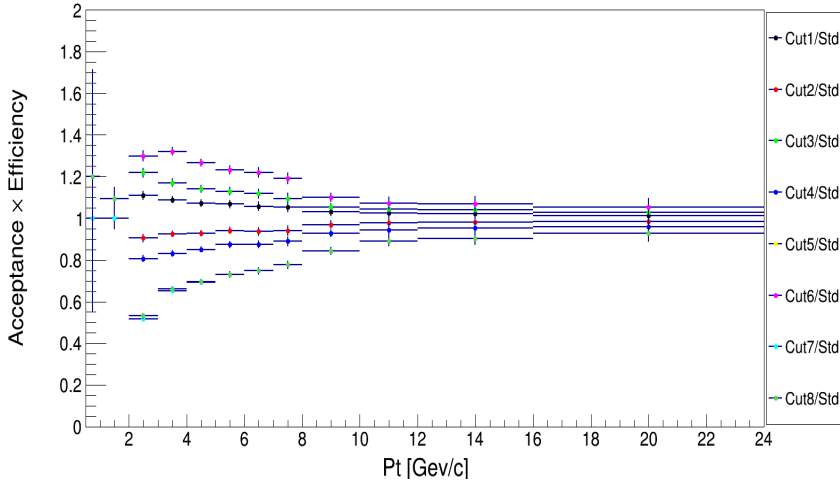


Figure 30: Ratio of D^+ efficiencies with alternate variations w.r.t. the standard cut used for the analysis.

and as a function of the associated track p_T ranges. This quantity is, hance, the residual contamination of secondary tracks in our reconstructed track sample. From these values, the corresponding primary track purities (1-contamination) were extracted, in each of the momentum ranges. It was also verified that, for all the cut selections, the $\Delta\phi$ distributions of the residual contaminations were flat within 1%.

As a second step of the procedure to verity the DCA cut stability, the D^0 -h data analysis was performed with all the different DCA selection (each time with the proper tracking efficiency map). After having extracted the correlation distributions, these were rescaled for the corresponding purities and compared with the purity-corrected correlation distributions obtained with the standard DCA selection. The ratios of the alternate selections over the standard selection, after the purity correction of both, are shown in Figures 37 and 38.

The ratios show a flat trend along the $\Delta\phi$ axis and, in general, a discrepancy from the value of 1 of no more than 3% (the worst case being the 0.3-1 GeV/c range for the associated track). Hence, a flat and symmetric 3% systematical uncertainty on the evaluation of the secondary contamination was assigned on the base of this check in 0.3-1 GeV/c, reduced to 2.5% in > 0.3 GeV/c and to 1.5% for the other ranges. This amount also covers possible biases in the estimation of the purity (the $\Delta\phi$ distribution of the residual contamination is always contained inside 1%, as previously said).

4.6 Uncertainty on feed-down subtraction

As described in the 3.3.5 section, the feed-down subtraction from the data distributions is performed by means of simulation templates of $B \rightarrow D$ -h correlation distributions from PYTHIA6 generator, with Perugia2011 tune, and considering the central value of f_{prompt} to extract the feed-down D-meson contribution. In order to evaluate a systematic uncertainty on this procedure, the feed-down subtraction procedure was repeated considering, together with PYTHIA6+Perugia2011 templates, also PYTHIA6+Perugia2010 and PYTHIA8 simulations. In each case, not only the central value of the measured f_{prompt} was considered to rescale the distributions, but also the maximum and minimum values of its total uncertainty.

Then, the envelope of nine the different cases obtained by varying the templates and the f_{prompt} assumption was considered, and a value of the systematics defined as the envelope spread divided by $\sqrt{3}$ was taken as systematic uncertainty. This uncertainty was assumed uncorrelated among the different $\Delta\phi$ points.

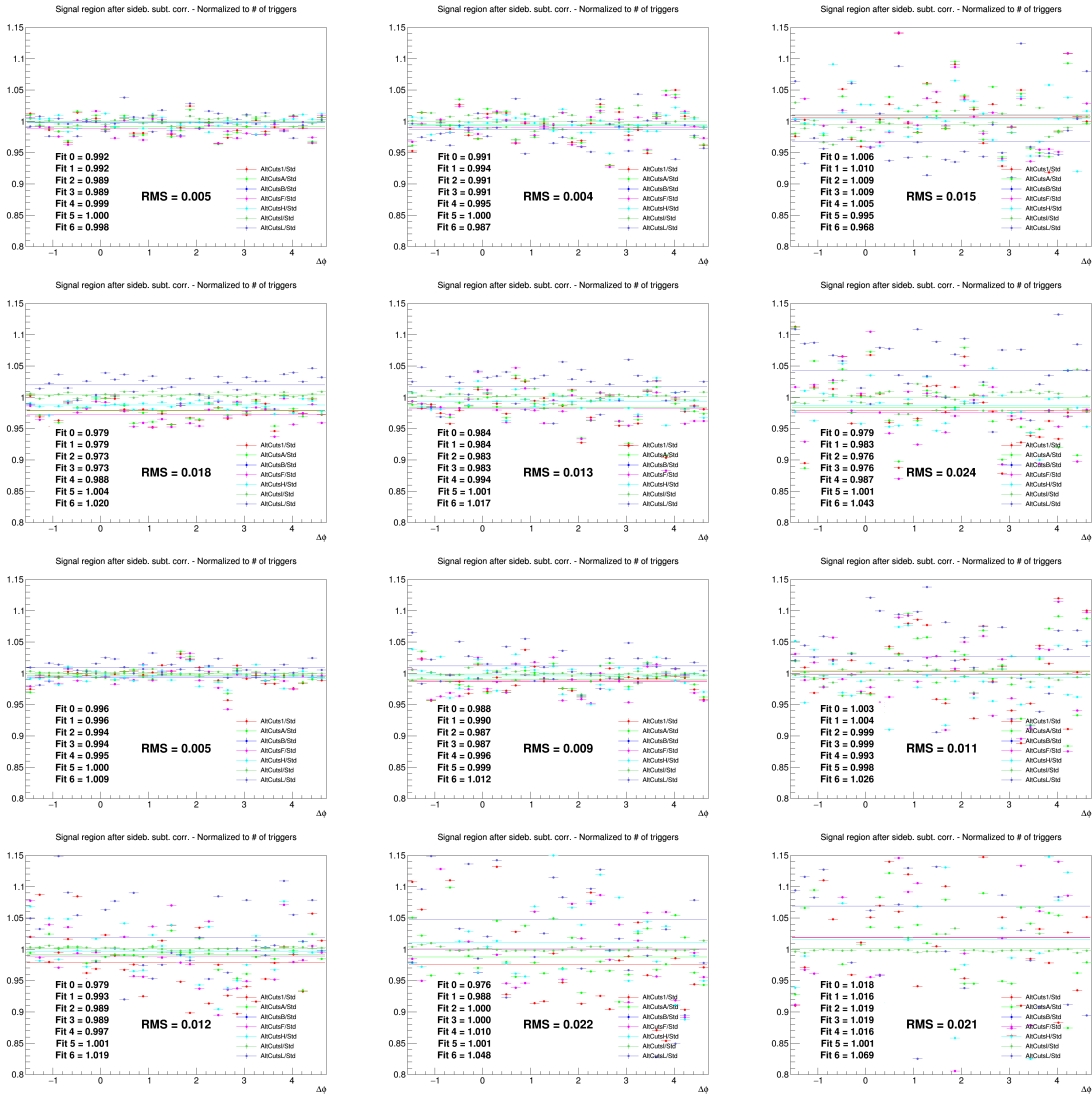


Figure 31: Ratios of D^0 -h correlation plots obtained with alternate D-meson cut sets over those obtained with standard selection. Rows: $p_T(D^0)$ 3-5, 5-8, 8-16, 16-24 GeV/c. In each row, the panels show the associated track p_T ranges 0.3-1, 1-2, 2-3 GeV/c, respectively.

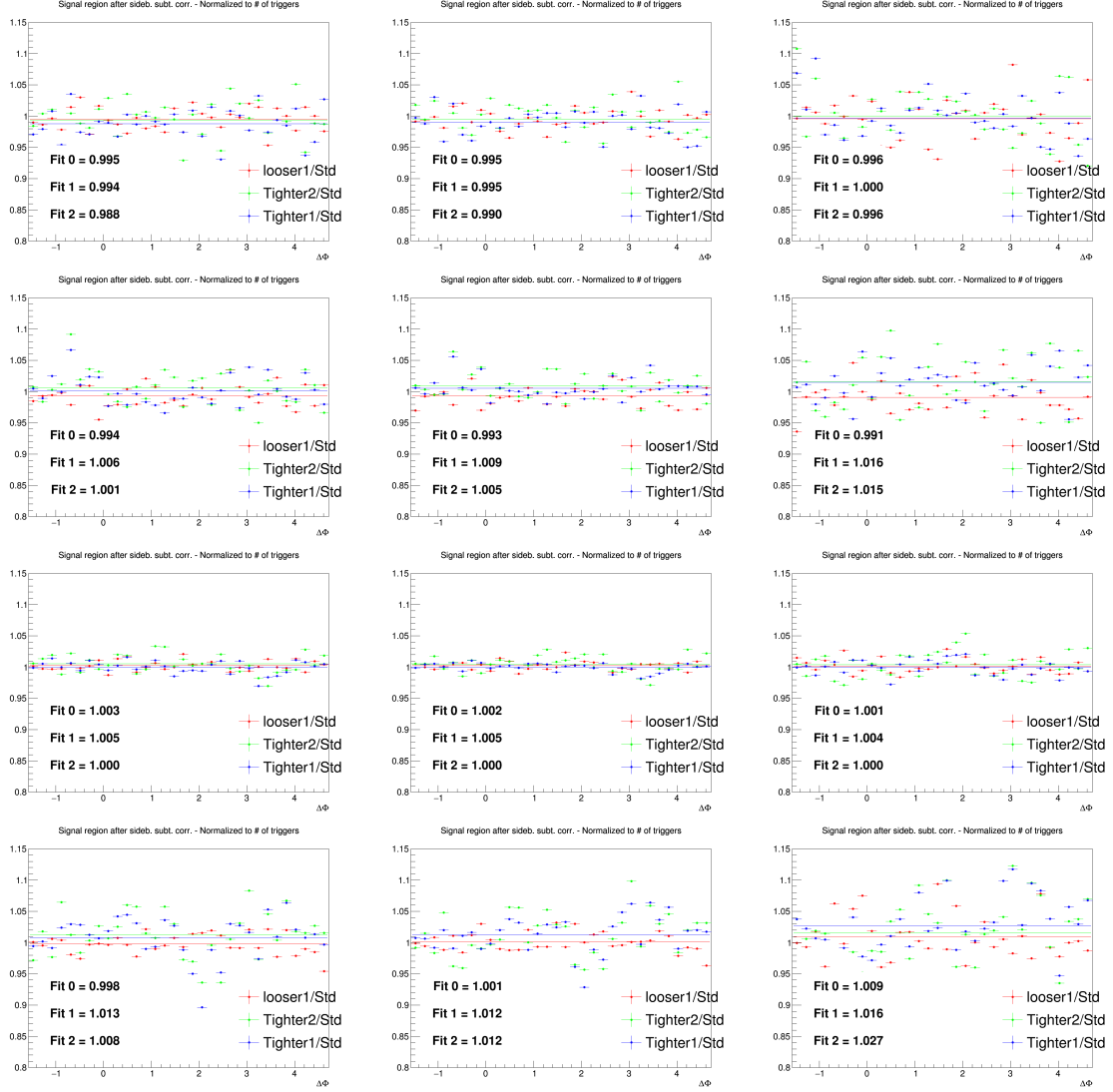


Figure 32: Ratios of D^{*+} - h correlation plots obtained with alternate D-meson cut sets over those obtained with standard selection. Rows: $p_T(D^{*+})$ 3-5, 5-8, 8-16, 16-24 GeV/c. In each row, the panels show the associated track p_T ranges 0.3-1, >0.3 GeV/c, >1 GeV/c, respectively.

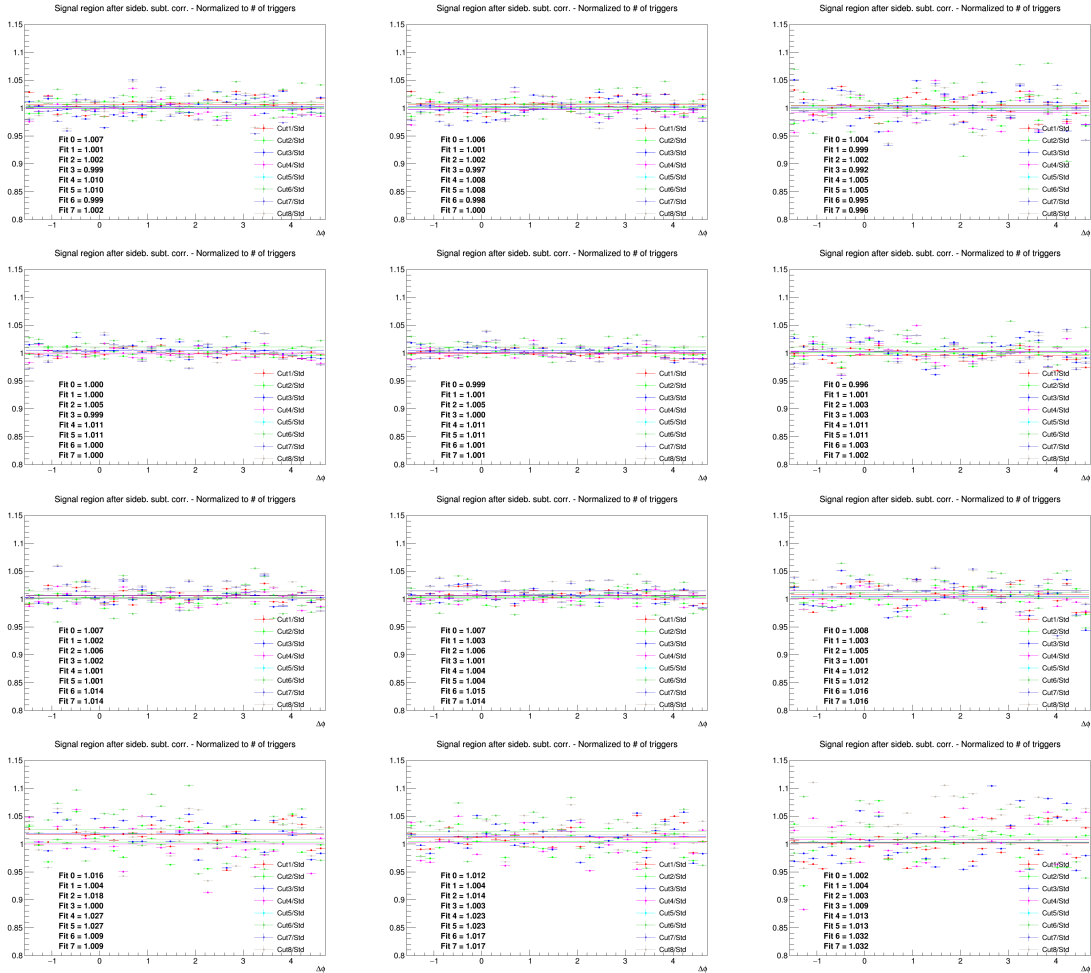


Figure 33: Ratios of D⁺-h correlation plots obtained with alternate D-meson cut sets over those obtained with standard selection. Rows: $p_T(D^+)$ 3-5, 5-8, 8-16, 16-24 GeV/c. In each row, the panels show the associated track p_T ranges 0.3-1, >0.3 GeV/c, >1 GeV/c, respectively.

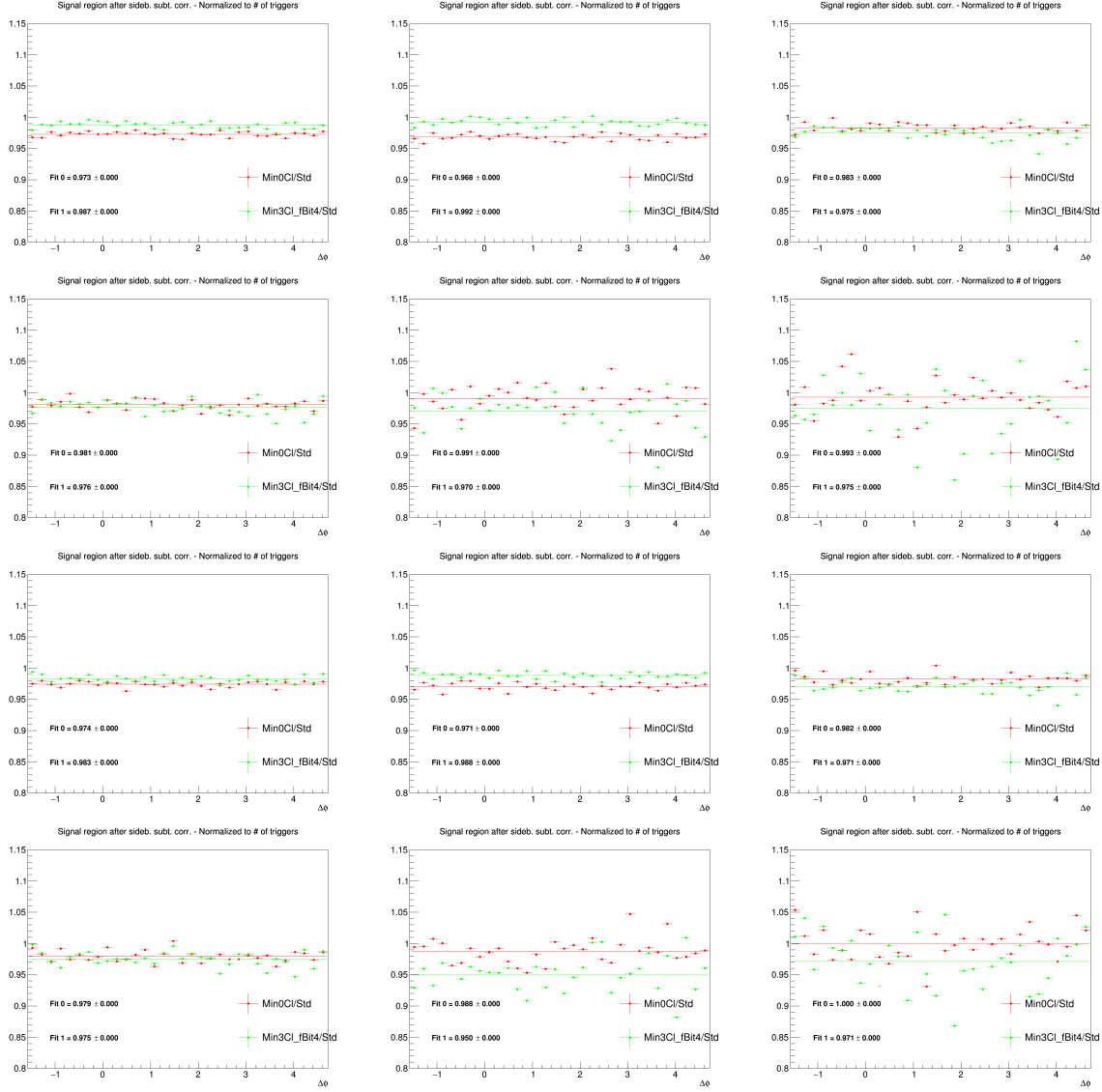


Figure 34: Ratios of correlation plots obtained with different associated tracks filtering selections. First 6 plots: $p_T(D)$ 3-5 GeV/c, next 6 plots: $p_T(D)$ 5-8 GeV/c. Each bunch of 6 plots has $p_T(\text{assoc})$ of >0.3 , $0.3-1$, >1 , $1-2$, $2-3$, <3 GeV/c, respectively.

569 4.7 Uncertainty on correction for the bias on B to D decay topologies

570 The evaluation of this systematic uncertainty was already explained in Section 3.3.3. For each of the
 571 five data points close to the center of the near-side peak, which are affected by the bias, a bilateral and
 572 symmetric uncertainty of amplitude $|C(\Delta\phi)_{\text{corr}} - C(\Delta\phi)_{\text{raw}}|/\sqrt{12}$ was assigned.

573 This because the uncorrected data points are expected to be the extreme (with the current D-meson
 574 selection, the bias is always upwards at the centre of the peak, and always upwards on its sides). We
 575 then assume that, if the correction is properly evaluated, the corrected data points are at the centre of the
 576 possible spread of the true unbiased results. In this case, the span of the possible true results (in case
 577 of underestimation/overestimation of the bias) goes from the uncorrected data points to its symmetric
 578 value, with respect to the corrected data point, on the other direction. If this distribution is uniform,
 579 and constrained by these two values, the 1σ confidence region for the position of the is in a bilateral
 580 $|C(\Delta\phi)_{\text{corr}} - C(\Delta\phi)_{\text{raw}}|/\sqrt{12}$ window, centered on the $|C(\Delta\phi)_{\text{corr}}$ points.



Figure 35: Ratios of correlation plots obtained with different associated tracks filtering selections. First 6 plots: $p_T(D)$ 8-16 GeV/c, next 6 plots: $p_T(D)$ 16-24 GeV/c. Each bunch of 6 plots has $p_T(\text{assoc})$ of >0.3 , $0.3-1$, >1 , $1-2$, $>2-3$, <3 GeV/c, respectively.

581 This source of uncertainty was assumed uncorrelated among the $\Delta\phi$ points.

582 4.8 Summary table

583 A summary of the $\Delta\phi$ -correlated uncertainties affecting the correlation distributions is show in Figure
584 39. They are the S and B extraction uncertainty, the background shape uncertainty, the cut variation
585 uncertainty, the tracking efficiency uncertainty and the secondary particle contamination uncertainty.

586 The overall amount of $\Delta\phi$ -correlated uncertainties is about 5-6% (depending on the p_T bin) for the single
587 D-meson cases; when evaluating the averages of the distributions (see next section), this uncertainty
588 shrinks to 4-5%. This uncertainty is a global scale factor of the distributions, and is quoted as a label in
589 the plots.

590 The systematics uncertainties from feed-down subtraction and B \rightarrow D decay topology bias, instead are
591 $\Delta\phi$ dependent, and are hence reported as uncorrelated boxes in the plots. They do not amount to more
592 than 4%, in every bin of all the kinematic ranges studied.

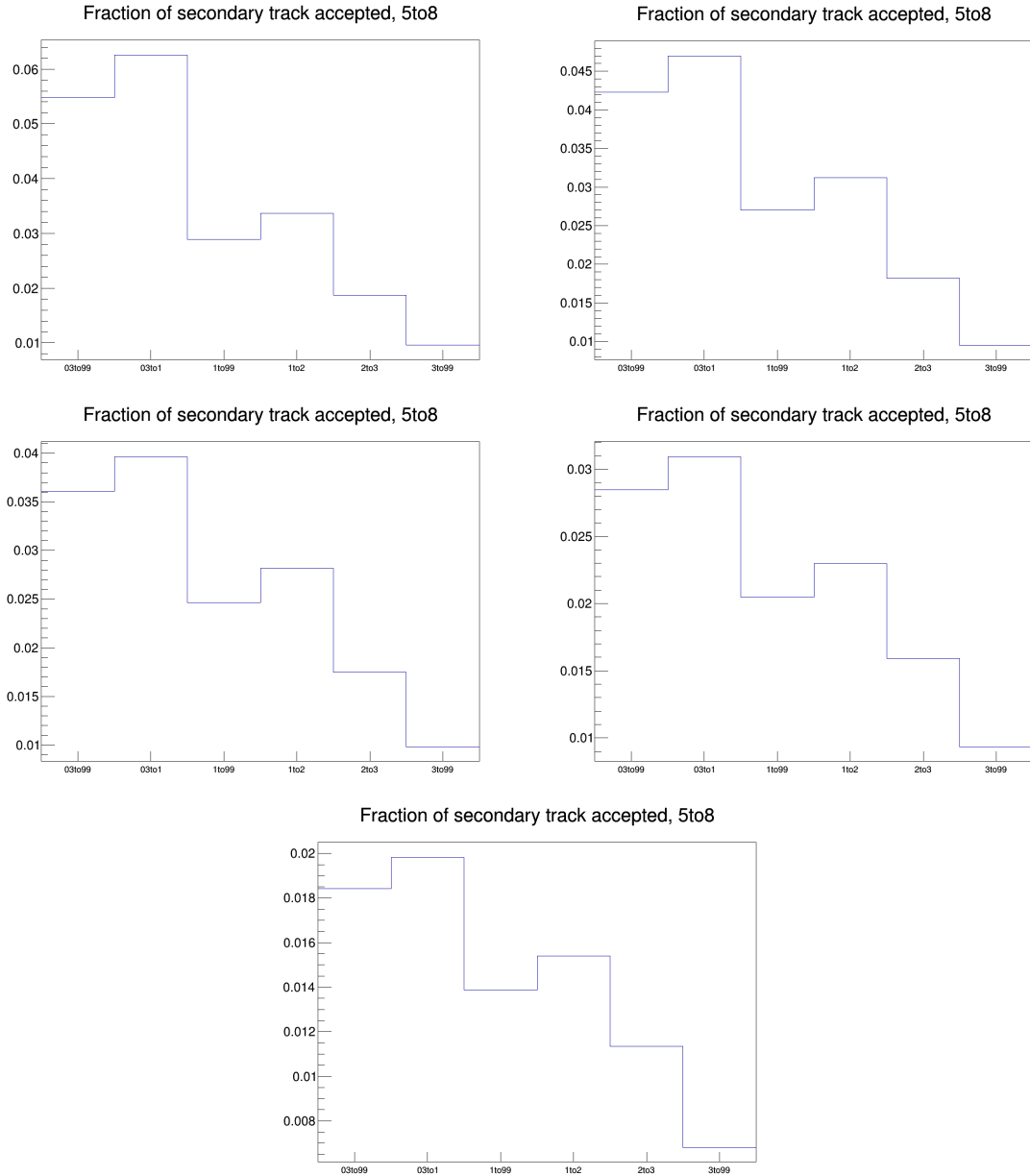


Figure 36: Secondary track contamination as a function of the associated track p_T , for the various DCA selections tried. The plots are ordered from the loosest to the tightest selection, i.e.: $DCA(xy) < 2.4 \text{ cm}$, $< 1 \text{ cm}$, $< 0.5 \text{ cm}$, $< 0.25 \text{ cm}$, $< 0.1 \text{ cm}$.

5 Results

5.1 Comparing the three D meson correlation distributions

To check the compatibility of the three D meson analyses, Figure 40 shows the corrected azimuthal correlation distributions (except for the feed-down subtraction and the secondary contamination removal) for D^0 -h, D^{*+} -h and D^+ -h, in each column, on the data sample used in the analysis. Results are shown for $3 < D p_T < 5 \text{ GeV}/c$, $5 < D p_T < 8 \text{ GeV}/c$, $8 < D p_T < 16 \text{ GeV}/c$ and $16 < D p_T < 24 \text{ GeV}/c$ with associated tracks $p_T > 0.3$, $p_T > 1$, $0.3 < p_T < 1 \text{ GeV}/c$, $1 < p_T < 2 \text{ GeV}/c$, $2 < p_T < 3 \text{ GeV}/c$ and $p_T > 3 \text{ GeV}/c$.

Figures 41, 42, 43, 44 show the superimposed correlation distributions from the single-meson analyses

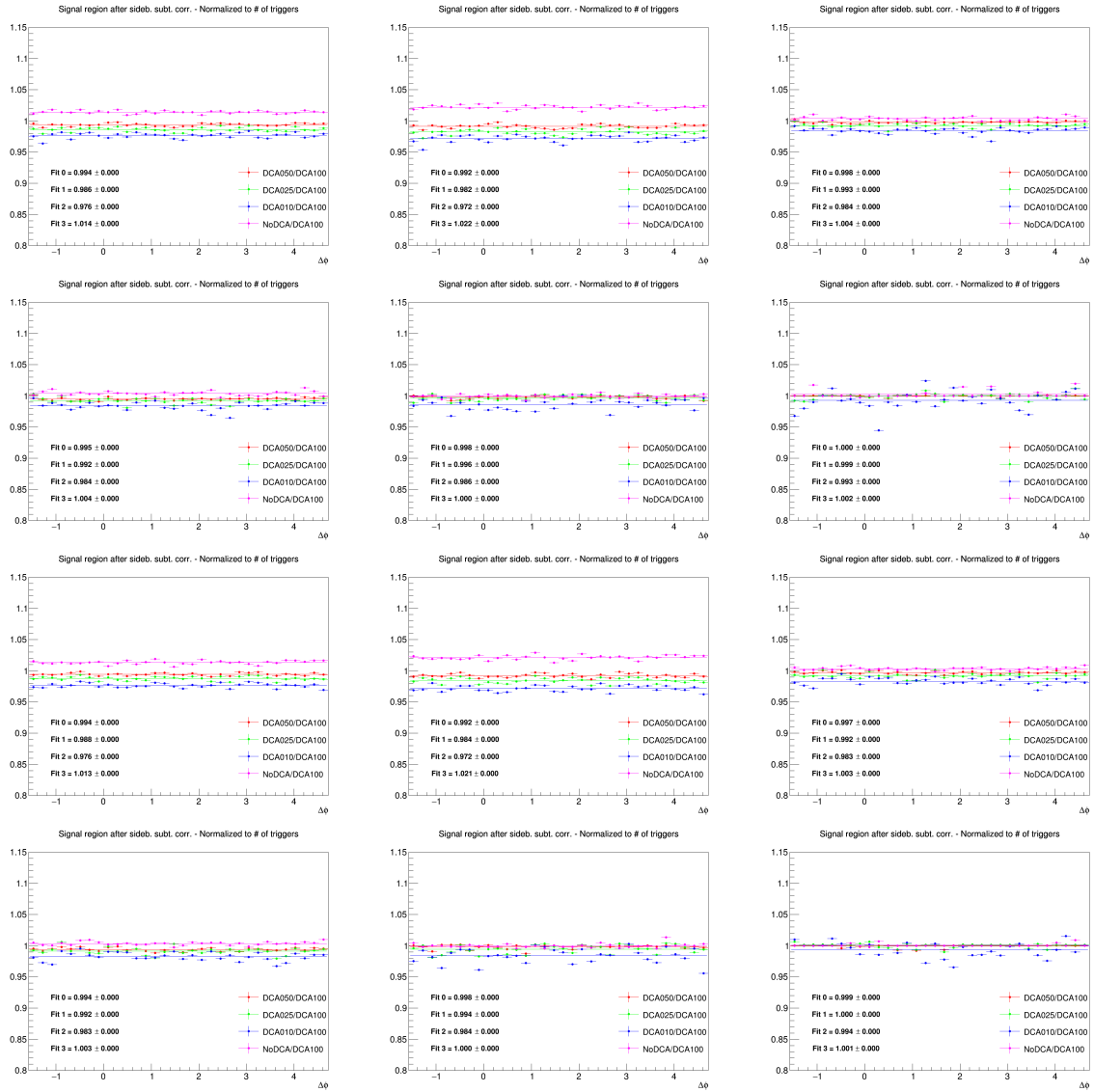


Figure 37: Ratios of correlation plots obtained with different associated DCA selections, after purity correction. First 6 plots: $p_T(D)$ 3-5 GeV/c, next 6 plots: $p_T(D)$ 5-8 GeV/c. Each bunch of 6 plots has $p_T(\text{assoc})$ of >0.3 , $0.3-1$, >1 , $1-2$, $2-3$, <3 GeV/c, respectively.

602 (same plots as previous figure) for better visualize the agreement among the different D-meson species
 603 results.

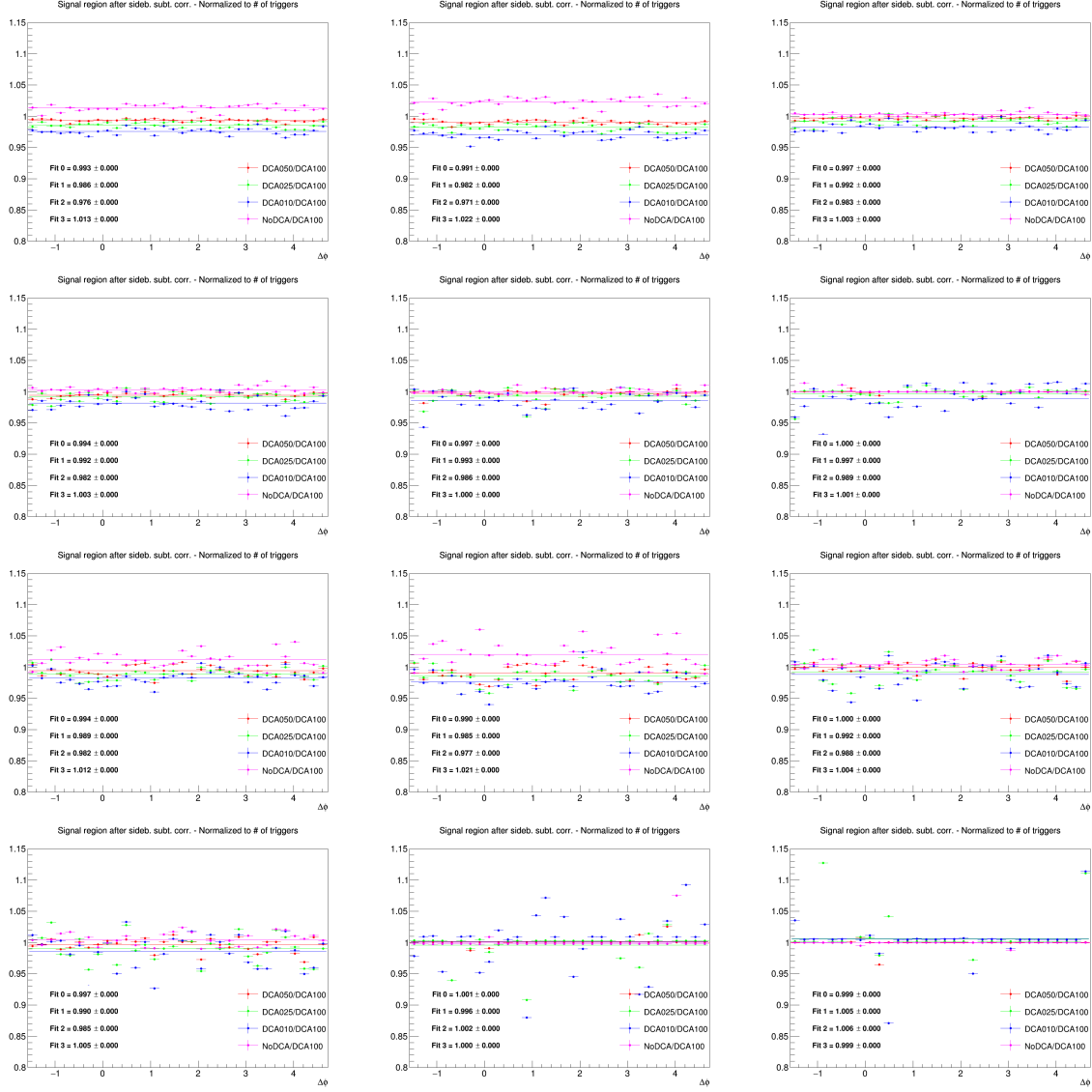
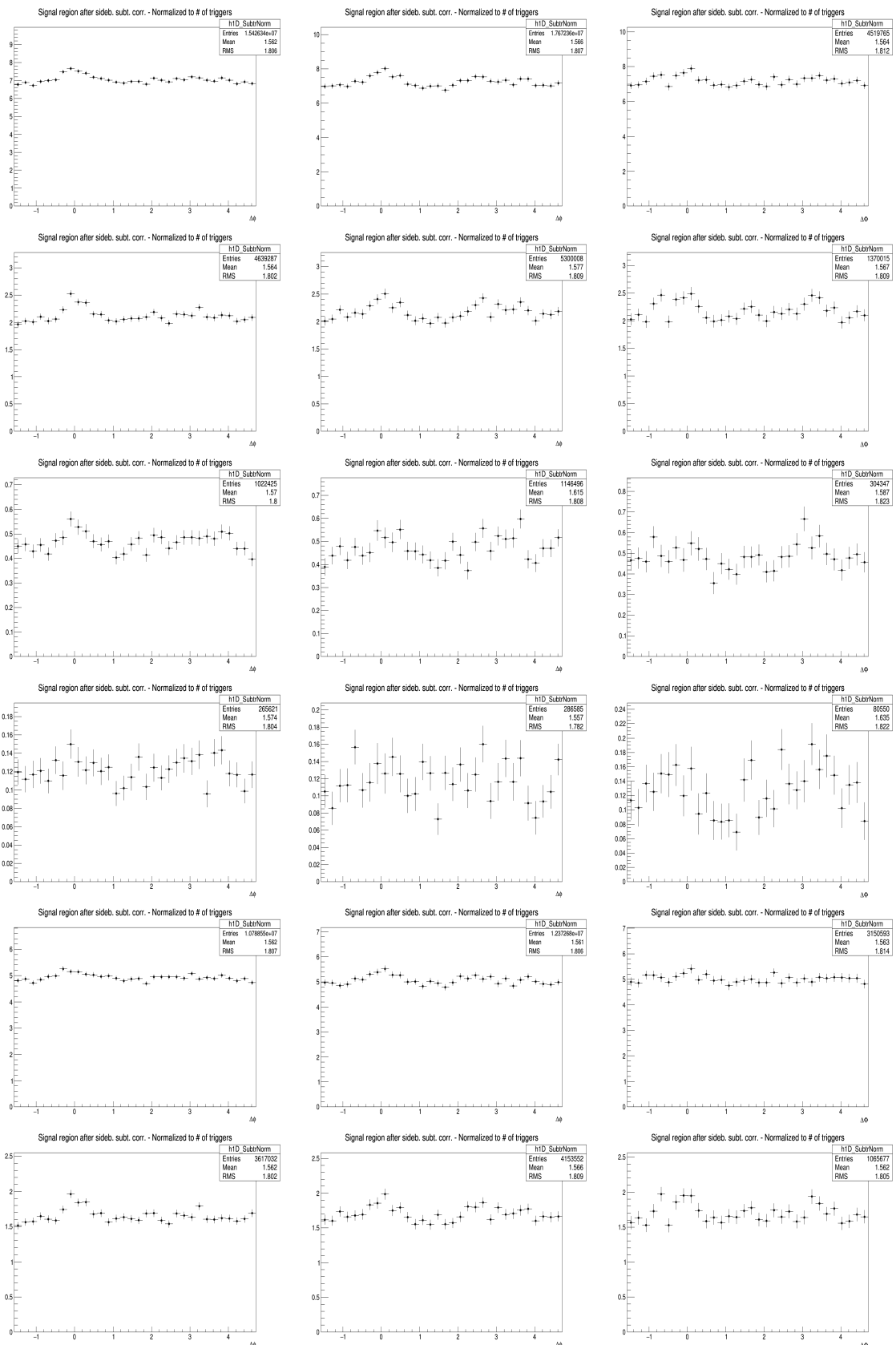


Figure 38: Ratios of correlation plots obtained with different associated DCA selections, after purity correction. First 6 plots: $p_T(D)$ 8-16 GeV/c, next 6 plots: $p_T(D)$ 16-24 GeV/c. Each bunch of 6 plots has $p_T(\text{assoc})$ of >0.3 , 0.3-1, >1 , 1-2, 2-3, <3 GeV/c, respectively.

pPb Sample	D ⁰				D [*]				D ⁺			
D Pt Range (GeV/c)	3-5	5-8	8-16	16-24	3-5	5-8	8-16	16-24	3-5	5-8	8-16	16-24
S and B Extraction	1%	1%	1%	3%	1%	1%	1%	2%	1%	1%	1%	2%
Background Correlation Shape	1%	1%	1%	3%	1%	1%	1%	3%	1%	1%	1%	3%
D meson Cut Variation	2%	2%	2%	2%	1.5%	1.5%	1%	1%	1%	1%	1%	3%

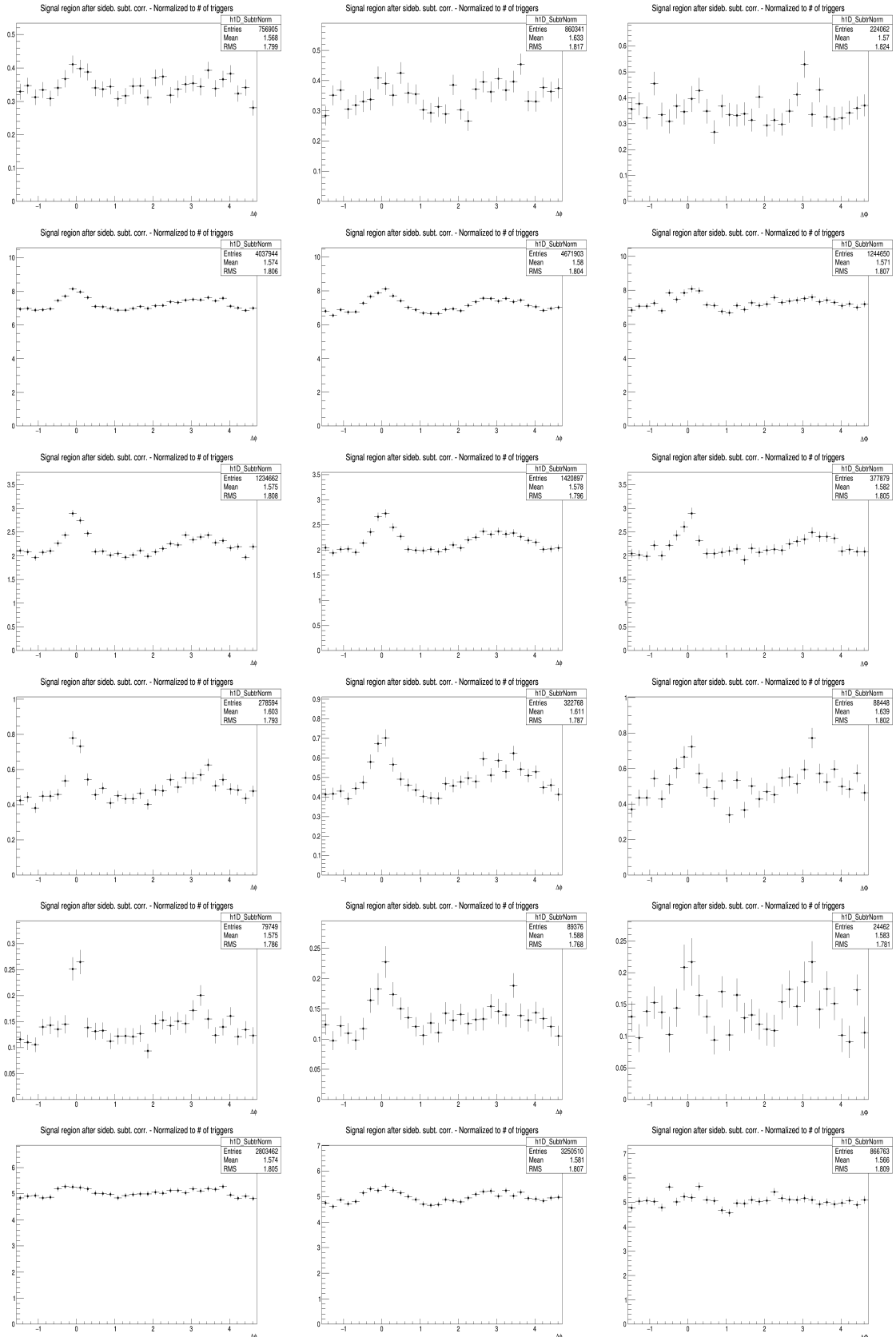
pPb Sample	D ⁰ , D [*] and D ⁺ (common for all the p _T (D) ranges)						
Assoc (p _T) Ranges (GeV/c)	> 0.3	> 1.0	> 2.0	> 3.0	0.3-1.0	1.0-2.0	2.0-3.0
Track Efficiency	3%	3%	3%	3%	3%	3%	3%
Purity	2.5%	1.5%	1.5%	1.5%	3%	1.5%	1.5%

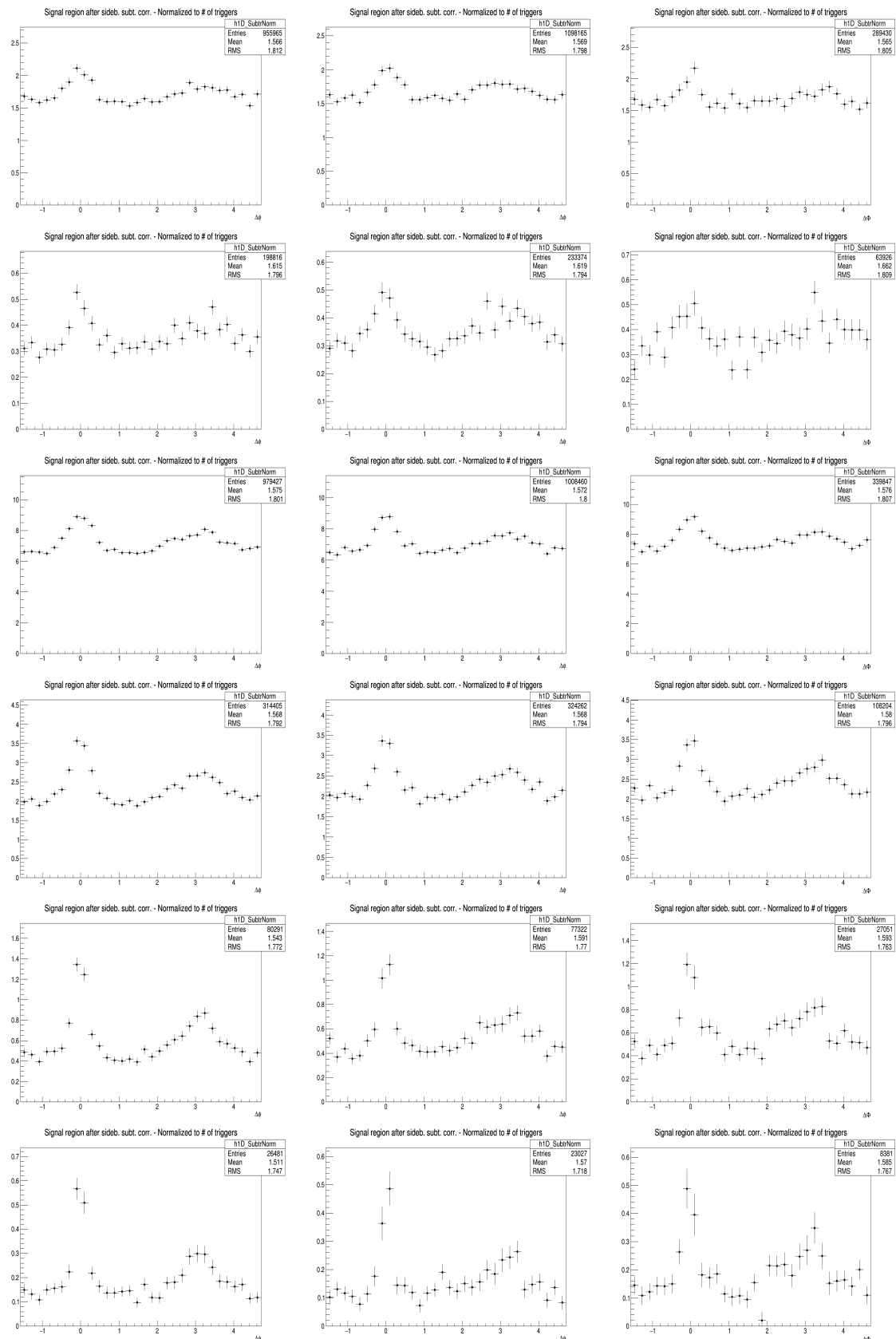
Figure 39: Summary of the $\Delta\phi$ -correlated uncertainties affecting the correlation distributions, for the three D-mesons, in the kinematic ranges analyzed.

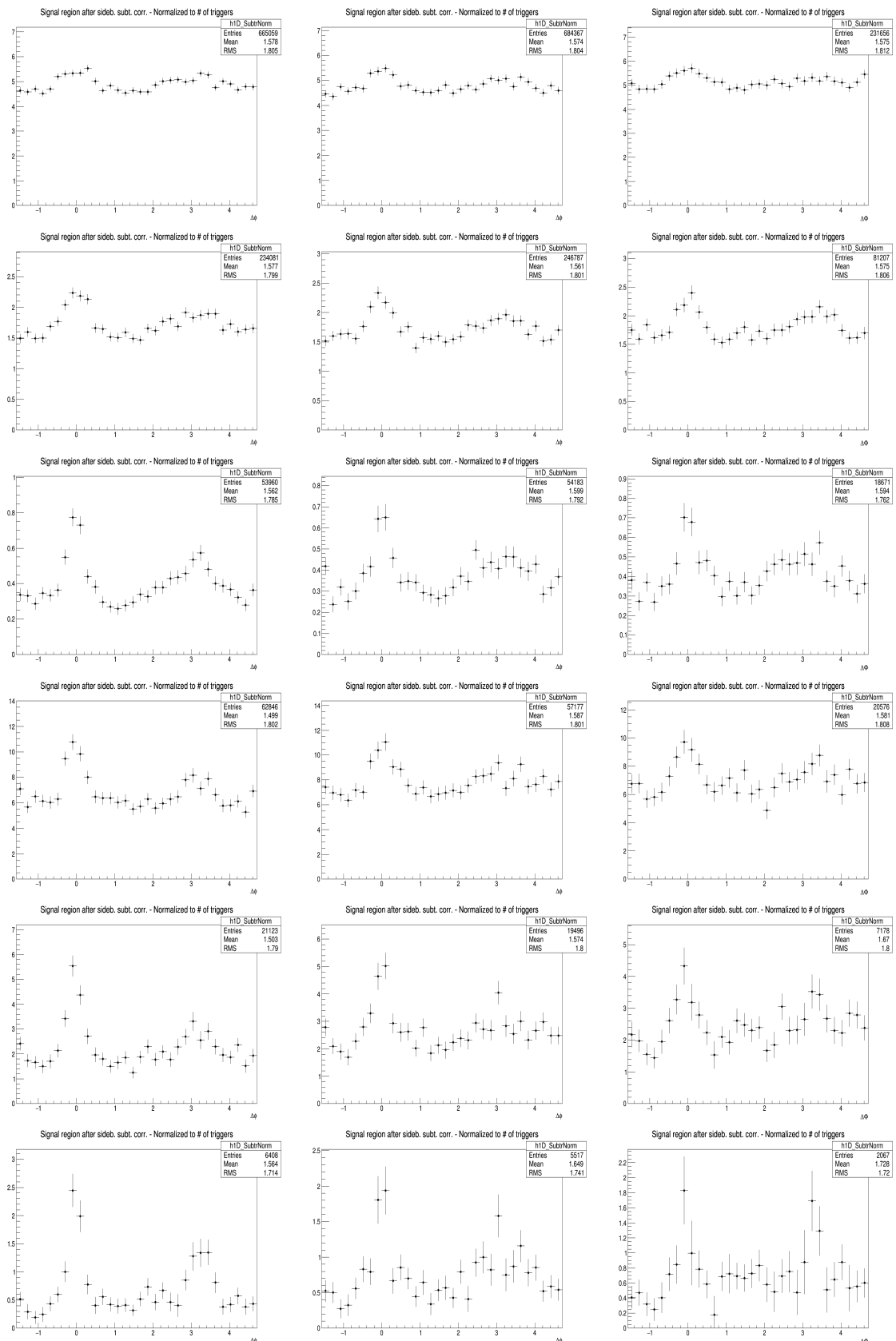


5.1 Comparing the three D meson correlation distributions

55







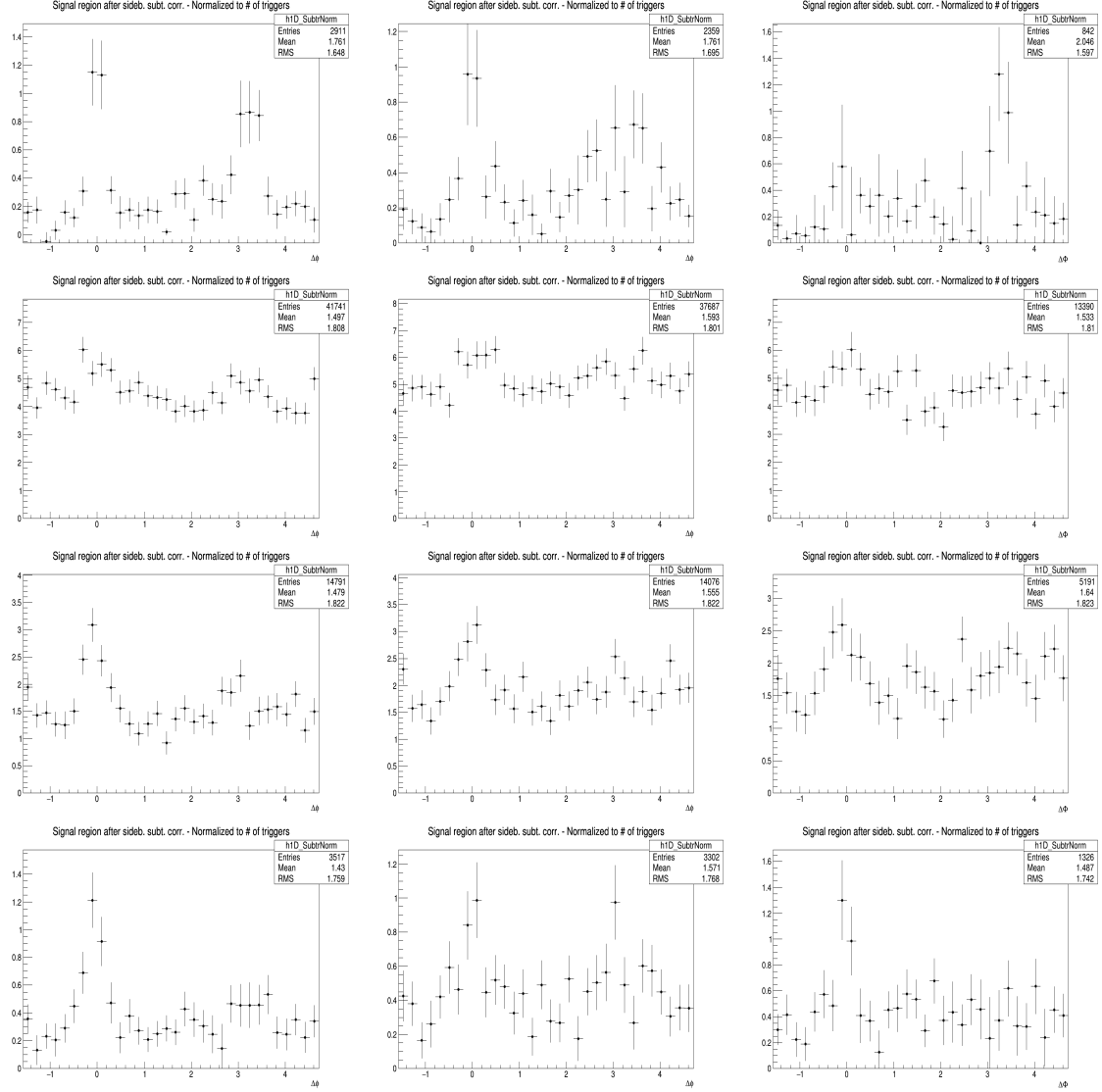


Figure 40: Corrected distribution of D-hadrons azimuthal correlations for the three species (apart from feed-down and purity), from analysis on the data sample, for the analyzed D-meson (**Column-Left:** D^0 , **Column-Middle:** D^+ and **Column-Right:** D^*) and different associated tracks p_T ranges (**Row 1-7:** $3 < Dp_T < 5 \text{ GeV}/c$, $p_T(\text{Assoc}) > 0.3, 1.0, 2.0, 3.0, 0.3-1.0, 1.0-2.0$ and $2.0-3.0 \text{ GeV}/c$ respectively), (**Row 8-14:** $5 < Dp_T < 8 \text{ GeV}/c$, $p_T(\text{Assoc}) > 0.3, 1.0, 2.0, 3.0, 0.3-1.0, 1.0-2.0$ and $2.0-3.0 \text{ GeV}/c$ respectively), (**Row 15-21:** $8 < Dp_T < 16 \text{ GeV}/c$, $p_T(\text{Assoc}) > 0.3, 1.0, 2.0, 3.0, 0.3-1.0, 1.0-2.0$ and $2.0-3.0 \text{ GeV}/c$ respectively) and (**Row 22-28:** $16 < Dp_T < 24 \text{ GeV}/c$, $p_T(\text{Assoc}) > 0.3, 1.0, 2.0, 3.0, 0.3-1.0, 1.0-2.0$ and $2.0-3.0 \text{ GeV}/c$ respectively)

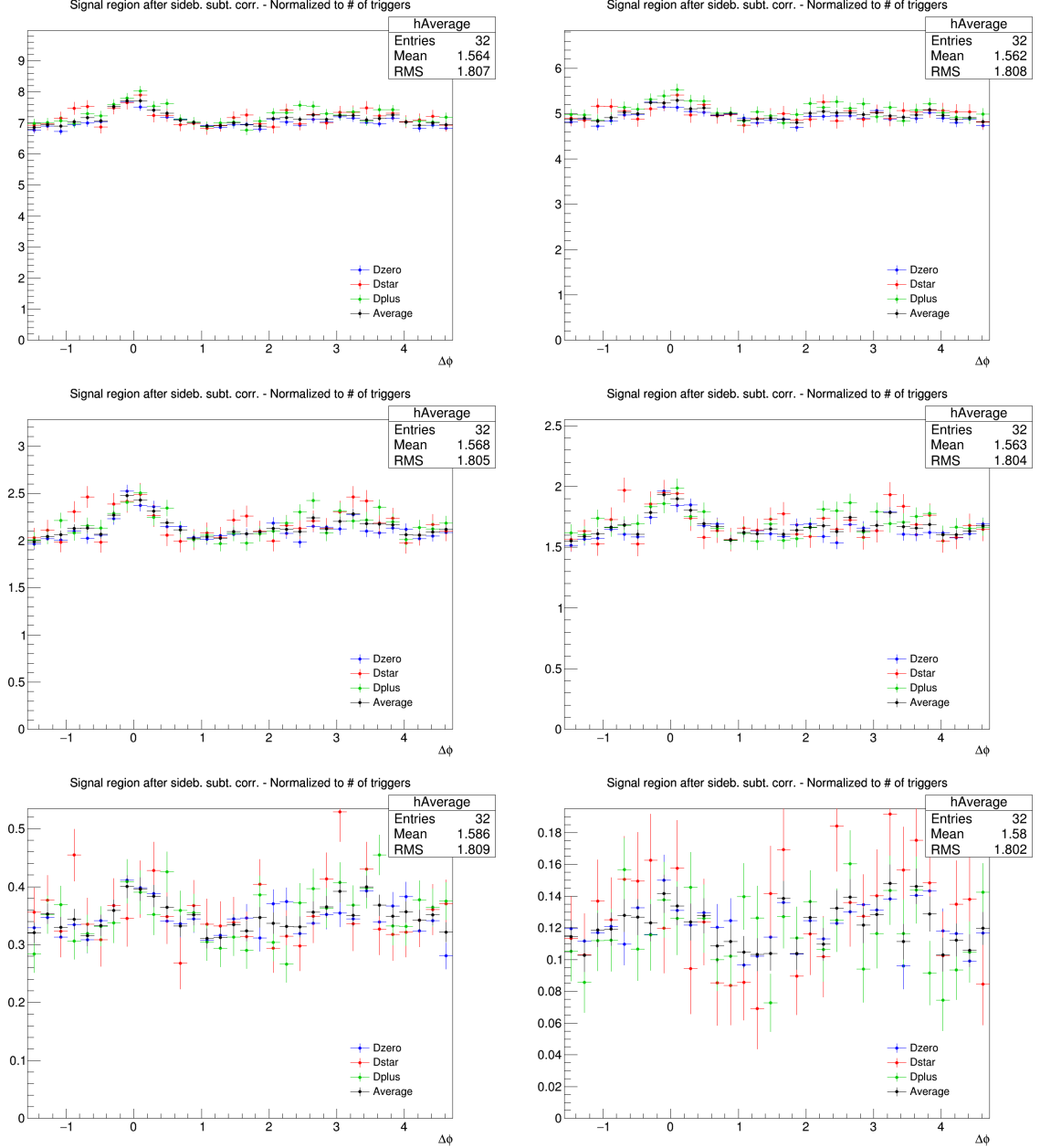


Figure 41: Superimposition of the corrected distribution of D-hadrons azimuthal correlations for the three species (apart from feed-down and purity), from analysis on the data sample, for the analyzed D-meson and different associated track p_T ranges, and D-meson p_T 3-5 GeV/c. **Panels from 1 to 6 of each page:** $p_T(\text{Assoc}) > 0.3$, $0.3-1.0$, >1.0 , $1.0-2.0$, $2.0-3.0$ and $>3.0 \text{ GeV}/c$

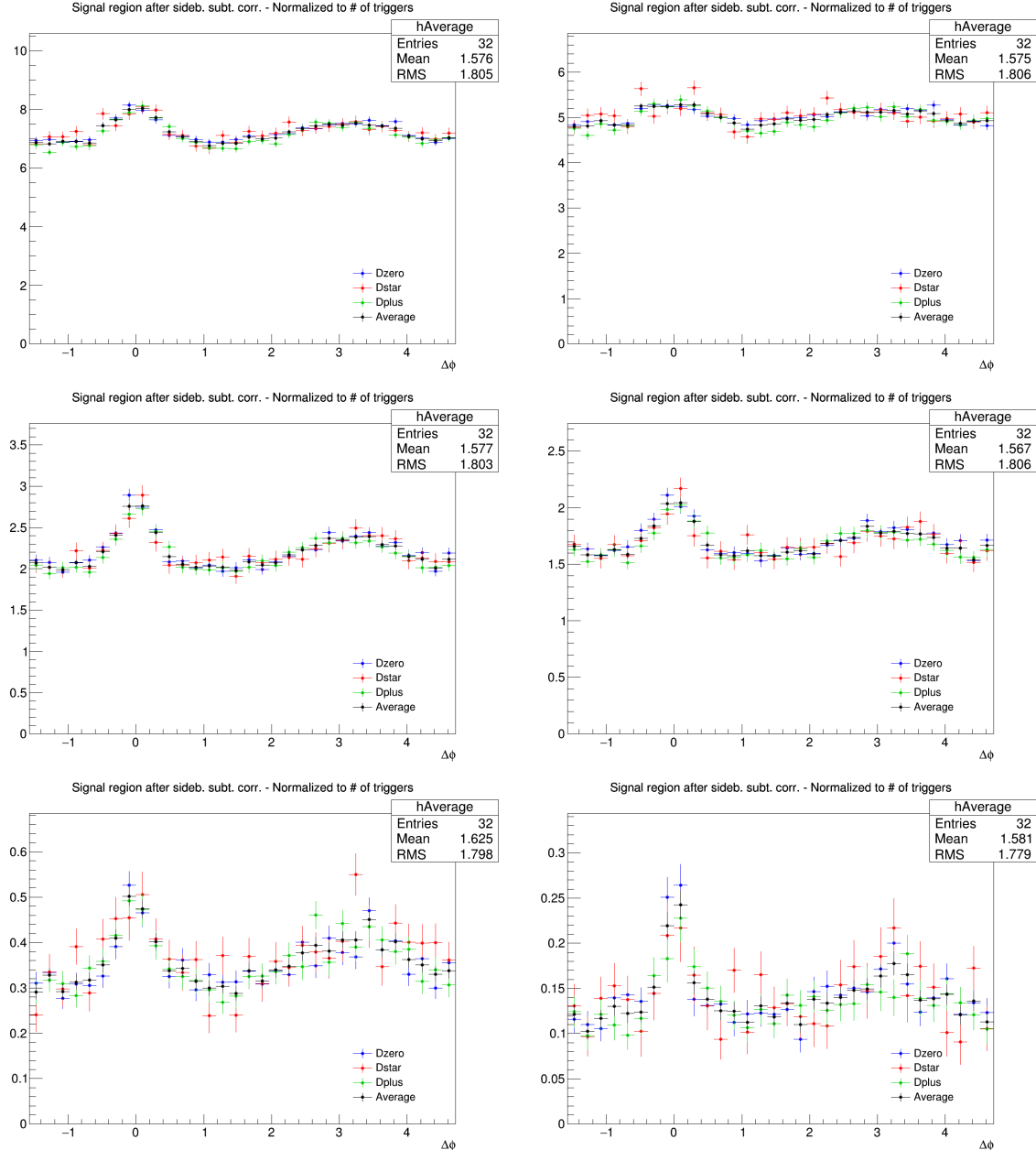


Figure 42: Superimposition of the corrected distribution of D-hadrons azimuthal correlations for the three species (apart from feed-down and purity), from analysis on the data sample, for the analyzed D-meson and different associated track p_T ranges, and D-meson p_T 5-8 GeV/c. **Panels from 1 to 6 of each page:** $p_T(\text{Assoc}) > 0.3$, $0.3\text{-}1.0$, >1.0 , $1.0\text{-}2.0$, $2.0\text{-}3.0$ and >3.0 GeV/c

- 604 An agreement of the distributions from the three mesons within the uncertainties is found in all the
605 kinematic ranges.
- 606 Despite being evaluated in the full 2π range, the range of final results was then reduced to $[0, \pi]$ radians,
607 reflecting the points outside that range over the value of 0. This allowed to reduce the impact of statistical
608 fluctuations on the data points (supposing equal statistics for a pair of symmetric bins, after the reflection
609 the relative statistical uncertainty for the resulting bin is reduced by a factor $1/\sqrt{2}$).

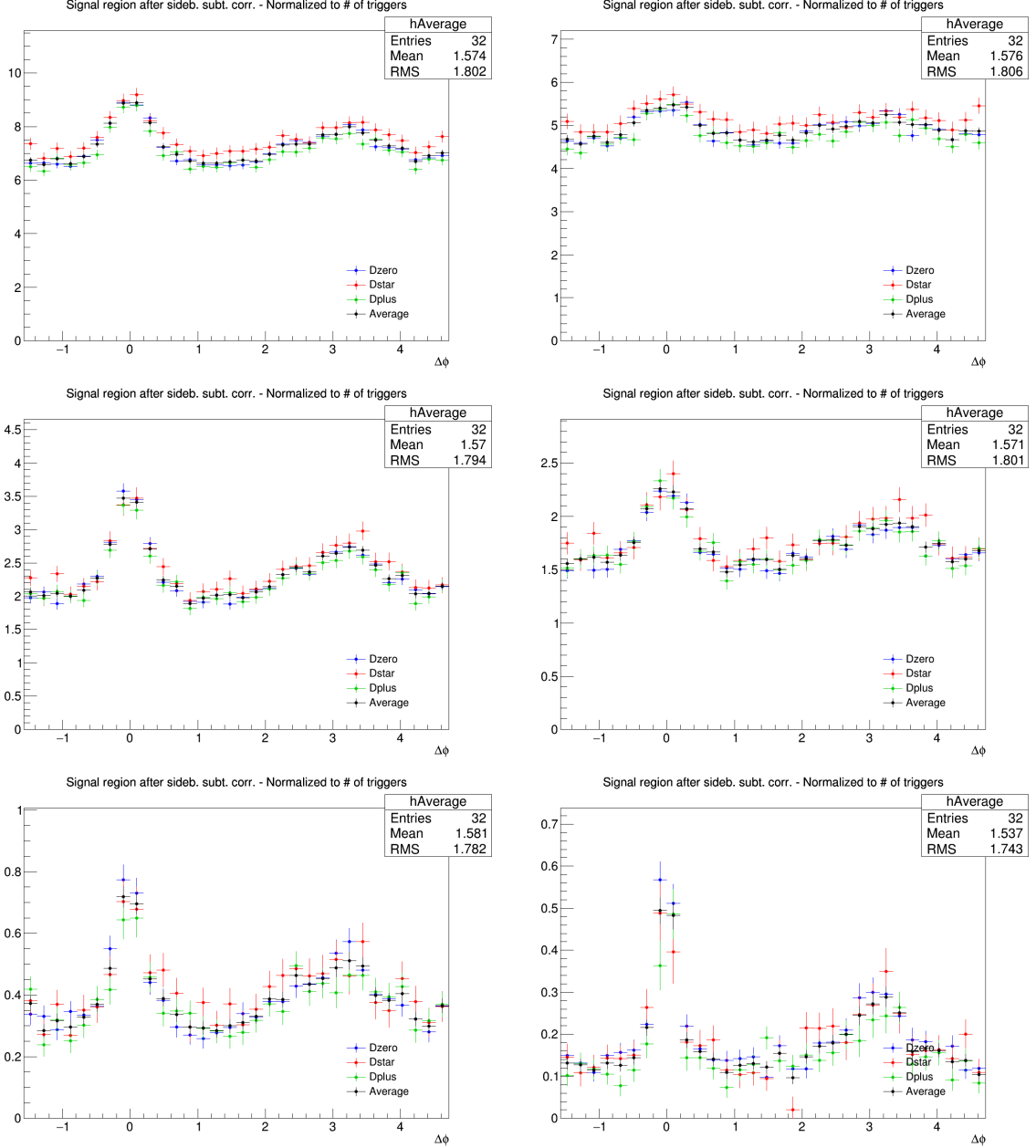


Figure 43: Superimposition of the corrected distribution of D-hadrons azimuthal correlations for the three species (apart from feed-down and purity), from analysis on the data sample, for the analyzed D-meson and different associated track p_T ranges, and D-meson p_T 8-16 GeV/c. **Panels from 1 to 6 of each page:** $p_T(\text{Assoc}) > 0.3$, $0.3-1.0$, >1.0 , $1.0-2.0$, $2.0-3.0$ and >3.0 GeV/c

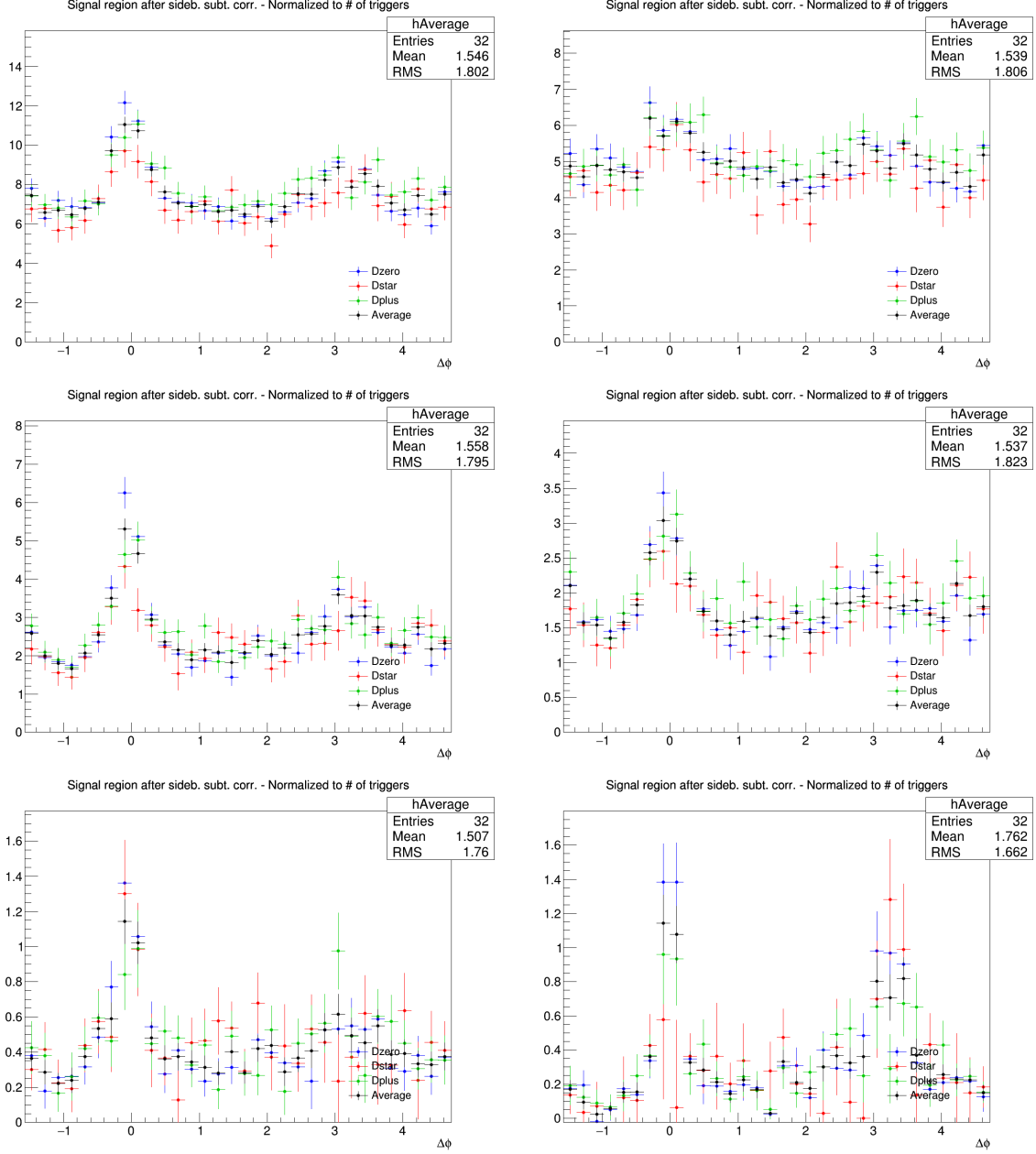


Figure 44: Superimposition of the corrected distribution of D-hadrons azimuthal correlations for the three species (apart from feed-down and purity), from analysis on the data sample, for the analyzed D-meson and different associated track p_T ranges, and D-meson p_T 16-24 GeV/c. **Panels from 1 to 6 of each page:** $p_T \text{ (Assoc)} > 0.3$, $0.3-1.0$, >1.0 , $1.0-2.0$, $2.0-3.0$ and >3.0 GeV/c

610 **5.2 Average of D⁰, D⁺ and D*⁺ results**

611 Given the compatibility within the uncertainties among the D⁰, D⁺ and D*⁺ azimuthal correlations, and
 612 since no large differences are visible in the correlation distributions observed in Monte Carlo simulations
 613 based on Pythia with Perugia0, 2010 and 2011 tunes¹, it was possible to perform a weighted average
 614 (eq. 5) of the azimuthal correlation distributions of D⁰, D⁺ and D*⁺, in order to reduce the overall
 615 uncertainties. Although some correlation between the mesons could be present (about the 30% of the
 616 D⁰, and also part of the D⁺, come from D*⁺ decays), the three selected D-meson samples can be treated
 617 as uncorrelated. The inverse of the sum in quadrature of the statistical uncertainty, of the S and B
 618 extraction uncertainty, and of the background shape systematic uncertainty was used as weight.

$$\left\langle \frac{1}{N_D} \frac{dN_{\text{assoc}}}{dp_T} \right\rangle_{D\text{mesons}} = \frac{\sum_{i=\text{meson}} w_i \frac{1}{N_D} \frac{dN_i^{\text{assoc}}}{d\Delta\varphi}}{\sum_{i=\text{meson}} w_i}, w_i = \frac{1}{\sigma_{i,\text{stat}}^2 + \sigma_{i,\text{uncorr.syst}}^2} \quad (5)$$

619 The statistical uncertainty and the uncertainties on S and B extraction and on background shape (those
 620 used for the weights) on the average were then recalculated using the following formula:

$$\sigma^2 = \frac{1}{n_D} \frac{\sum_{i=\text{meson}} w_i \sigma_i^2}{\sum_{i=\text{meson}} w_i} \quad (6)$$

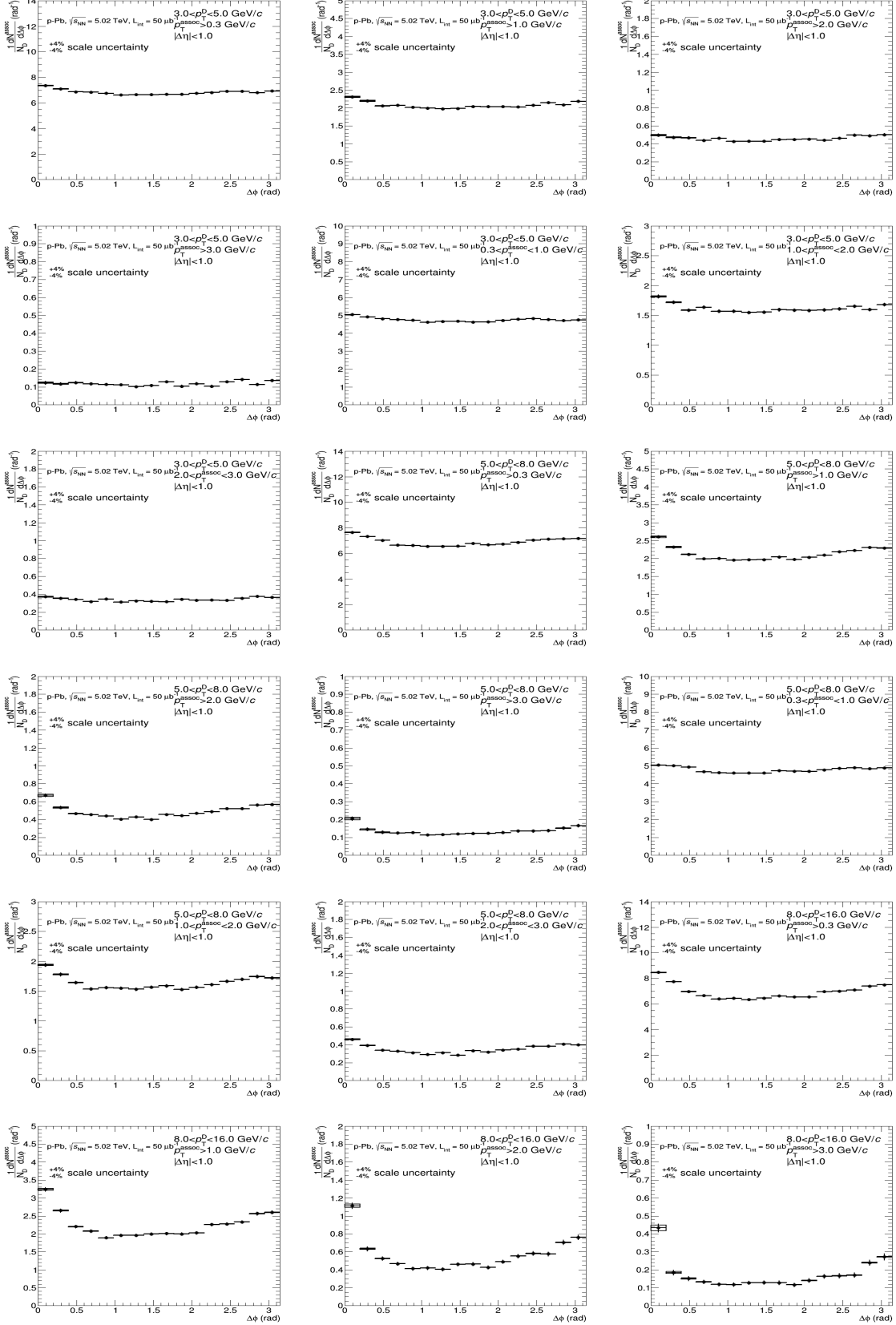
621 where n_D is the number of mesons considered in the average. It can be observed that for $\sigma_i^2 = 1/w_i$ the
 622 formula coincides with the standard one giving the uncertainty on a weighted average. The contribution
 623 to the average systematic uncertainty for those uncertainty sources not included in the weight definition,
 624 was evaluated via error propagation on the formula of the weighted average (5), resulting in equation
 625 (7) and (8) for sources considered uncorrelated and correlated among the mesons. In particular, the
 626 uncertainties on the associated track reconstruction efficiency, on the contamination from secondary, on
 627 the feed-down subtraction, and that resulting from the Monte Carlo closure test were considered fully
 628 correlated among the mesons, while those deriving from the yield extraction (included in the weight
 629 definition) and on the D meson reconstruction and selection efficiency were treated as uncorrelated.

$$\sigma^2 = \frac{\sum_{i=\text{meson}} w_i^2 \sigma_i^2}{(\sum_{i=\text{meson}} w_i)^2} \quad (7)$$

$$\sigma = \frac{\sum_{i=\text{meson}} w_i \sigma_i}{\sum_{i=\text{meson}} w_i} \quad (8)$$

630 Figure 45 shows the averages of the azimuthal correlation distributions of D⁰, D⁺ and D*⁺ and charged
 631 particles with $p_T > 0.3$ GeV/c, $0.3 < p_T < 1$ GeV/c, $p_T > 1$ GeV/c, $1 < p_T < 2$ GeV/c, $2 < p_T <$
 632 3 GeV/c, $p_T < 3$ GeV/c in the D meson p_T ranges $3 < p_T < 5$ GeV/c, $5 < p_T < 8$ GeV/c, $8 < p_T <$
 633 16 GeV/c and $16 < p_T < 24$ GeV/c. As expected, a rising trend of the height of the near-side peak with
 634 increasing D-meson p_T is observed, together with a decrease of the baseline level with increasing p_T of
 635 the associated tracks.

¹A slight near side hierarchy is present among the three meson results, with D*⁺ meson having a lower peak amplitude than D⁰ and D⁺. It was verified that this is induced by the presence of D⁰ and D⁺ mesons coming from D*⁺, the latter having on average a larger p_T and coming, hence, on average, from a larger p_T quark parton, which fragments in slightly more tracks in the near-side.



636 The usage of weighted average requires, as an underlying assumption, identical results expected for
 637 different species (or, at least, compatible within the uncertainties). Anyway, it was also verified that the
 638 usage of the arithmetic average instead of the weighted average increases the uncertainties on the points,

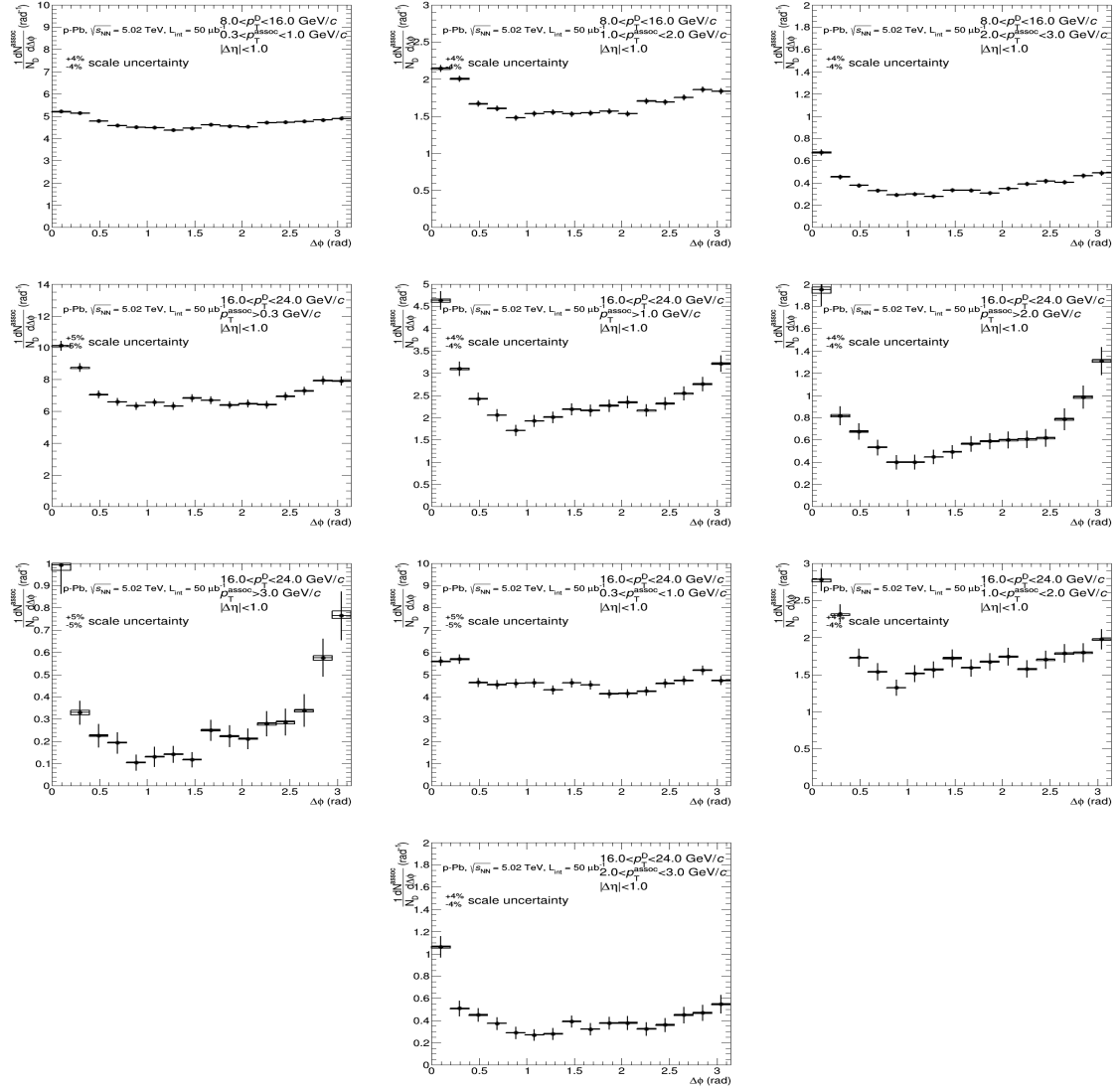


Figure 45: Average of D^0 , D^+ and D^{*+} azimuthal correlation distributions, in the D meson p_{T} ranges $3 < p_{\text{T}} < 5 \text{ GeV}/c$, $5 < p_{\text{T}} < 8 \text{ GeV}/c$, $8 < p_{\text{T}} < 16 \text{ GeV}/c$ and $16 < p_{\text{T}} < 24 \text{ GeV}/c$, with associated tracks with $p_{\text{T}} > 0.3 \text{ GeV}/c$, $p_{\text{T}} > 1 \text{ GeV}/c$ and $0.3 < p_{\text{T}} < 1 \text{ GeV}/c$.

but produces a negligible shift of their central values.

5.3 Fit observable p_T trends and uncertainties

In order to extract quantitative and physical information from the data correlation patterns, the averaged D-h correlation distributions are fitted with two Gaussian functions (with means fixed at $\Delta\varphi=0$ and $\Delta\varphi=\pi$ values), plus a constant term (baseline). A periodicity condition is also applied to the fit function to obtain the same value at the bounds of 2π range. The expression of the fit expression is reported below (equation 9):

$$f(\Delta\varphi) = c + \frac{Y_{NS}}{\sqrt{2\pi}\sigma_{NS}} e^{\frac{(\Delta\varphi-\mu_{NS})^2}{2\sigma_{NS}^2}} + \frac{Y_{AS}}{\sqrt{2\pi}\sigma_{AS}} e^{\frac{(\Delta\varphi-\mu_{AS})^2}{2\sigma_{AS}^2}} \quad (9)$$

where baseline is calculated as the weighted average of the points lying in the so-called "transverse region", i.e. the interval $\frac{\pi}{4} < |\Delta\varphi| < \frac{\pi}{2}$.

An example of the results from the fit is shown in Figure 46

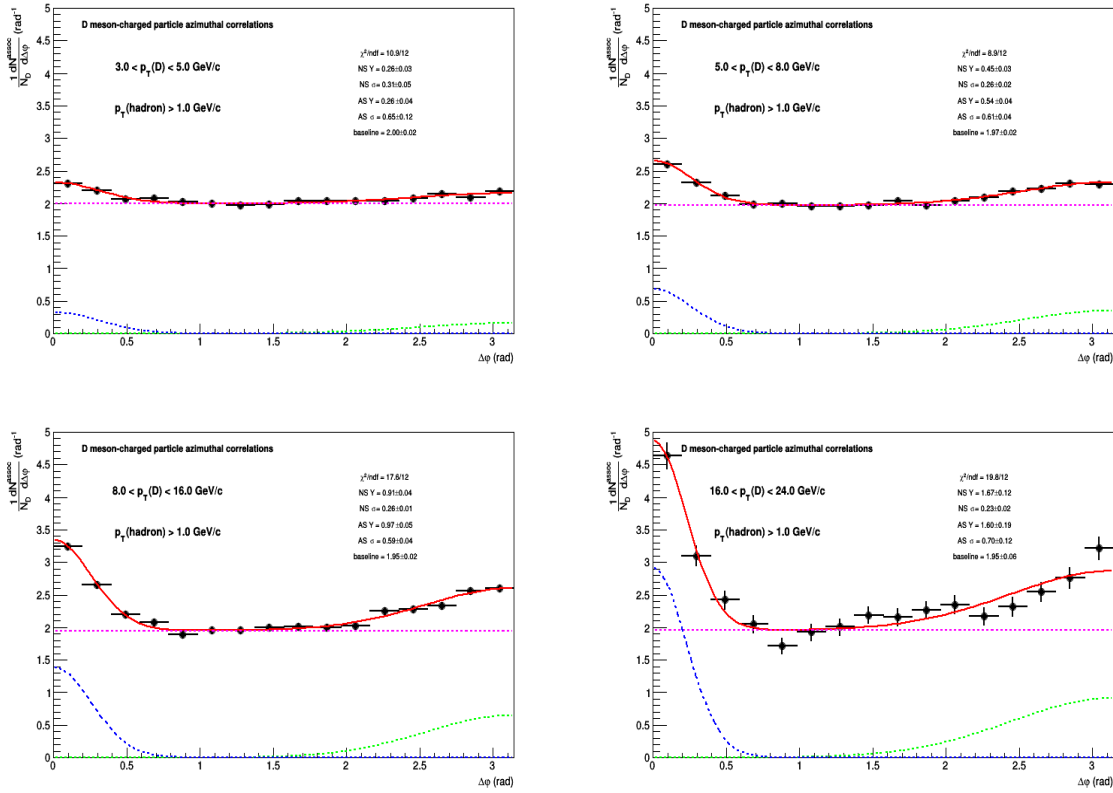


Figure 46: Example of fit to azimuthal correlation distributions and baseline estimation.

From the fit outcome is it possible to retrieve the near-side and away-side yield and widths (integral and sigma of the Gaussian functions, respectively), as well as the baseline height. The near-side observables give information on the multiplicity and angular spread of the tracks from the fragmentation of the charm jet which gave birth to the D-meson trigger, while at first order the away-side observables are related to the hadronization of the charm parton produced in the opposite direction (though the presence of NLO processes for charm production breaks the full validity of this assumption). The baseline value is a rough indicator of the underlying event multiplicity, though below the baseline level also charm and beauty-related pairs are contained (especially in cases of NLO production for the heavy quarks).

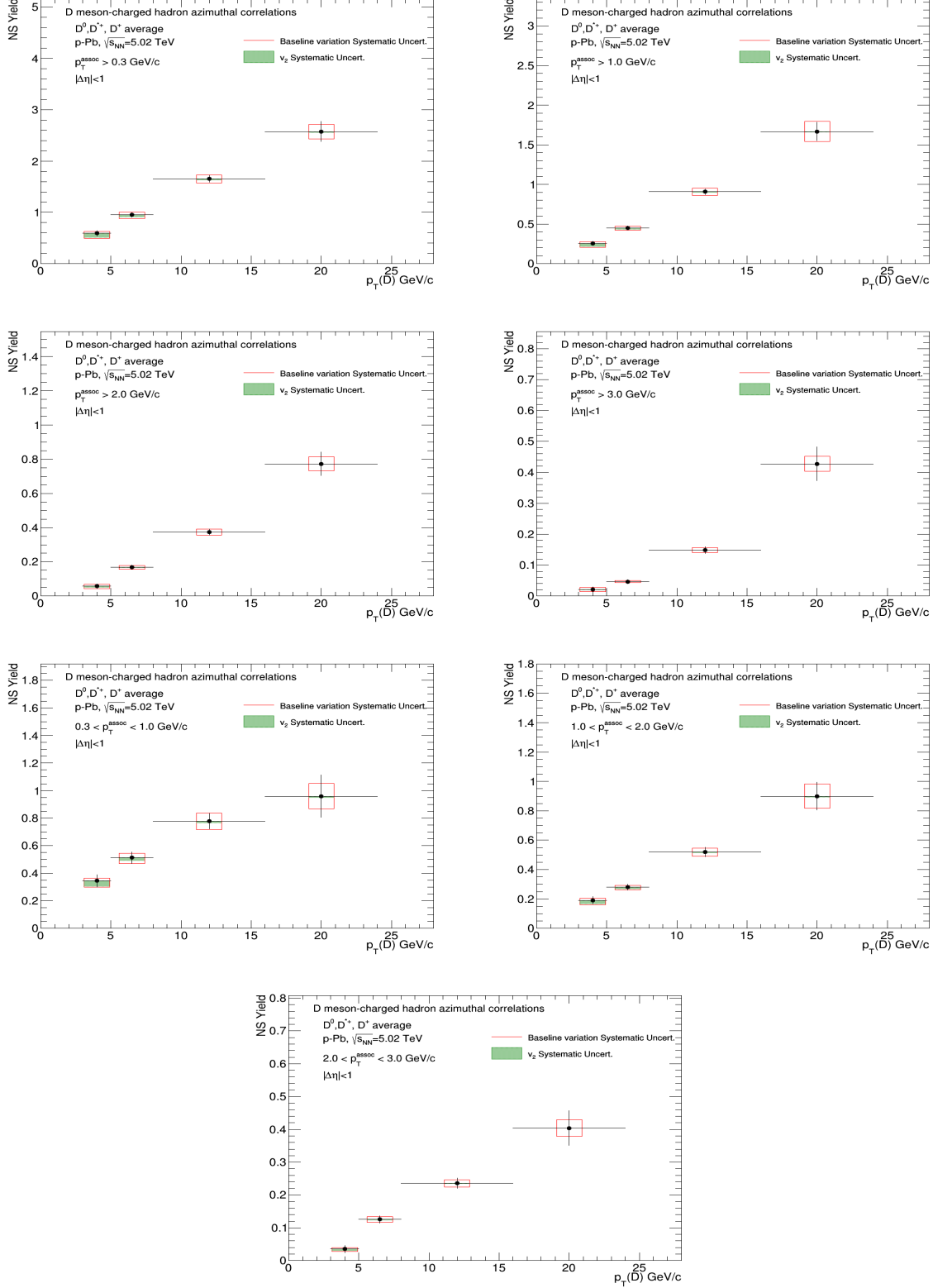
657 The evaluation of the systematic uncertainties on the observables obtained from the fits is performed as
 658 follows:

- 659 – The fits are repeated by changing the range of the transverse region in which the baseline is eval-
 660 uated. Alternate definitions of $\frac{\pi}{4} < |\Delta\phi| < \frac{3\pi}{8}$, $\frac{3\pi}{8} < |\Delta\phi| < \frac{\pi}{2}$ and $\frac{\pi}{4} < |\Delta\phi| < \frac{5\pi}{8}$ are considered.
- 661 – In addition, $\Delta\phi$ correlation points are shifted to the upper and lower bounds of their uncorrelated
 662 systematic boxes, and the refitted.
- 663 – The maximum variation of the parameters between the fit outcomes defined in the previous points
 664 is considered as systematic uncertainty for the near-side and away-side widths.
- 665 – For the estimation of the baseline and of the near-side and away-side yields, the previous value is
 666 added in quadrature with the $\Delta\phi$ -correlated systematics in the correlation distributions, since these
 667 values are affected by a change in the global normalization of the distributions.
- 668 – In addition, for all the fit observables, another fit variation is performed assuming, instead of a flat
 669 baseline, a $v_2\Delta$ -like modulation, with the following v_2 values for the associated tracks: 0.04 (0.3-1
 670 GeV/c), 0.06 (>0.3 GeV/c), 0.08 (1-2 GeV/c), 0.09 (>1 GeV/c, 2-3 GeV/c), 0.1 (>3 GeV/c),
 671 on the basis of ATLAS preliminary results for heavy-flavour muons at 8 TeV; for the D-meson
 672 triggers the following v_2 values were instead assumed: 0.05 (3-5 GeV/c), 0.03 (5-8 GeV/c), 0.02
 673 (8-24 GeV/c), on the basis of previous ALICE measurements in p-Pb collisions at 5 TeV [3]. The
 674 difference of the fit observables with respect to the standard fits is taken as uncertainty. Due to its
 675 peculiarity, this systematic uncertainty is summed in quadrature with the others to obtain the total
 676 uncertainty, but is also shown separately in the figures.

$$\sigma^{syst} = \sqrt{(Max(\Delta par^{ped.mode}, \Delta par^{\Delta\phi point}))^2 + (\sigma_{Syst}^{corr})^2} \quad (10)$$

677 5.3.1 Results for near-side yield and width, away-side yield and width, and baseline

678 Figures 47, 48, 49, 50 and 51 shows the near-side associated yield, width (the sigma of the Gaussian
 679 part of the fit functions), away-side associated yield, width and the height of the baseline, for the average
 680 correlation distributions, in the kinematic ranges studied in the analysis, together with their statistical
 681 and systematic uncertainties. For each kinematic range, the correspondent plot showing the systematic
 682 uncertainty of the considered observable from the variation of the fit procedure is reported as well (which
 683 is the full systematic uncertainty for the widths). Figures 52, 53, 54, 55 and 56 show the full systematic
 684 uncertainties for near side yield and width, away side yield and width, and baseline, with the breakdown
 685 of fit variation, $v_2\Delta$ and $\Delta\phi$ correlated systematic uncertainties.



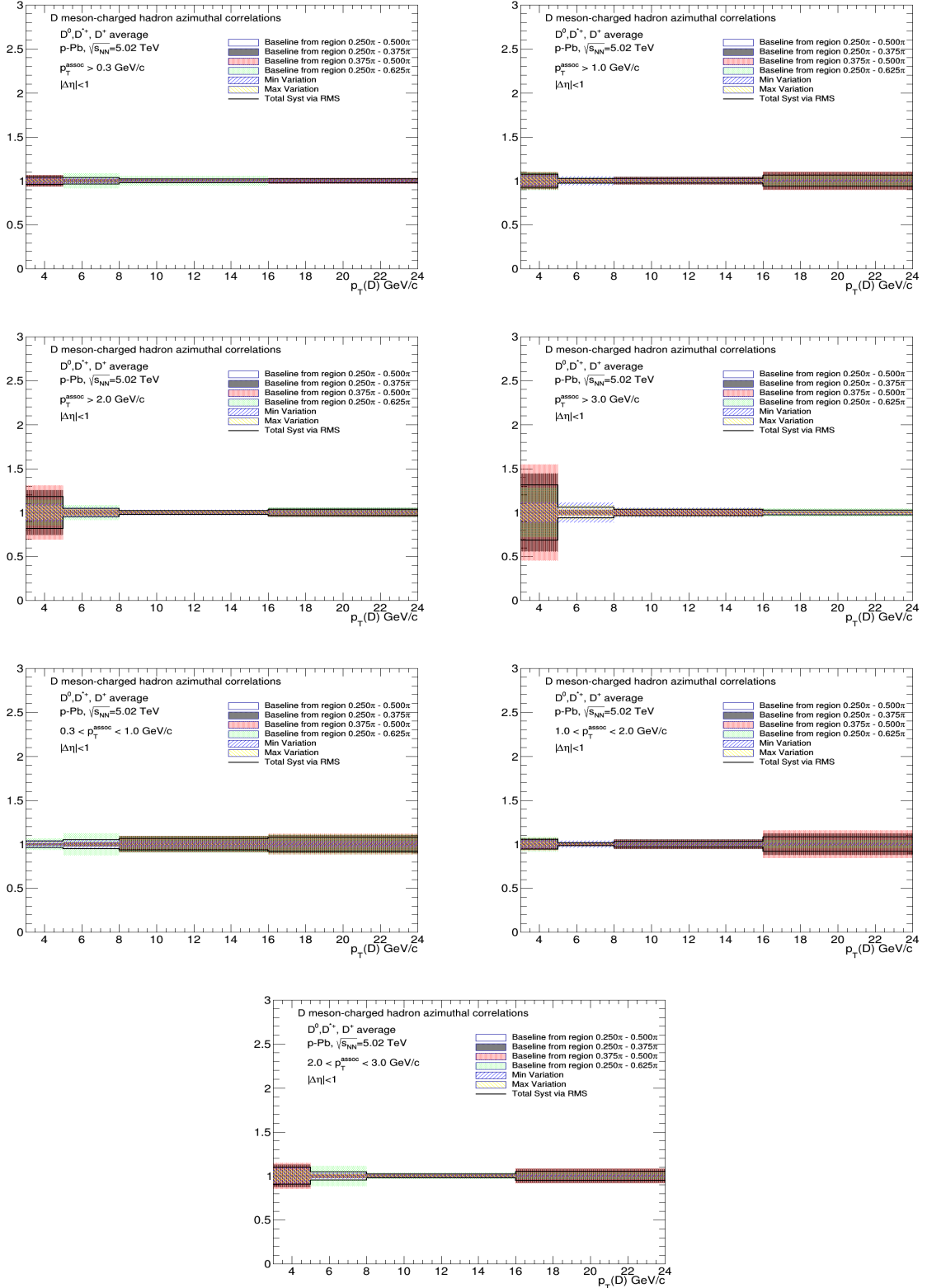
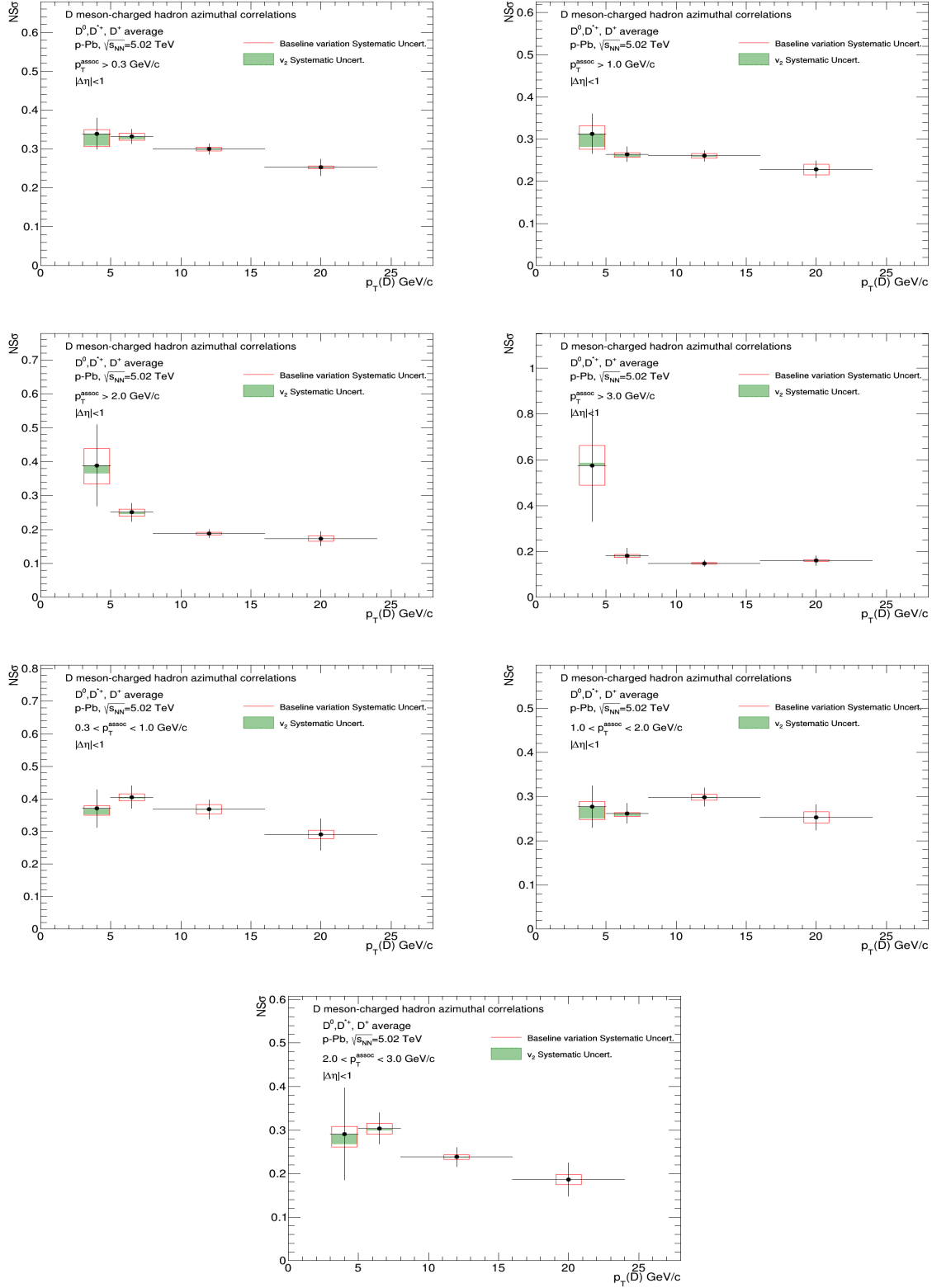


Figure 47: Top panels: near side yield $p_T(D)$ trend for the D-meson average, extracted from fit to the azimuthal correlation distributions, for all the analyzed kinematic ranges of associated track p_T . Bottom panels: for each kinematic region the systematic uncertainties coming from the variation of the fit procedure are shown.



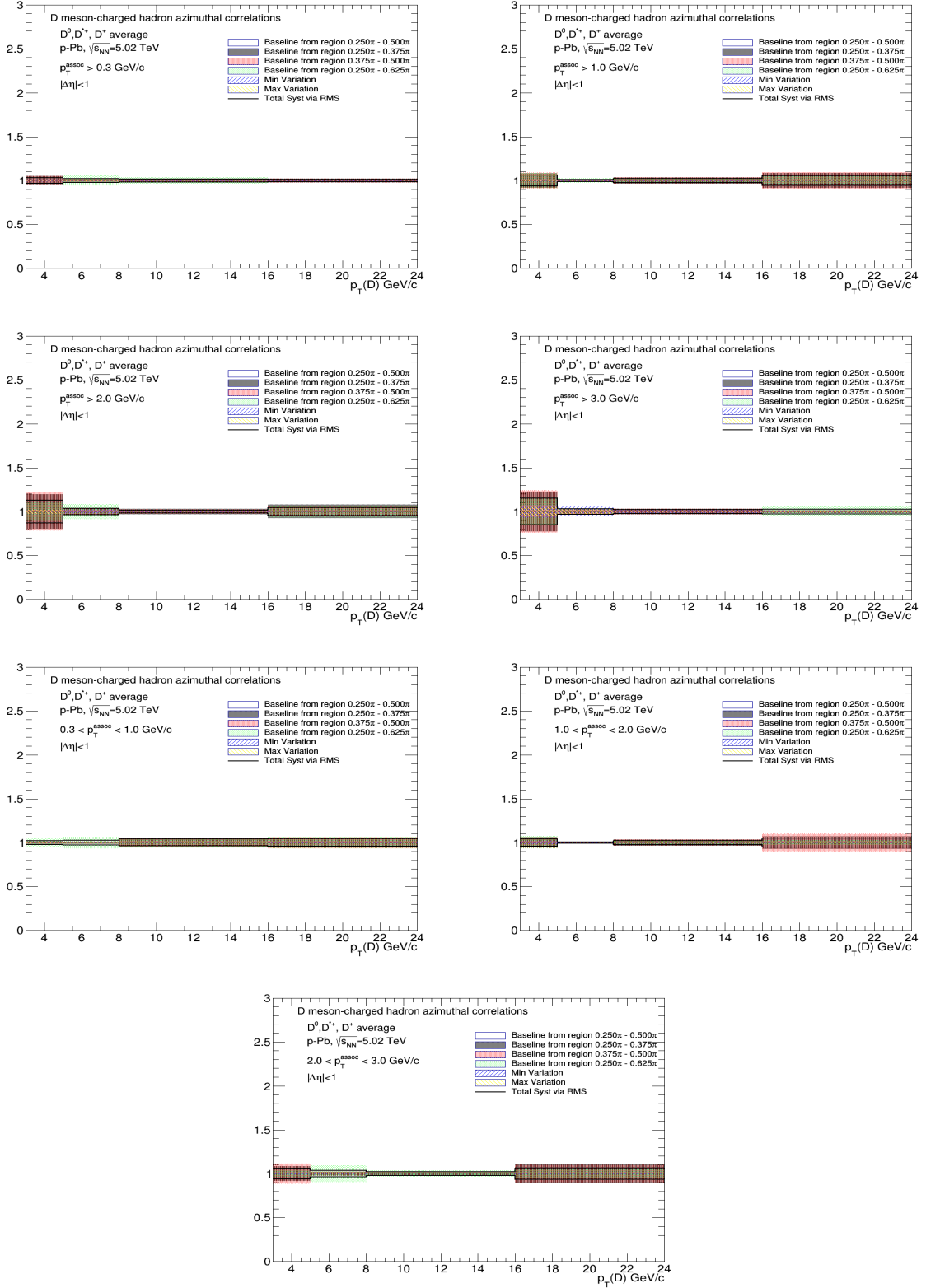
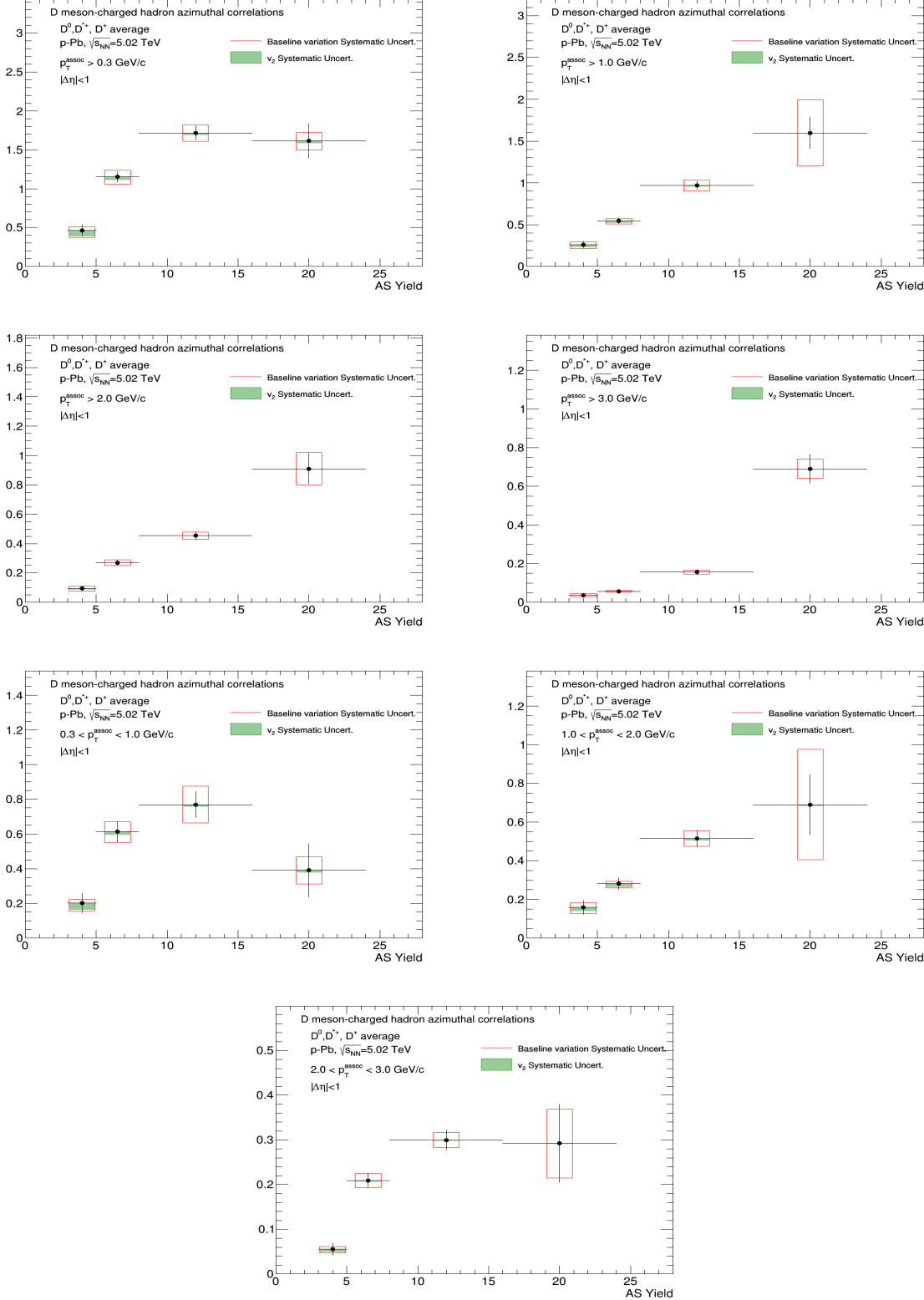


Figure 48: Top panels: near side width $p_T(D)$ trend for the D-meson average, extracted from fit to the azimuthal correlation distributions, for all the analyzed kinematic ranges of associated track p_T . Bottom panels: for each kinematic region the systematic uncertainties coming from the variation of the fit procedure are shown.



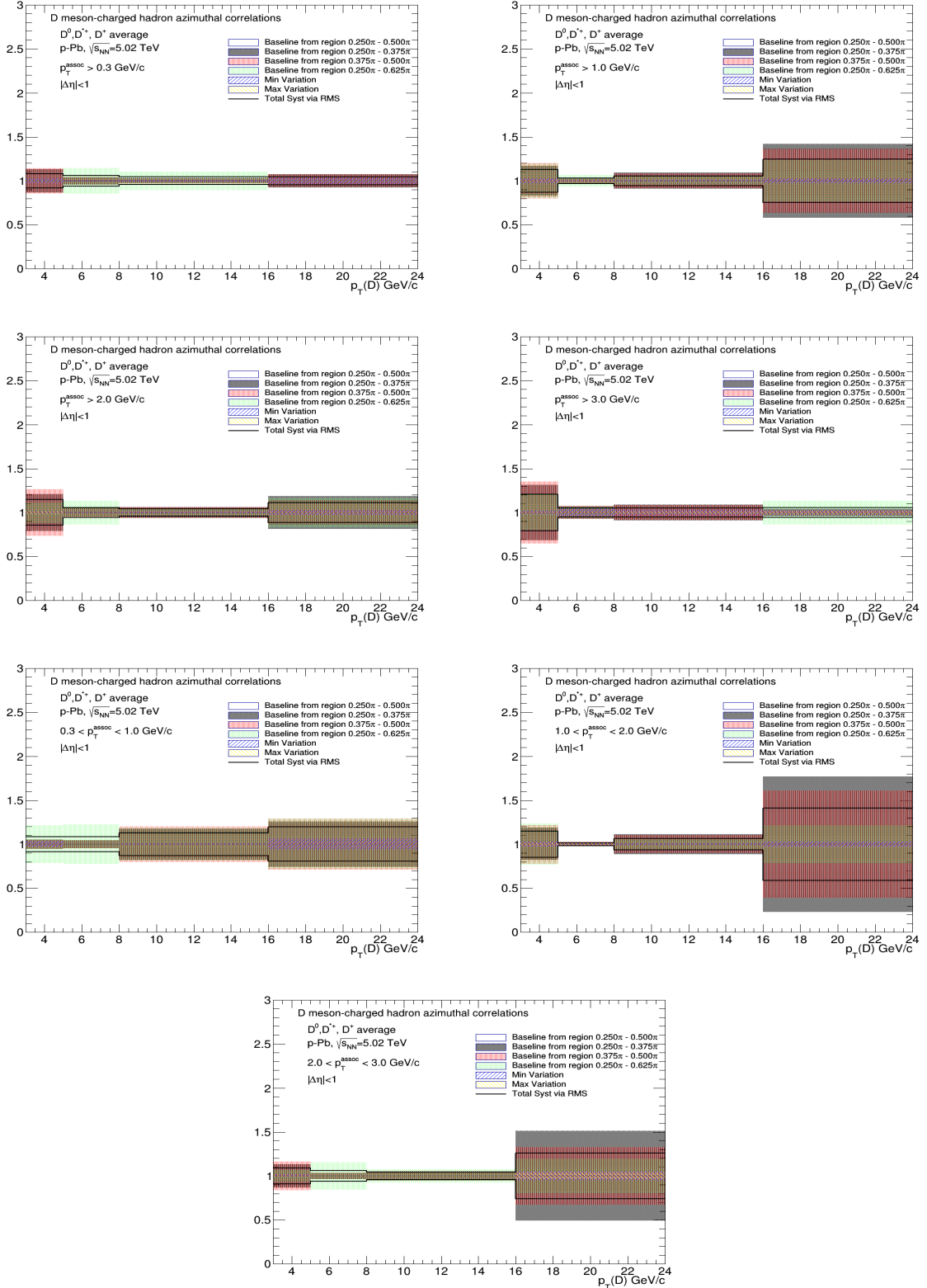
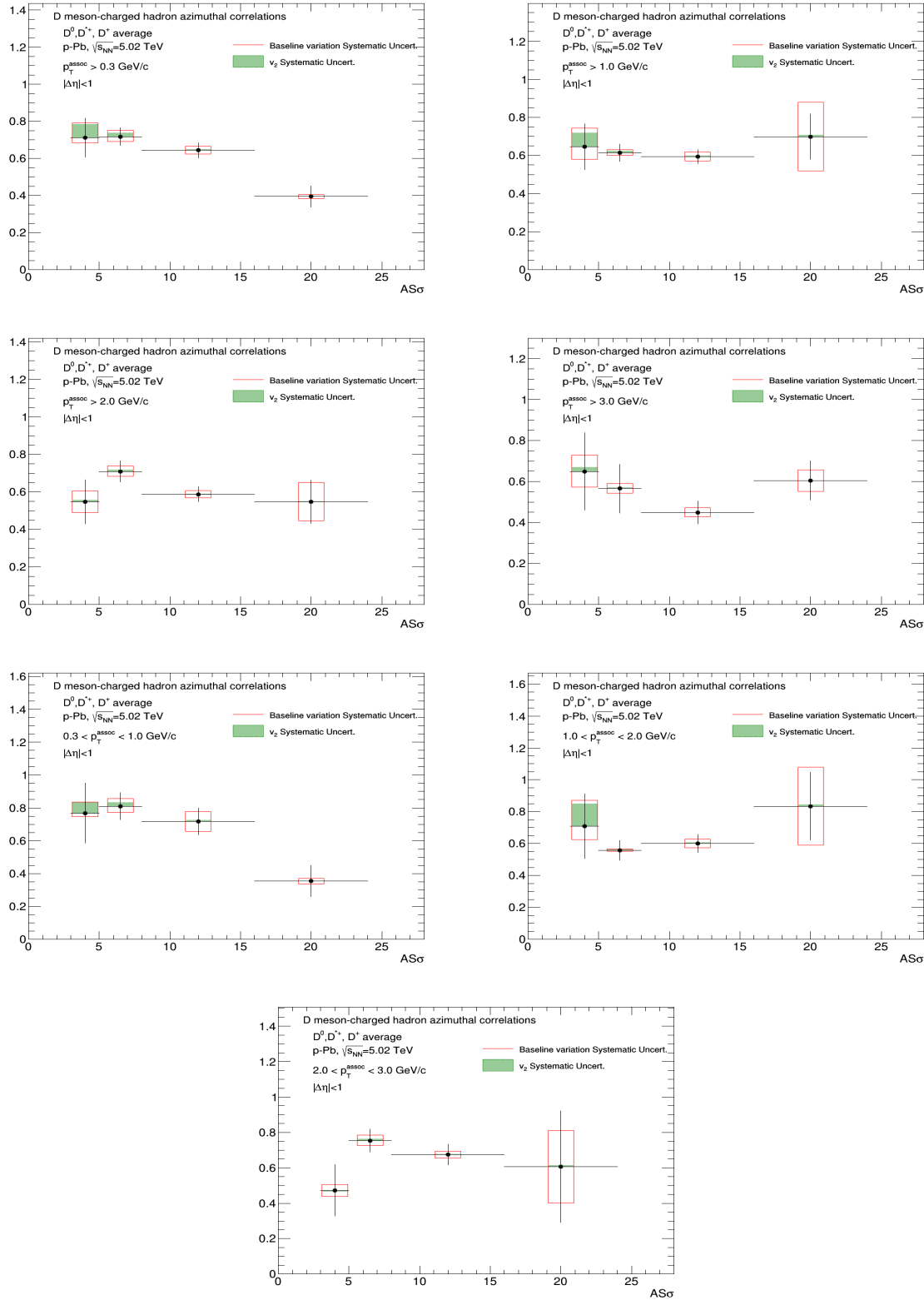


Figure 49: Top panels: away side yield $p_T(D)$ trend for the D-meson average, extracted from fit to the azimuthal correlation distributions, for all the analyzed kinematic ranges of associated track p_T . Bottom panels: for each kinematic region the systematic uncertainties coming from the variation of the fit procedure are shown.



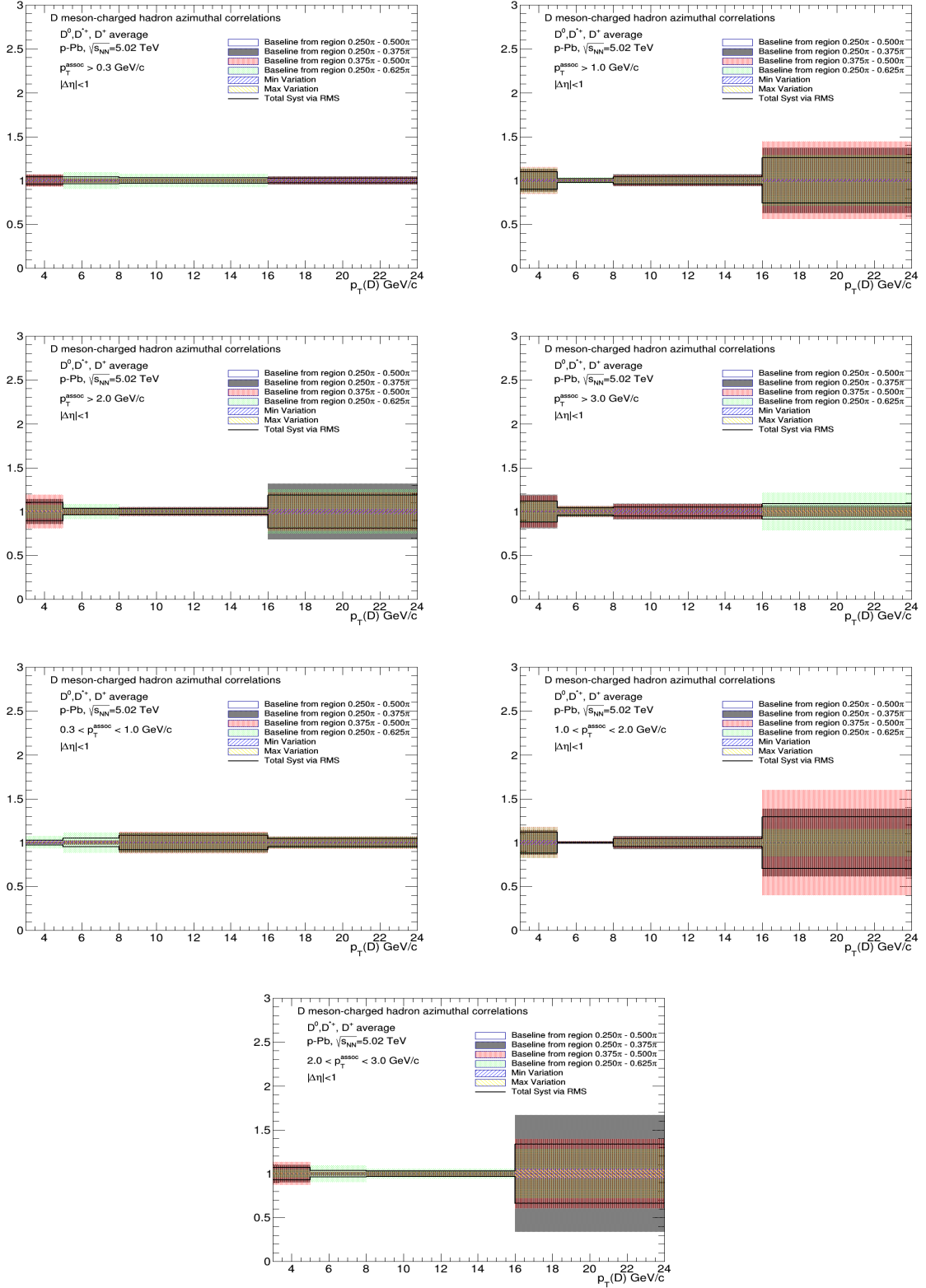
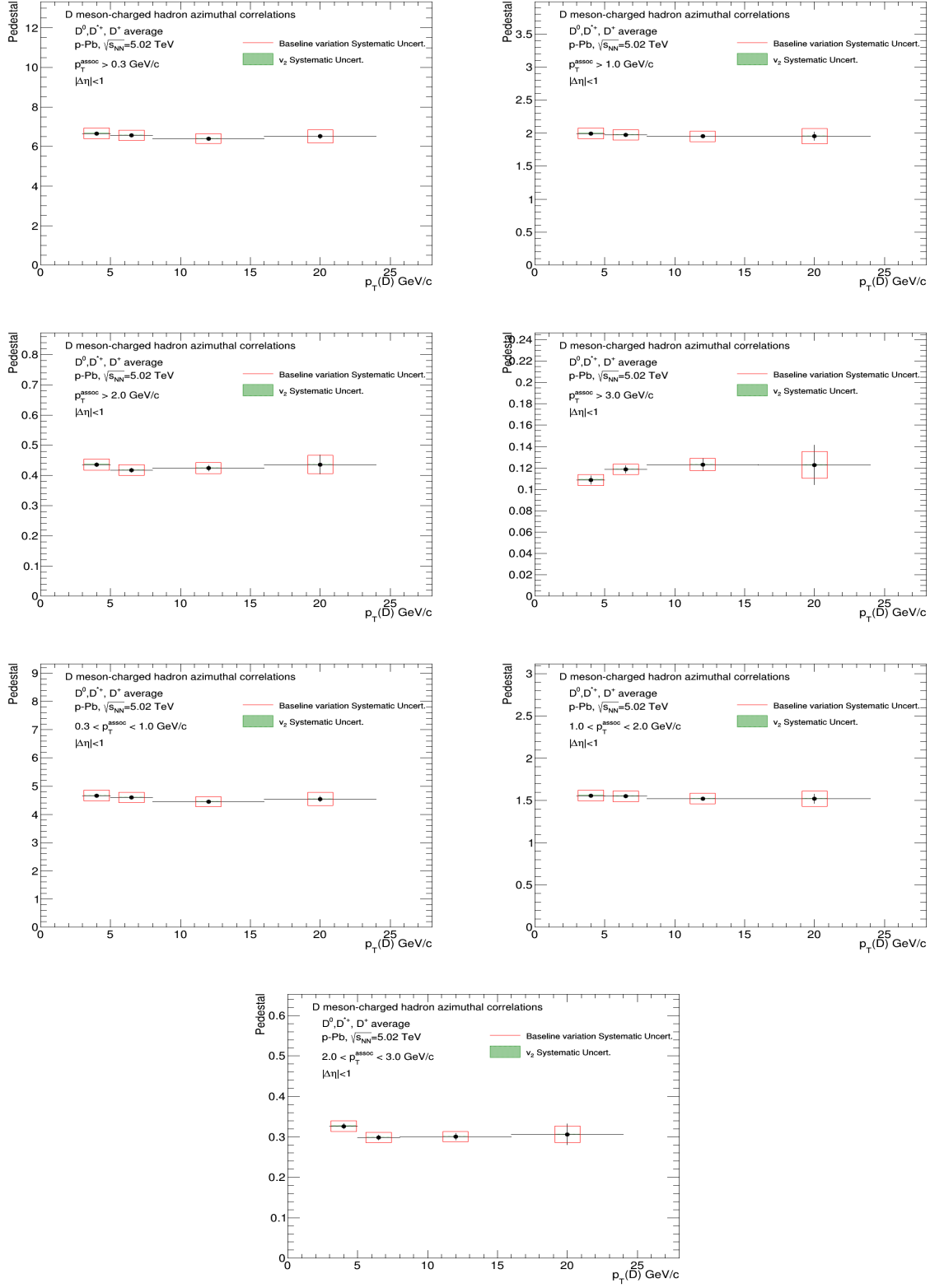


Figure 50: Top panels: away side width $p_T(D)$ trend for the D-meson average, extracted from fit to the azimuthal correlation distributions, for all the analyzed kinematic ranges of associated track p_T . Bottom panels: for each kinematic region the systematic uncertainties coming from the variation of the fit procedure are shown.



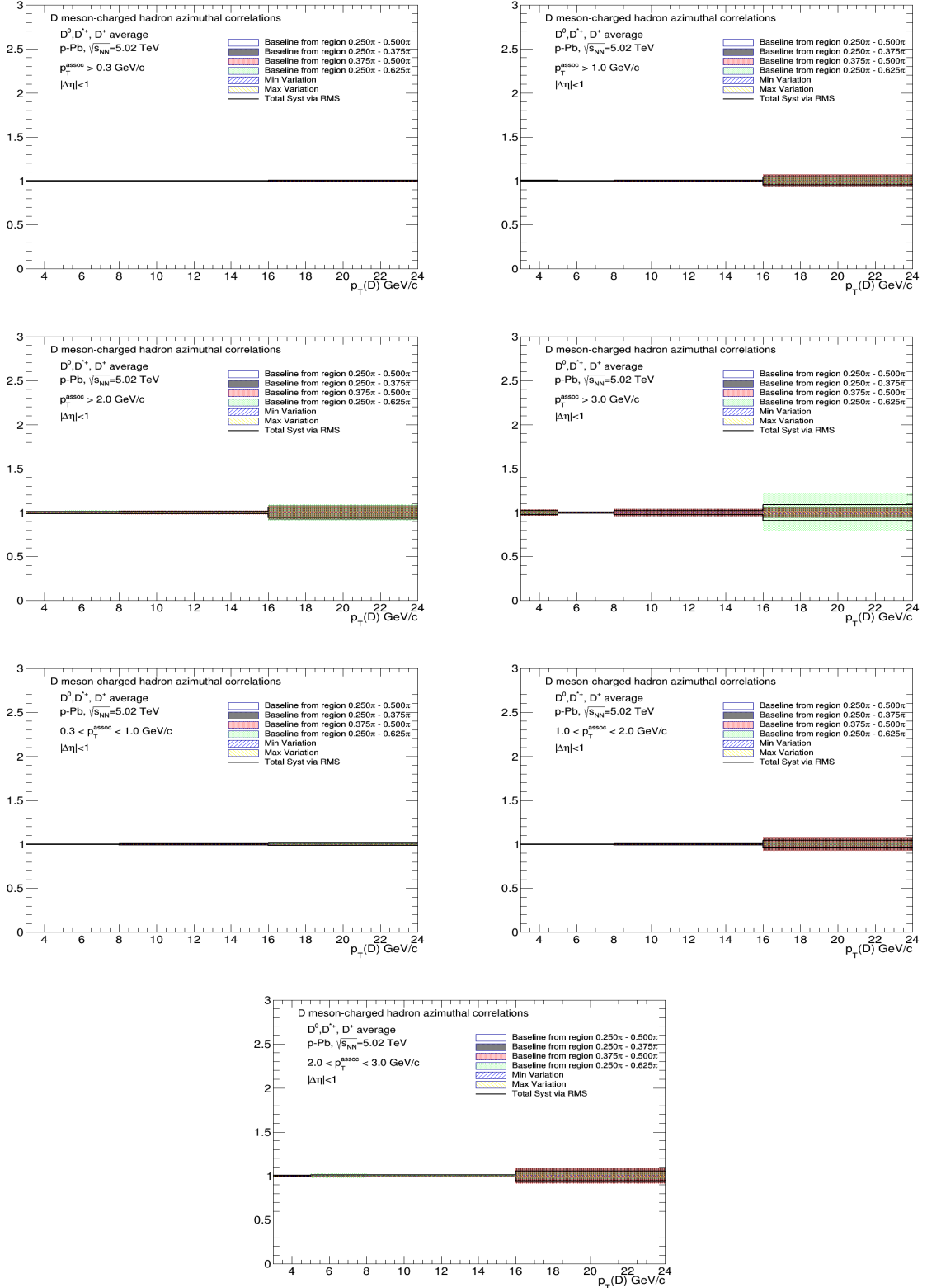


Figure 51: Top panels: baseline height trend for the D-meson average, extracted from fit to the azimuthal correlation distributions, for all the analyzed kinematic ranges of associated track p_T . Bottom panels: for each kinematic region the systematic uncertainties coming from the variation of the fit procedure are shown.

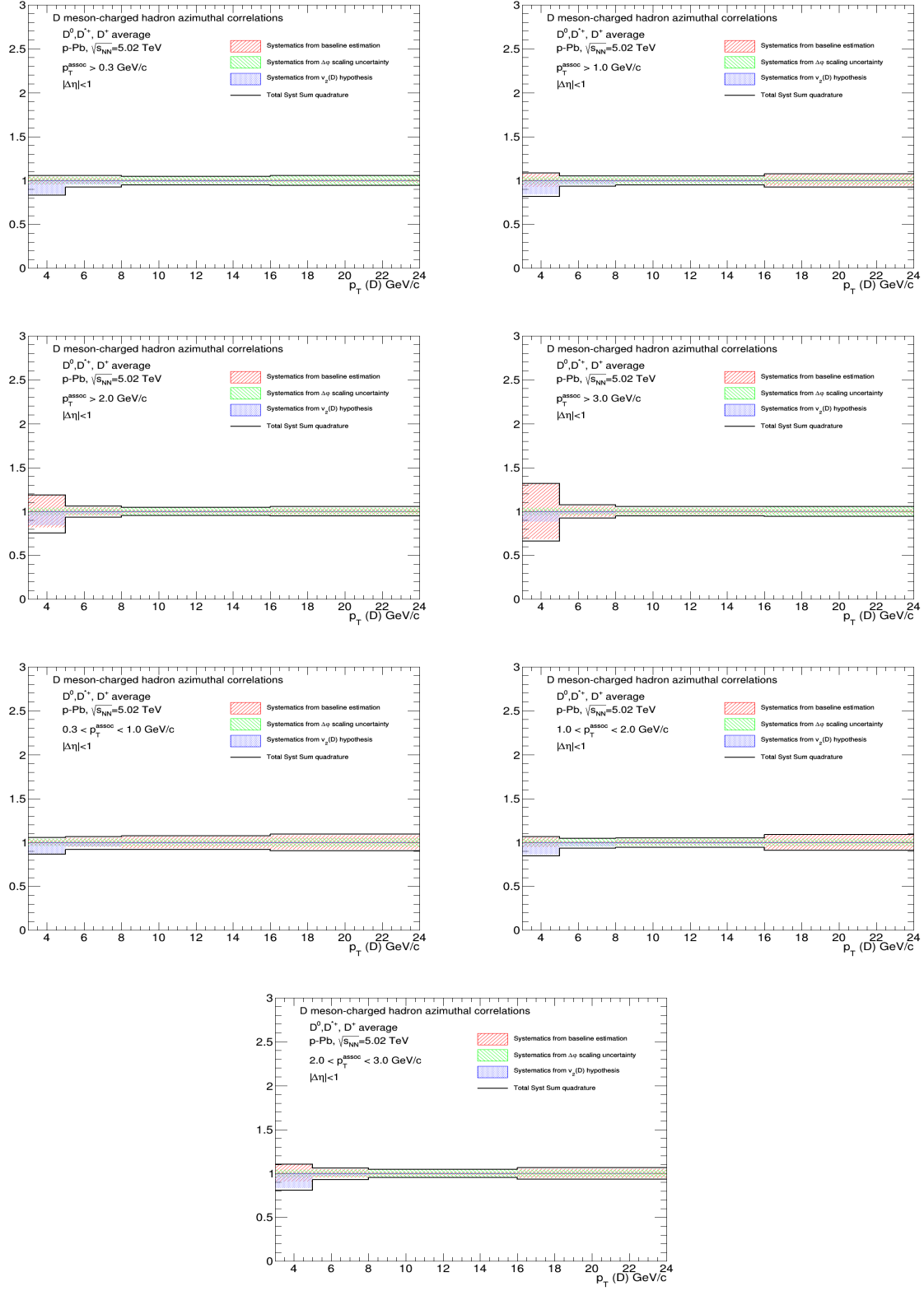


Figure 52: Total systematic uncertainty, and its components, for near-side yields in the different kinematic ranges analyzed

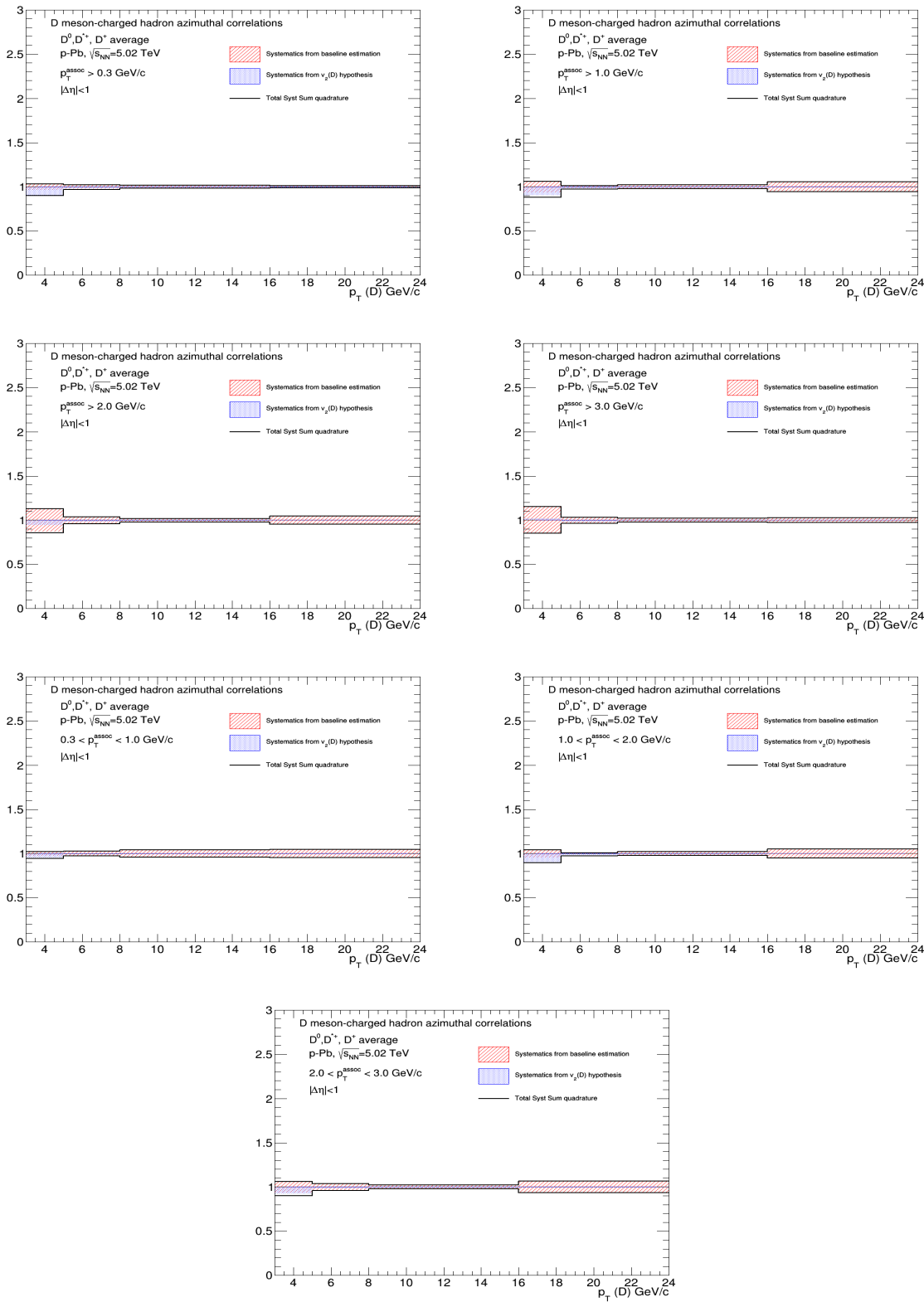


Figure 53: Total systematic uncertainty, and its components, for near-side sigma in the different kinematic ranges analyzed

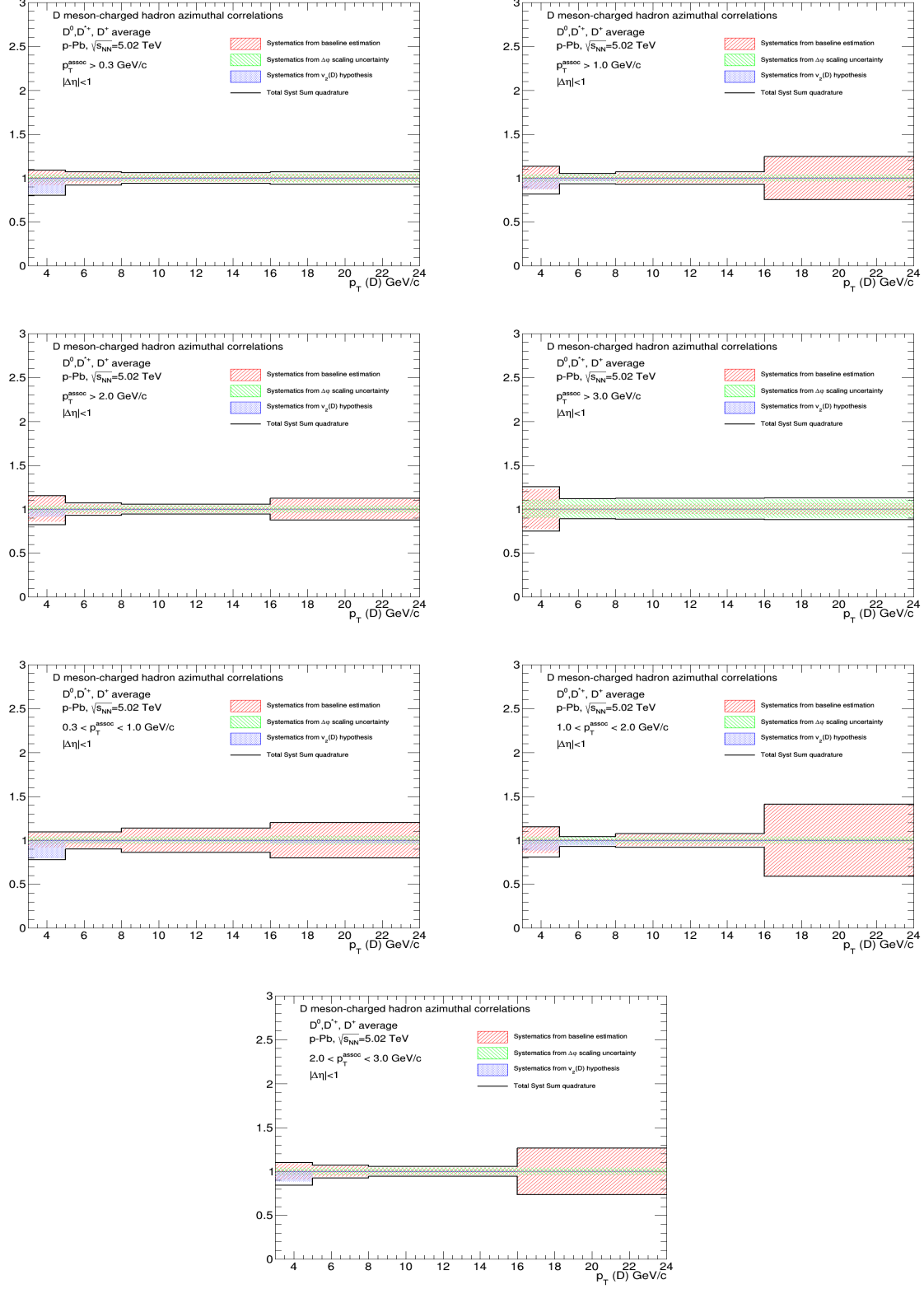


Figure 54: Total systematic uncertainty, and its components, for away-side yields in the different kinematic ranges analyzed

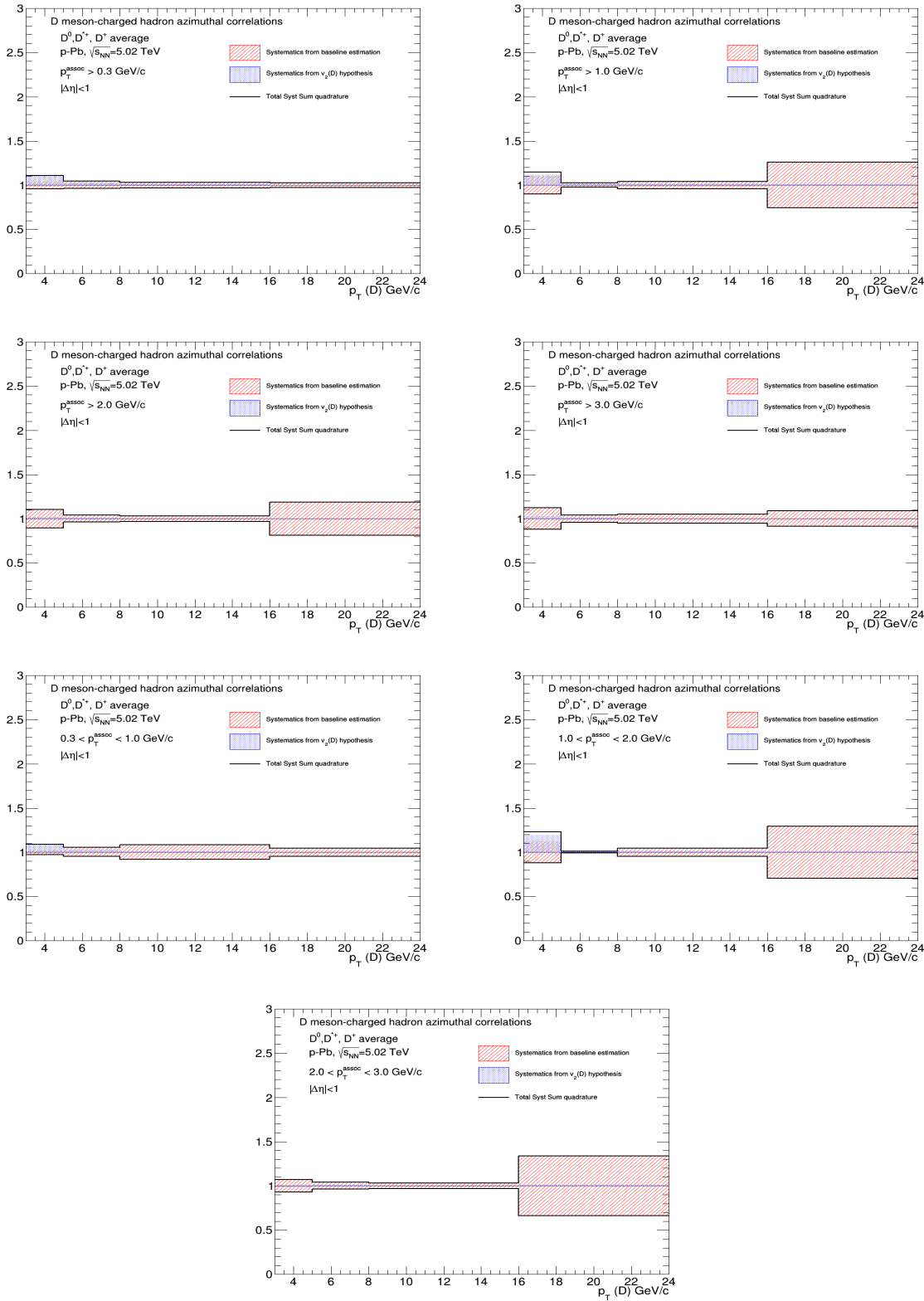


Figure 55: Total systematic uncertainty, and its components, for away-side sigma in the different kinematic ranges analyzed

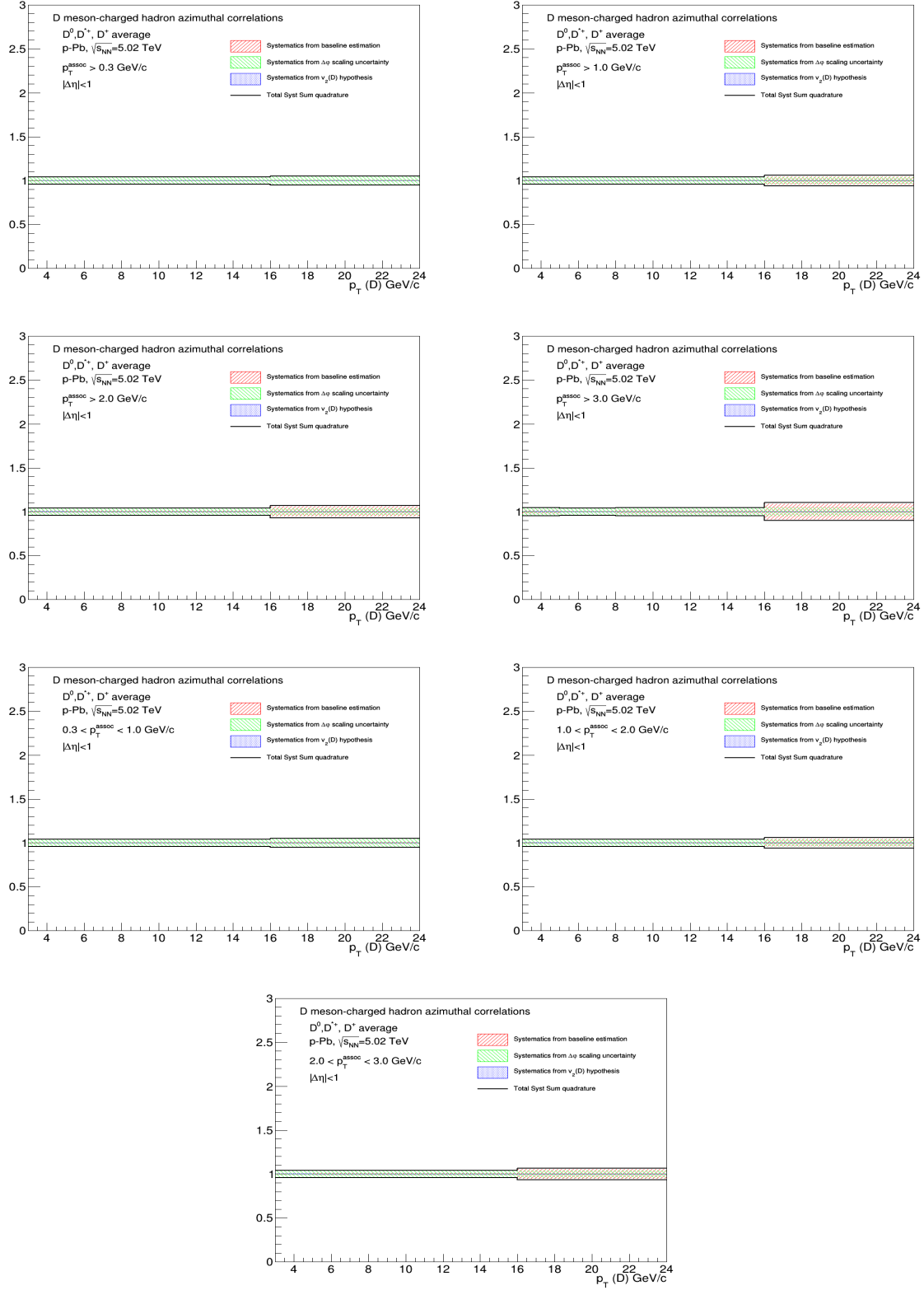


Figure 56: Total systematic uncertainty, and its components, for baseline heights in the different kinematic ranges analyzed.

686 **5.4 Comparison of 2016 p-Pb and 2013 p-Pb results**

687 In Figure 57, the average correlation distributions from the published analysis in p-Pb 2013 sample
 688 (black points) and the new p-Pb 2016 sample (red points), both at 5 TeV, are compared. As it's evident,
 689 the statistical and systematic uncertainties are largely reduced in the new data sample. The feature of
 690 the correlation distributions are the same in both systems, and an overall compatibility of the points is
 691 observed. Only in the near-side region, the 2016 points are generally slightly below the 2013 points. In
 692 part, this can be partially explained with the different procedure for assessing the B to D decay topology
 693 bias (2016 data are corrected, with a slight downward shift for the first two points, while for 2013 data
 694 only a downward systematic uncertainty was applied.

695 Figure 58 shows the same comparison for the fit observables. Also in this case the uncertainties are
 696 largely reduced for the 2016 analysis. While the away side features are compatible (but with large
 697 uncertainties) and the near-side widths are on top of each other, for the near-side yields a slight decrease
 698 of the 2016 results is observed (though well within the uncertainty). This is a direct consequence of
 699 the feature just observed in the comparison of the near-side peak point of the azimuthal correlation
 700 distributions.

701 **5.5 Comparison of 2016 p-Pb and 2010 pp results**

702 Figure 59 shows the comparison of the average D-h correlation distributions in pp 2010 data sample at
 $\sqrt{s} = 7$ TeV (published in [2]) and in the new p-Pb 2016 sample at $\sqrt{s_{NN}} = 5.02$ TeV. The results are
 703 shown after the subtraction of the baseline. The precision of the new p-Pb results is much better than that
 704 of pp results; the correlation distributions show very similar features in the two collision systems.

705 In Figure 60 the comparison is performed for the near-side peak observables, again in the common
 706 kinematic ranges, where the same consideration about the uncertainties holds. The similarity of the
 707 correlation distributions is reflected also in the near-side yield and width values, which do not seem to
 708 differ within the uncertainties, pointing to the absence of strong effects from cold-nuclear matter effects
 709 on the correlation distributions.

710 It has to be said that, on the base of a study performed with Pythia6-Perugia2011 simulations, a scaling
 711 factor of about 0.93 is expected when passing from a center-of-mass energy of $\sqrt{s} = 7$ TeV to $\sqrt{s} = 5$
 712 TeV, difficult to be appreciated with the current uncertainties, especially the pp ones.

714 **5.6 Comparison of 2016 p-Pb and model expectations**

715 A comparison of the average D-h correlation distributions on the new p-Pb data samples with expecta-
 716 tions from Monte Carlo simulations (currently Pythia6-Perugia2011, Pythia6-Perugia2010, Pythia6-
 717 Perugia0, PYTHIA8; POWHEG+PYTHIA and EPOS 3 will be added if they come in time) is shown in
 718 Figure 61, after the baseline subtraction (which differs strongly between data and simulations, due to he
 719 very different underlying event). The simulations, though being for pp, include the boost of the center-
 720 of-mass along the beam axis present in p-Pb collisions and nuclear PDF. The shape of the correlation
 721 distributions is well reproduced by all the models, together with their p_T trend and with the evolution of
 722 the correlation peaks.

723 Figures 62 and 63 show the same comparison for the fit observables (peak yields and widths for near-side
 724 and away-side, respectively), for all the addressed p_T ranges.

725 **5.7 Planned results for SQM approvals**

726 We are planning to approve the following results (the graphical way of showing the information has still
 727 to be defined):

- 728 – Average D-h correlation distributions, in the different kinematic ranges

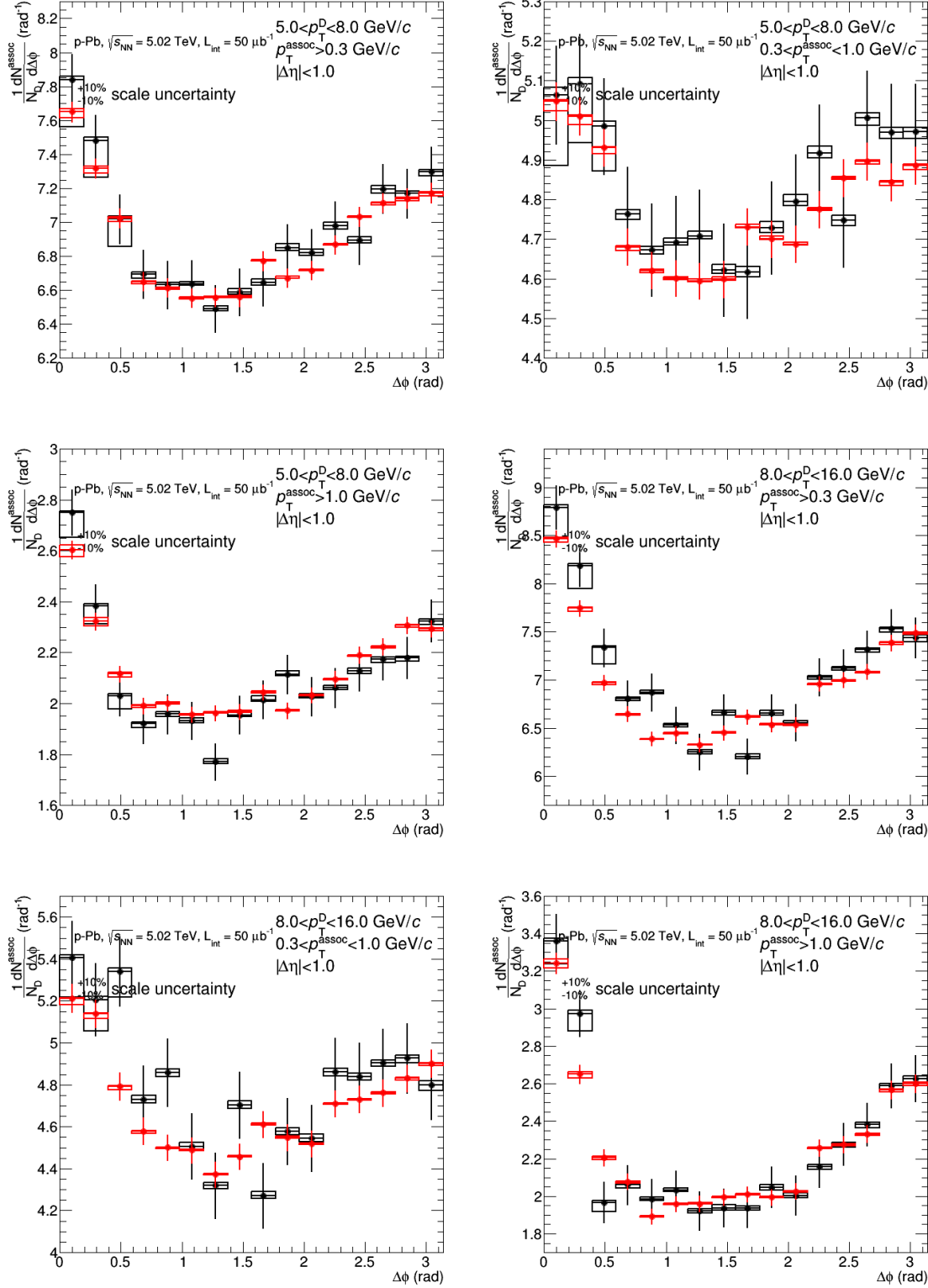


Figure 57: Comparison of 2016 (red) and 2013 (black) results for azimuthal correlation distributions, for the common p_T ranges.

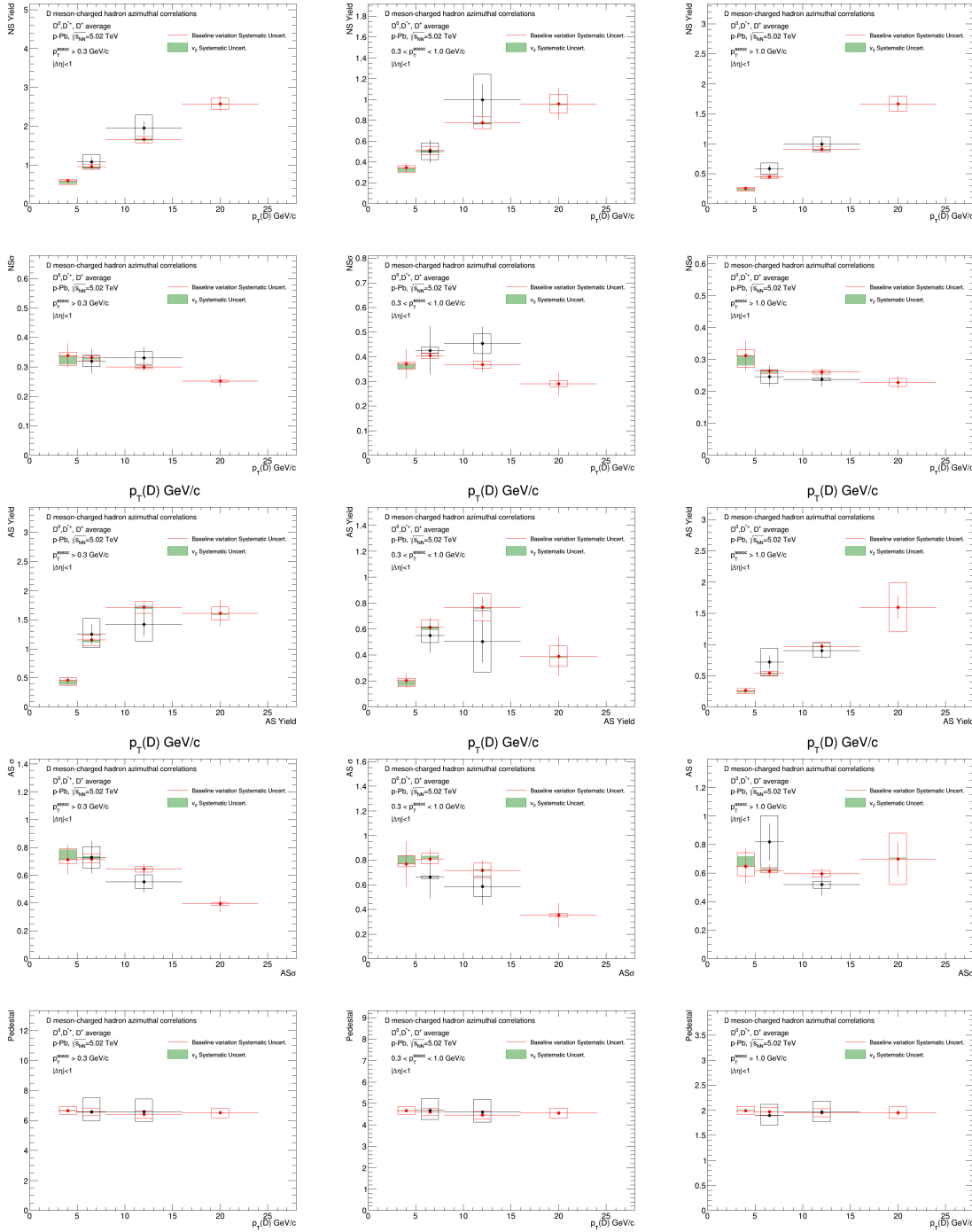


Figure 58: Comparison of 2016 (red) and 2013 (black) results for azimuthal correlation distributions, for the common p_T ranges.

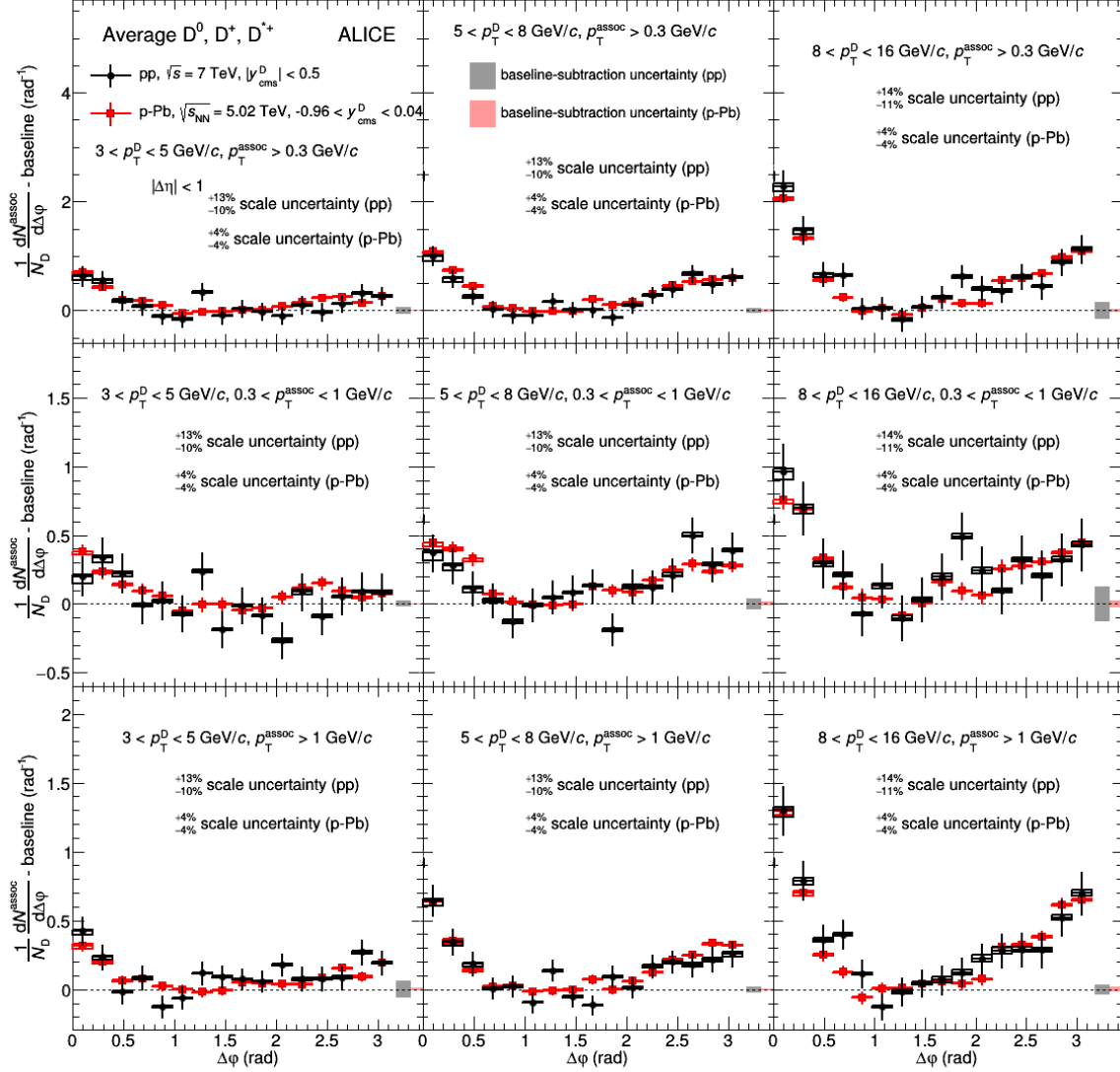


Figure 59: Comparison of pp 2010 (black) and p-Pb 2016 (red) average D-h azimuthal correlation distributions, for the common p_T ranges.

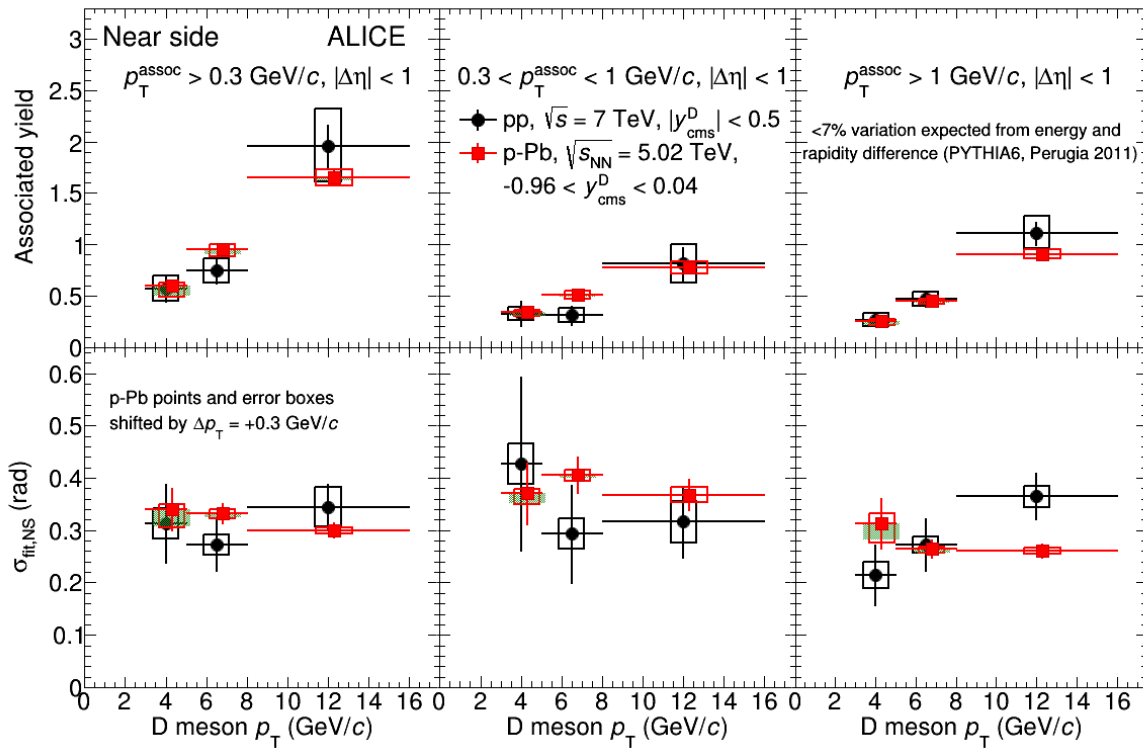
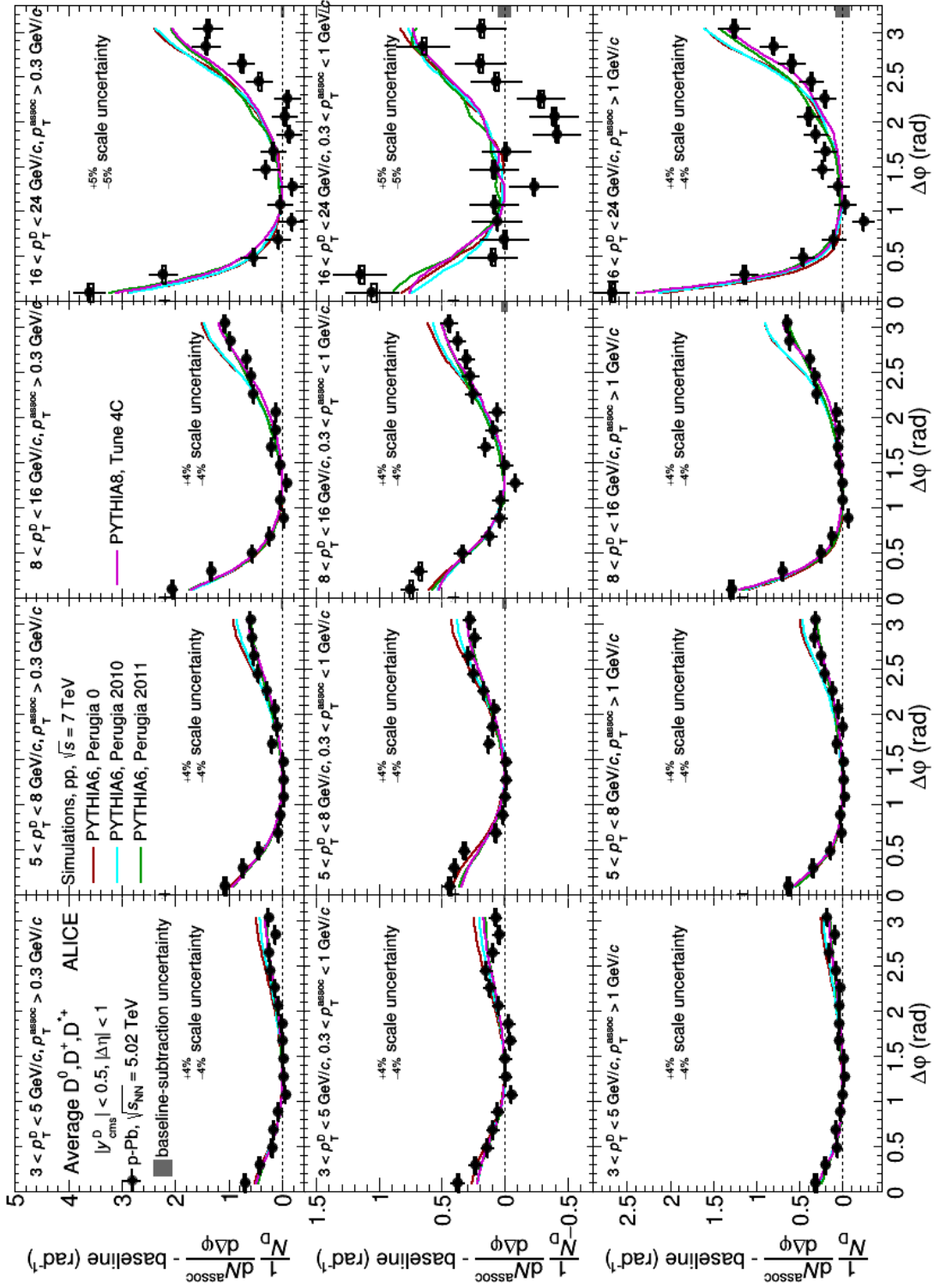


Figure 60: Comparison of pp 2010 (black) and p-Pb 2016 (red) near-side peak yields and widths, for the common p_T ranges.

- 729 – $pT(D), pT(\text{assoc})$ trend of NS yield, NS width, AS yield, AS sigma, baseline
- 730 – Comparison of correlation distributions with expectations from models (PYTHIA, POWHEG,
- 731 EPOS)
- 732 – Comparison of fit observables with expectations from models (PYTHIA, POWHEG, EPOS)
- 733 – (probably) Comparison of correlation distributions and/or fit observables with pp 2010 (and/or pPb
- 734 2013) results



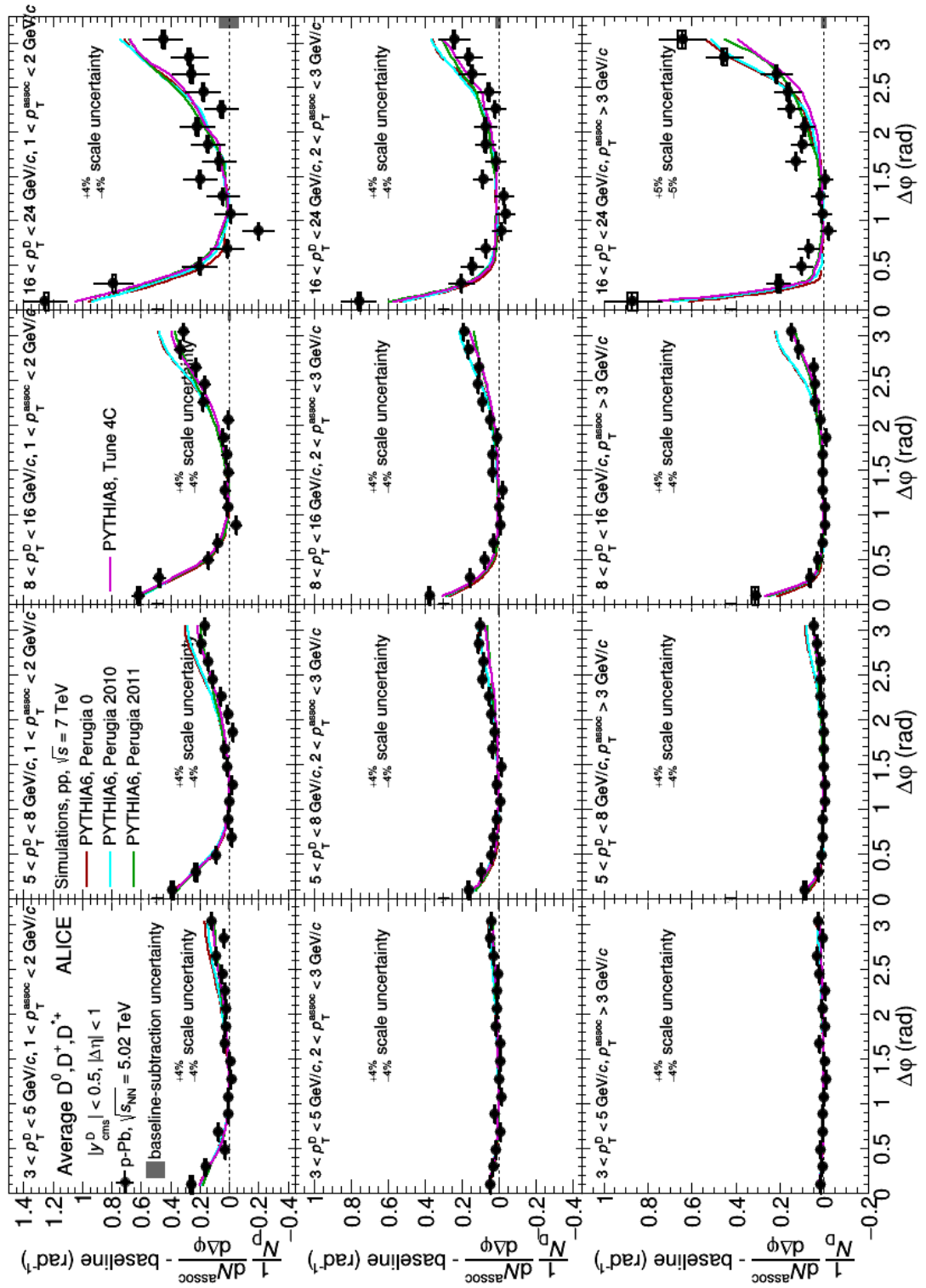
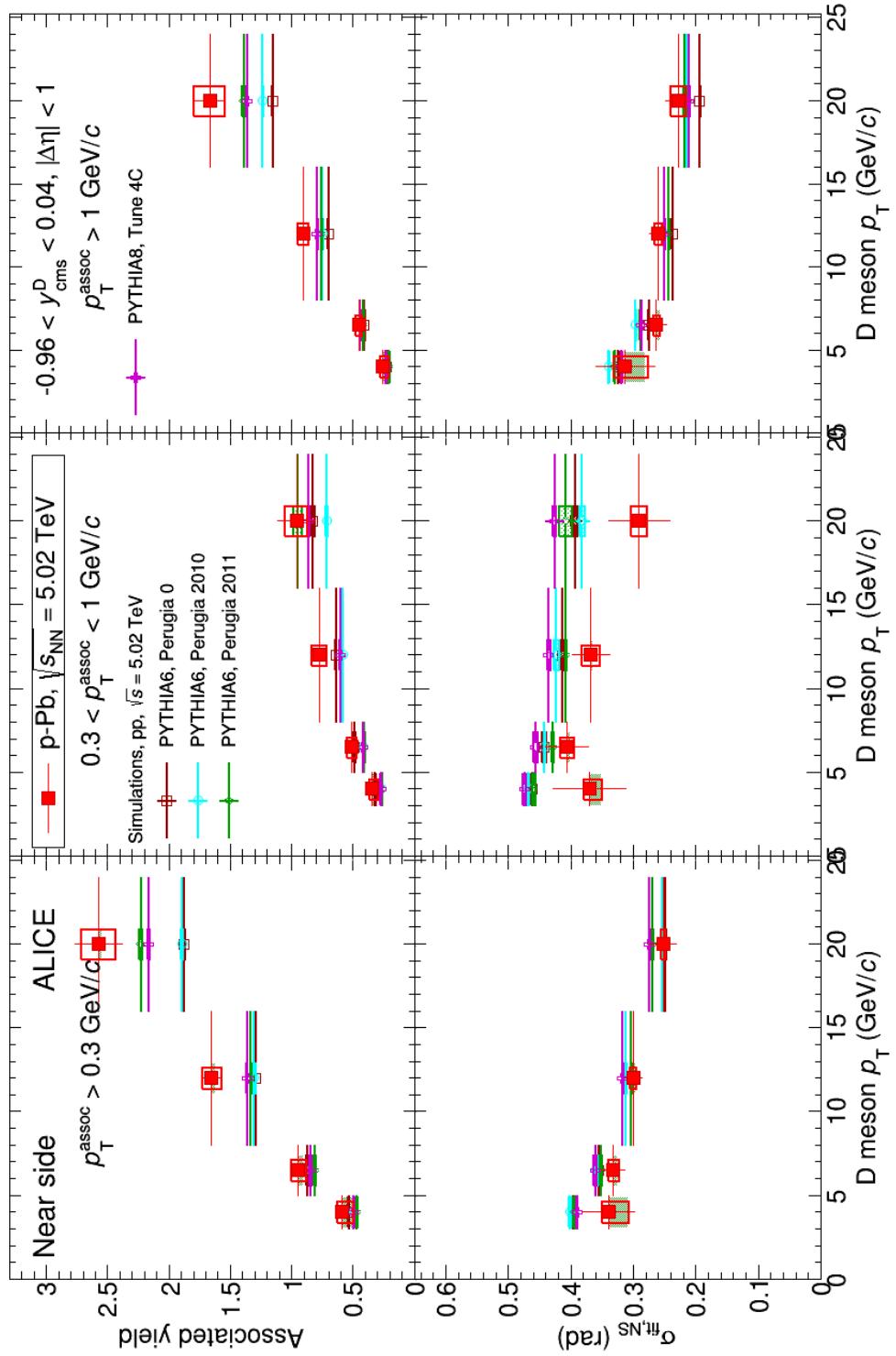


Figure 61: Comparison of p-Pb 2016 average D-h correlation distributions and model expectations, for all the studied kinematic ranges.



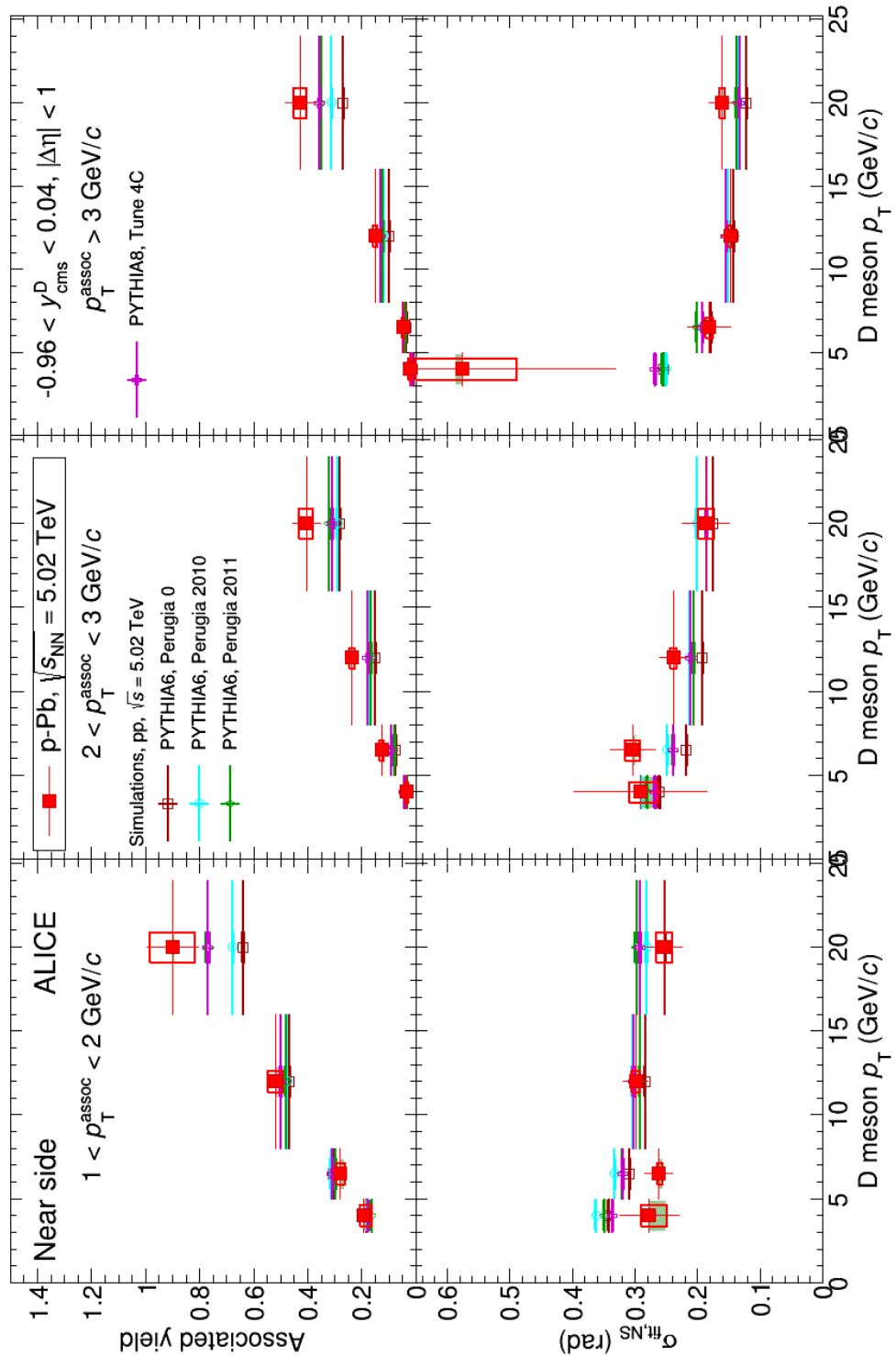
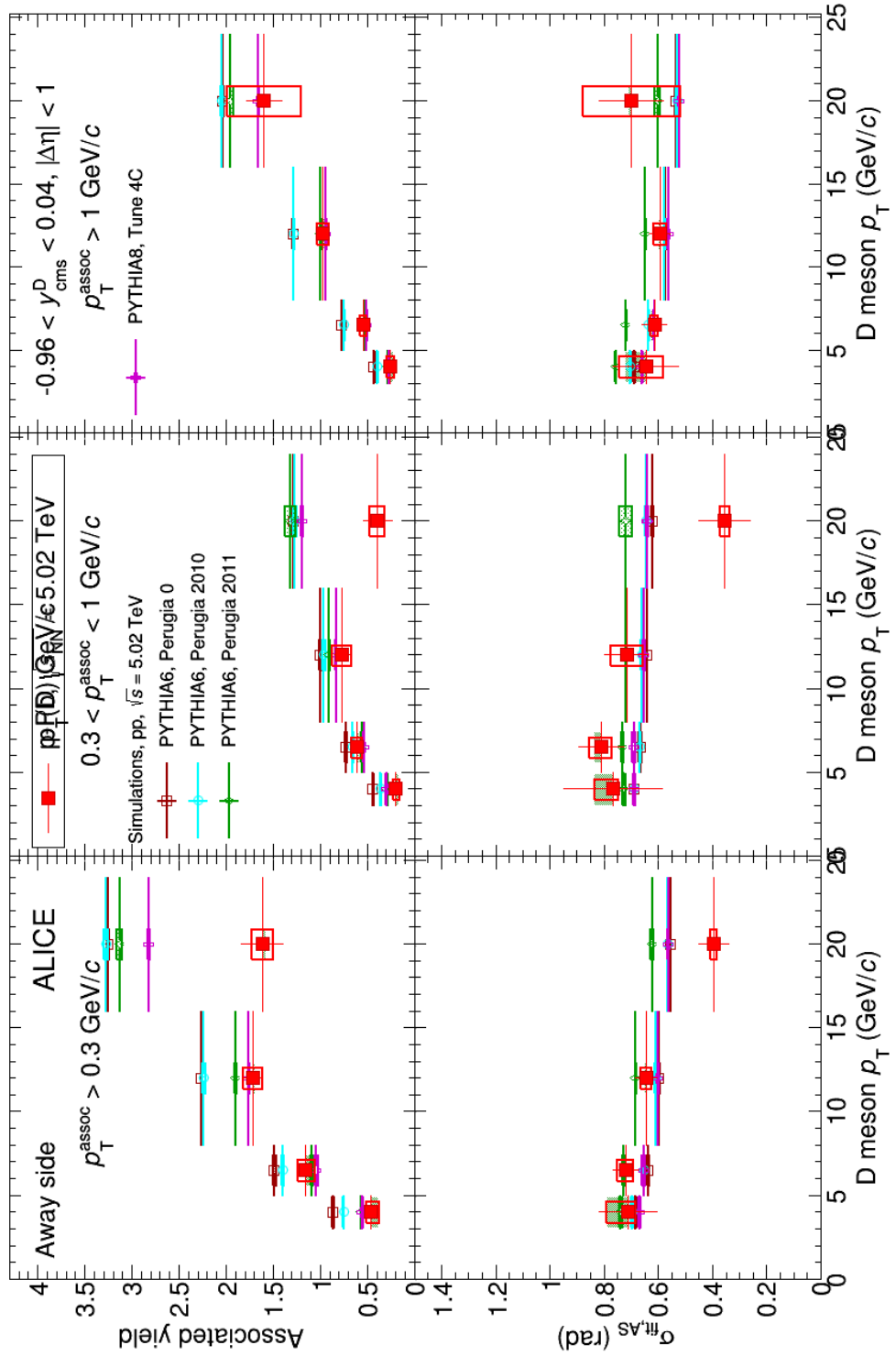


Figure 62: Comparison of near-side peak yields and widths from p-Pb 2016 results and model expectations, for all the studied kinematic ranges.



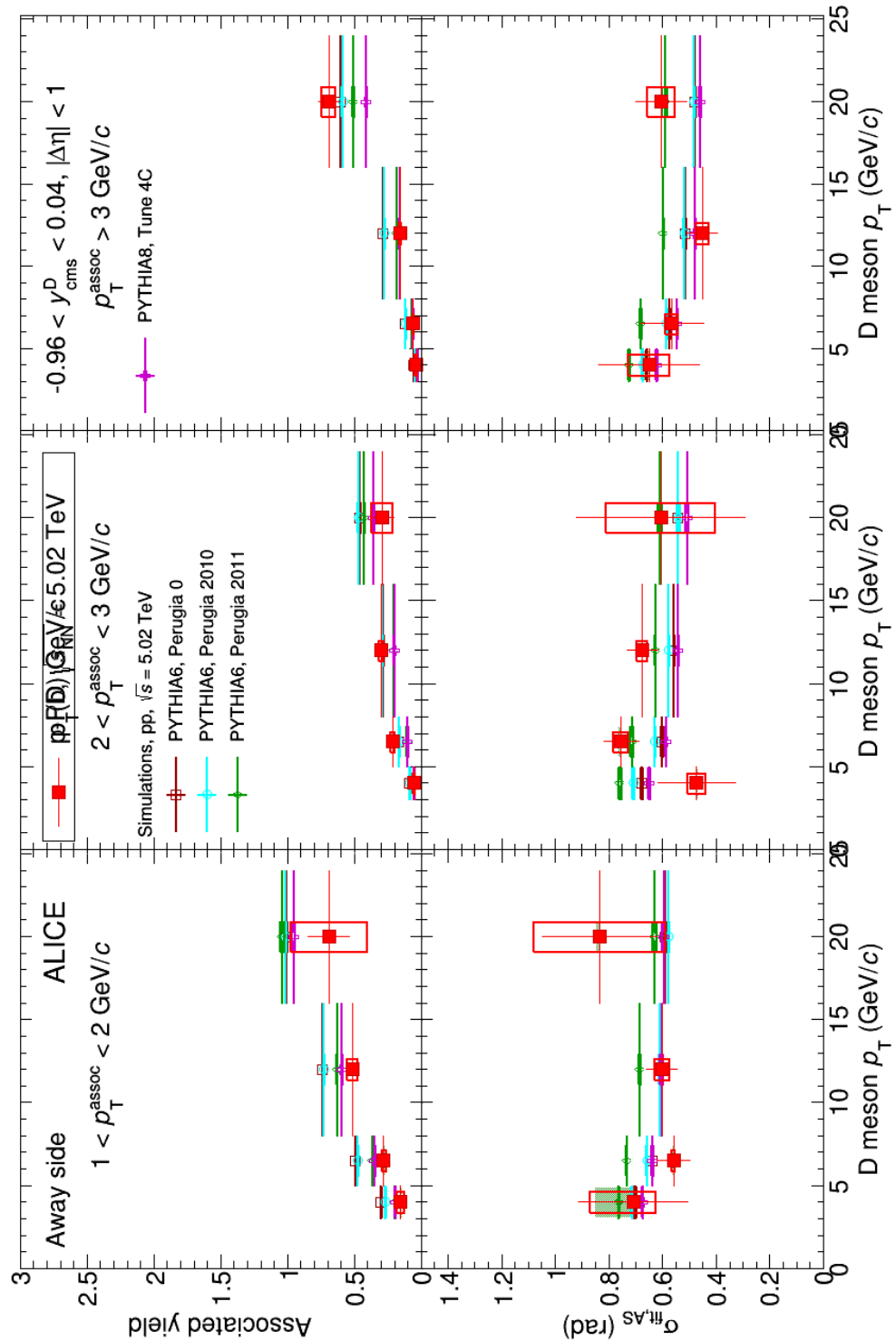


Figure 63: Comparison of away-side peak yields and widths from p-Pb 2016 results and model expectations, for all the studied kinematic ranges.

735 **6 Bibliography**736 **References**

- 737 [1] B. Abelev et al. [ALICE Collaboration], JHEP **01** (2012) 128
738 [2] B. Abelev et al. [ALICE Collaboration], Eur. Phys. J. C (2017) 77:245
739 [3] B. Abelev et al. [ALICE Collaboration], Phys.Lett. B719 (2013) 29-41